دانشگاه سمنان

دانشکده مهندسی برق و کامپیوتر

Frequency Selective Surface and Grid Array

سال تحصیلی ۹۵-۱۳۹۴

درس: دکتر مجید اصحی

Frequency Selective Surface and Grid Array

WILEY SERIES IN MICROWAVE AND OPTICAL ENGINEERING

KAI CHANG, Editor
Texas A & M University

FIBER-OPTIC COMMUNICATION SYSTEMS
Govind P. Agrawal

COHERENT OPTICAL COMMUNICATIONS SYSTEMS
Silvello Betti, Giancarlo De Marchis and Eugenio Iannone

HIGH-FREQUENCY ELECTROMAGNETIC TECHNIQUES: RECENT ADVANCES AND APPLICATIONS
Asoke K. Bhattacharyya

COMPUTATIONAL METHODS FOR ELECTROMAGNETICS AND MICROWAVES
Richard C. Booton, Jr.

MICROWAVE SOLID-STATE CIRCUITS AND APPLICATIONS
Kai Chang

MULTICONDUCTOR TRANSMISSION-LINE STRUCTURES: MODAL ANALYSIS TECHNIQUES
J. A. Brandão Faria

MICROSTRIP CIRCUITS
Fred Gardiol

HIGH-SPEED VLSI INTERCONNECTIONS: MODELING, ANALYSIS, AND SIMULATION
A. K. Goel

HIGH-FREQUENCY ANALOG INTEGRATED CIRCUIT DESIGN
Ravender Goyal (ed.)

OPTICAL COMPUTING: AN INTRODUCTION
Mohammad A. Karim and Abdul Abad S. Awwal

MICROWAVE DEVICES, CIRCUITS AND THEIR INTERACTION
Charles A. Lee and G. Conrad Dalman

ANTENNAS FOR RADAR AND COMMUNICATIONS: A POLARIMETRIC APPROACH
Harold Mott

SOLAR CELLS AND THEIR APPLICATIONS
Larry D. Partain (ed.)

ANALYSIS OF MULTICONDUCTOR TRANSMISSION LINES
Clayton R. Paul

INTRODUCTION TO ELECTROMAGNETIC COMPATIBILITY
Clayton R. Paul

NEW FRONTIERS IN MEDICAL DEVICE TECHNOLOGY
Arye Rosen and Harel Rosen (eds.)

FREQUENCY SELECTIVE SURFACE AND GRID ARRAY
T. K. Wu (ed.)

OPTICAL SIGNAL PROCESSING, COMPUTING AND NEURAL NETWORKS
Francis T. S. Yu and Suganda Jutamulia

Frequency Selective Surface and Grid Array

Edited by

T. K. WU
TRW Electronic Systems and Technology Division

A WILEY-INTERSCIENCE PUBLICATION
JOHN WILEY & SONS, INC.
New York / Chichester / Brisbane / Toronto / Singapore

Library of Congress Cataloging in Publication Data:

Frequency selective surface and grid array / edited by T. K. Wu.
p. cm.
"A Wiley-Interscience publication."
Includes index.
ISBN 0-471-31189-8
1. Microwave devices—Materials. 2. Frequency selective surfaces.
3. Diffraction gratings. I. Wu, T. K., 1948–
TK7876.F74 1995
621.381'3—dc20 95-4985

Printed in the United States of America

10 9 8 7 6 5 4 3 2 1

Contents

Contributors

Chi-Hou Chan, Department of Electrical Engineering, University of Washington, Seattle, WA 98195

Jonathan B. Hacker, BellCore, 331 Newman Springs Road, Red Bank, NJ 07701

Gregory S. Hickey, Jet Propulsion Laboratory, California Institute of Technology, Pasadena, CA 91109

Raj Mittra, Electromagnetics Communication Laboratory, University of Illinois, Urbana, IL 61801

Robert G. Schmier, Westinghouse Electric Corporation, Electronic Systems Group, Baltimore, MD 21203-0746

Lance B. Sjogren, RF Products Center, TRW Electronic Systems and Technology Division, Redondo Beach, CA 90278

Joseph D. Vacchione, Jet Propulsion Laboratory, California Institute of Technology, Pasadena, CA 91109

Robert M. Weikle, University of Virginia, Department of Electrical Engineering, Charlottesville, VA 22903

Te-Kao Wu, formerly with Jet Propulsion Laboratory, California Institute of Technology, Pasadena, CA 91109; now with TRW Electronic Systems and Technology Division, Redondo Beach, CA 90278

Foreword

In electric circuits, filters are one of the fundamental devices. In microwave engineering, the counterpart of a filter is a frequency selective surface (FSS). There are two major applications of FSS. One is to use FSS as antenna radomes for better control of electromagnetic wave transmission and scattering. The other application of FSS is in reflector antenna systems, where FSS reflectors are used to separate feeds of different frequency bands.

Since the advent of FSS in the late 1960s, there has been a sizable effort in the study of FSS from the viewpoint of theory, measurement, and manufacture, out of which a wealth of knowledge has grown. Up to this point, the knowledge has been scattered throughout technical, conference proceedings, and company reports. Some of it is unpublished. There is a need for a unified presentation of FSS technology. Dr. T. K. Wu, an internationally known researcher in electromagnetics, has taken on this task. The result is this comprehensive book on FSS and associated devices.

The eight chapters of this book cover various aspects of FSS, ranging from modal analysis to fabrication. All chapters are written by recognized experts in this field. For those people who want to learn about FSS, as well as for those who work with FSS, I recommend this book highly.

SHUNG-WU LEE

University of Illinois, Urbana

brief summary of FSS analytical and measurement techniques. A FORTRAN computer code is given in the Appendix for calculating the transmission and reflection performance of a gridded square-loop, square-loop, or double-square-loop patch-element FSS using the equivalent circuit model. More sophisticated codes, using the accurate integral equation technique, may be purchased from Professors R. Mittra and S. W. Lee of the University of Illinois.

Chapters 2 through 6 are devoted to FSS analyses, designs, and applications. Chapter 2, by Dr. Chi Chan, presents a very thorough treatment of the single thin- or thick-screen FSS analysis using the spectral domain approach. The cascading analysis of multiple FSS screens is discussed in Chapter 3 by Dr. Joe Vacchione and Professor Mittra. Chapter 4 presents two case studies of FSS application to multiband communication antenna systems. Various practical FSS designs are described in detail to give readers as many examples as possible. Chapter 5, by Mr. Robert Schmier, presents a thorough thick- and thin-screen FSS analysis, using the spatial domain approach, and an interesting application to bandpass radomes. The detailed equations for the reaction integrals, which have never been disclosed in any reference, are given in the Appendix. Chapter 6, by Mr. Gregory Hickey, presents FSS materials and fabrication techniques, which are the first disclosure of these subjects in any book.

Chapters 7 and 8 constitute the second part of the book, devoted to active grid arrays. Chapter 7, by Dr. Lance Sjogren, presents the beam control array, which incorporates a variable-impedance element to provide an FSS whose characteristics are externally controllable. Chapter 8, by Drs. Jon Hacker and Robert Weikle, emphasizes the incorporation of active devices that provide gain or nonlinearity into an FSS, enabling the development of arrays with numerous additional capabilities, including oscillation, amplification, and mixing. The authors have also provided two computer source codes for analyzing the equivalent circuit parameters for the cross-dipole and bow-tie grid unit-cell configurations. These codes are developed using the EMF method discussed in the chapter.

Finally, I would like to thank Professor Kai Chang of Texas A & M University for his suggestions and encouragement and for including this book in the Microwave and Optical Engineering Series; all the authors for their contributions and for their cooperation; Drs. S. Govind of Northrop, L. Sjogren of TRW, and J. Vacchione of JPL for reviewing the original manuscripts; Mr. G. Telecki, Ms. Rose Leo Kish, Ms. Angioline Loredo, Mr. Perry King, and the production staff of John Wiley & Sons, Inc. for their assistance and fine work in the processing and publishing of this book.

T. K. WU

CHAPTER ONE

Fundamentals of Periodic Structures

T. K. WU, Jet Propulsion Laboratory, California Institute of Technology, Pasadena, California

Two-dimensional planar periodic structures, as depicted in Figure 1.1, have attracted a great amount of attention because of the frequency filtering property suggested. A periodic array consisting of conducting patch or aperture elements [1–3] is known as a frequency selective surface (FSS), or dichroic. Similar to the frequency filters in traditional radio-frequency (RF) circuits, the FSS may have low-pass or high-pass spectral behavior, depending upon the array element type (i.e., patch or aperture).

More recently, the capabilities of the FSS have been extended by the addition of active devices embedded in the unit cell of the periodic structures. Such structures are also called active grid arrays [4–7]. One category of this grid array, the beam control array, incorporates a variable-impedance element to provide an FSS whose characteristics are externally controllable. Such arrays are discussed in Chapter 7. Incorporation of devices that provide gain or nonlinearity into an FSS allows the development of arrays with numerous additional capabilities, including oscillation, amplification, and mixing. Such arrays are discussed in Chapter 8.

Note that phased array antennas [8–11] do not fall into the category of grid arrays. The primary distinguishing features of the grid array are that it is a simple planar FSS with few (typically one or two) active devices embedded in the FSS unit cell, and it operates on a nonconfined propagating beam

Frequency Selective Surface and Grid Array, Edited by T. K. Wu
ISBN 0-471-31189-8

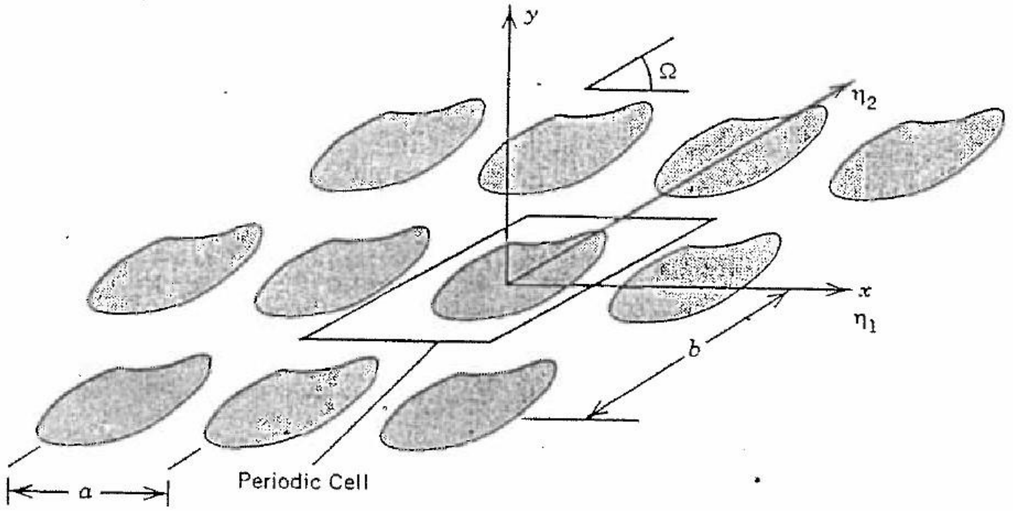

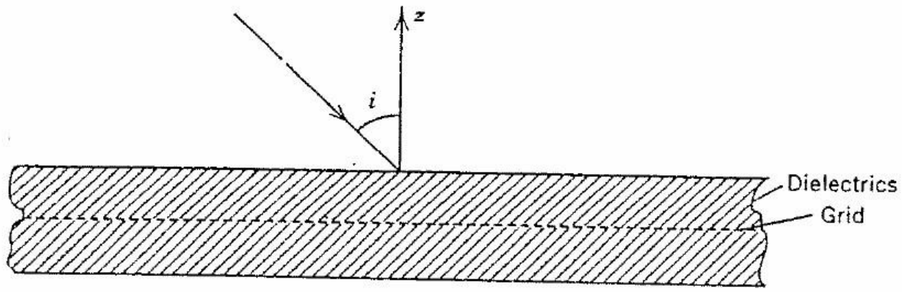

FIGURE 1.1 Geometry of a two-dimensional periodic structure.

rather than on an RF signal brought in through a guided-wave structure (e.g., a waveguide, microstrip, or stripline).

Many design parameters and principles are associated with the periodic structure, such as element shape, size, lattice geometry, dielectrics, grating lobes, and Wood's anomaly. These concepts are introduced in this chapter; more detailed descriptions of the analysis and design are given in subsequent chapters.

1.1 FSS ELEMENTS

An FSS is a periodic array of aperture or patch elements. As illustrated in Figure 1.2, the *aperture*-element FSS reflects at low frequencies and transmits at high frequencies (similar to a high-pass filter), whereas the *patch*-element FSS transmits at low frequencies and reflects at high frequencies

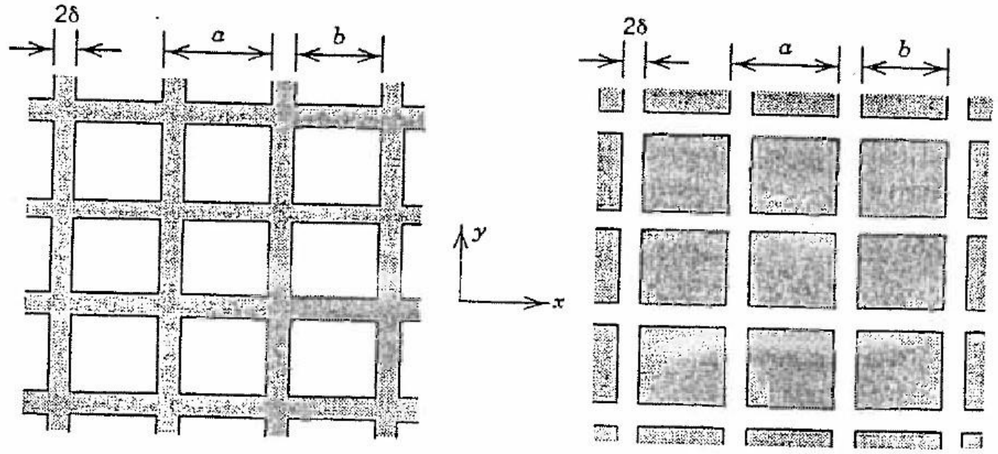

Shaded Area Is Metal

(a) High-Pass Aperture Element

(b) Low-Pass Patch Element

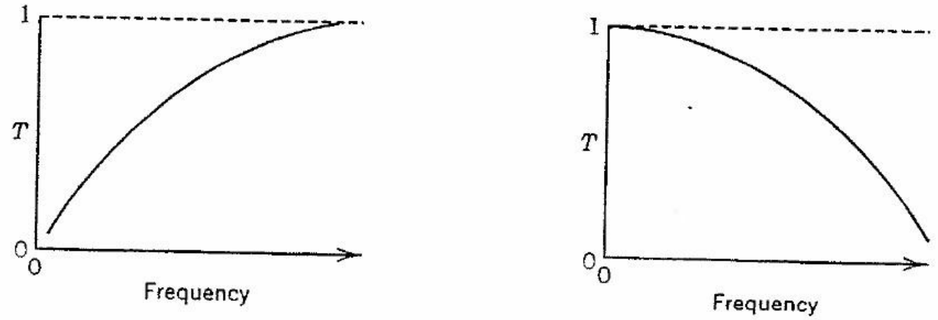

FIGURE 1.2 Aperture (a) and patch-element FSS (b).

(similar to a low-pass filter) [1–3]. For freestanding thin grids without dielectrics, the performance of the patch FSS exactly complements that of the aperture FSS. An FSS may also be categorized as thick- or thin-screen, depending on the thickness of the element. The term *thin-screen FSS* usually refers to a screen with printed-circuit-type elements—that is, patch or aperture elements less than 0.001 λ thick, where λ is the wavelength at the screen's resonant frequency. In general, the thin-screen FSS is lightweight, low volume, and can be inexpensively fabricated with conventional printed circuit technology.

On the other hand, a thick-screen FSS, used mostly for high-pass applications (aperture type), is a periodic array of elements with electrically large thickness. It is heavy, and fabrication requires precise and expensive machining of a thick metal block. Waveguide stacks [12–15] have been a popular thick-screen FSS. The advantage of thick-screen FSSs is that the ratio of

transmission frequency to reflection frequency (f_t/f_r), or band separation, can be reduced to 1.15 (= 14.0 GHz/12.2 GHz), which is required for advanced multifrequency communication satellite antennas [14]. When filled with a dielectric such as paraffin wax, the waveguide's cutoff frequency is reduced, so the waveguide can be smaller. Hence, a closely packed array is achieved without any grating lobe occurring in the operation bands. It has also been found that increasing the angle of incidence increases cross-polarization level and causes ellipticity in circularly polarized waves. One way to overcome this is to make the holes slightly oval, instead of circular, as indicated in Potter [16]. Chapters 2 and 5 discuss thick-screen FSS.

1.1.1 Element Shape

Figure 1.3 illustrates some of the most common of the various element shapes: circular [3, 12, 16], rectangular/dipole [17–20], cross dipole [21–25], Jerusalem cross [25–27], tripole [28], three- or four-legged dipole [29], ring [30–33], square-loop [34–37], and gridded square loop [36, 39]. One interesting element, invented by Rosen [38], has a capacitor inside a rectangular loop element to shorten the transmission/reflection band separation (f_t/f_r = 14.0/12.2 = 1.15).

The relative performance ratings of several freestanding, thin-screen FSSs are listed in Table 1.1. Seven elements are considered, and four characteristics—stability of resonant frequency with incident angle, cross-polarization level, bandwidth, and smallest band separation—are rated. The resonant frequency of the freestanding dipole element array has the worst stability with incident angle variations. Hence, it has the smallest operable bandwidth. The reason is that when a vertically polarized incoming wave hits a half-wave dipole in the x-y plane, as shown in Figure 1.3, the dipole will resonate

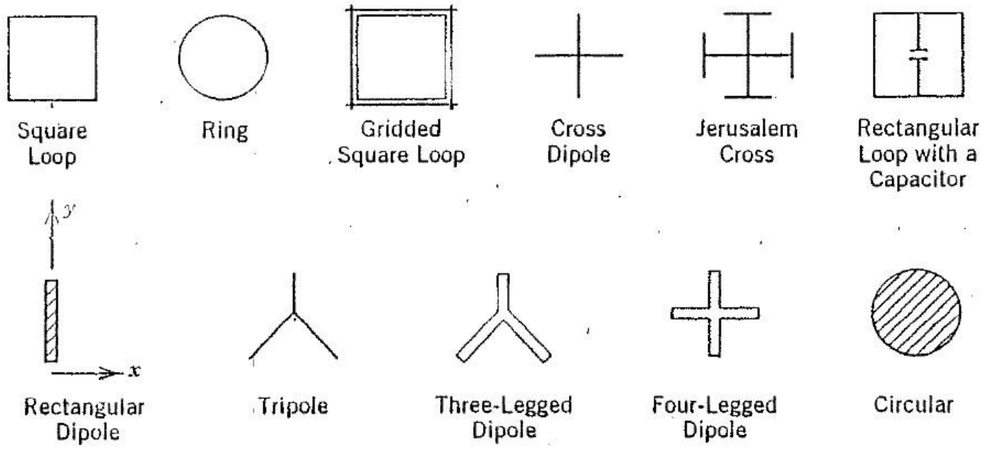

FIGURE 1.3 FSS element shapes.

TABLE 1.1.

Type of Element	Stability of Resonant Frequency with Angle of Incidence	Cross-Polarization Level	Larger Bandwidth	Small Band Separation
Loaded dipole	1	2	1	1
Jerusalem cross	2	3	2	2
Rings	1	2	1	1
Tripole	3	3	3	2
Crossed dipole	3	3	3	3
Square loop	1	1	1	1
Dipole	4	1	4	1

Ratings: best = 1, second best = 2, ...
Based on the freestanding single screen's performance.

regardless of incident angle. However, if the incident direction is oblique to the broadside of the dipole, the dipole will not resonate effectively, depending on the incident angles, because the projected length of the dipole in the incident direction is now less than a half-wavelength. For this reason the resonant frequency of the dipole or the crossed-dipole element FSS shifts drastically when incoming waves have large incident angles.

1.1.2 Element Size

When a strip dipole element, such as that shown in Figure 1.3, is illuminated by an RF source, and if the length of the dipole is a multiple of a half-wavelength, the dipole will resonate and scatter the energy. When many strip dipoles are arrayed, the reradiated energy from all the elements will be coherent toward the direction as if a reflection is occurring, where the reflection angle equals the incident angle. This is true because the induced surface current on each strip has a phase delay relative to its neighboring element. It is this phase delay that causes the scattered waves from all the elements to be coherent toward the reflection direction.

For square-loop and circular-loop (ring) elements (Figure 1.3), resonance occurs when the length of each half-loop is a multiple of a half-wavelength. In other words, each half-loop is acting as a dipole element. The length of the whole loop therefore needs to be a multiple of one full wavelength. To avoid a null in the scattered pattern, the length of the loop must be one wavelength instead of a multiple wavelength (a one-wavelength-long dipole will have a null in its broadside direction, a 1.5-wavelength-long dipole will form two nulls in the off-broadside directions, etc.) Similarly, a multiwave-

length loop is expected to have such undesirable nulls formed in its scattered pattern. To summarize, the mean circumference of a printed circular-ring element for the FSS application must be one wavelength long. For a ring element printed on a dielectric substrate, the electrical length of the circumference must be one effective wavelength, and the physical circumference will therefore be less than one free-space wavelength; this requirement is the result of the dielectric loading effect.

When the element size is quite different from the resonant dimensions, the incident wave will travel through an FSS screen as if the screen were essentially transparent. A small loss will occur due to dielectric, copper conduction, and scattering. Figure 1.4 illustrates the typical transmission characteristic of a ring-element FSS with a resonant frequency of $f_0 =$ 8.4 GHz, at which the screen reflects the incident wave. For frequencies

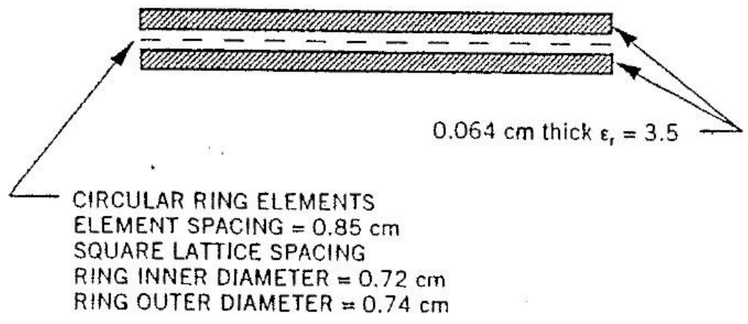

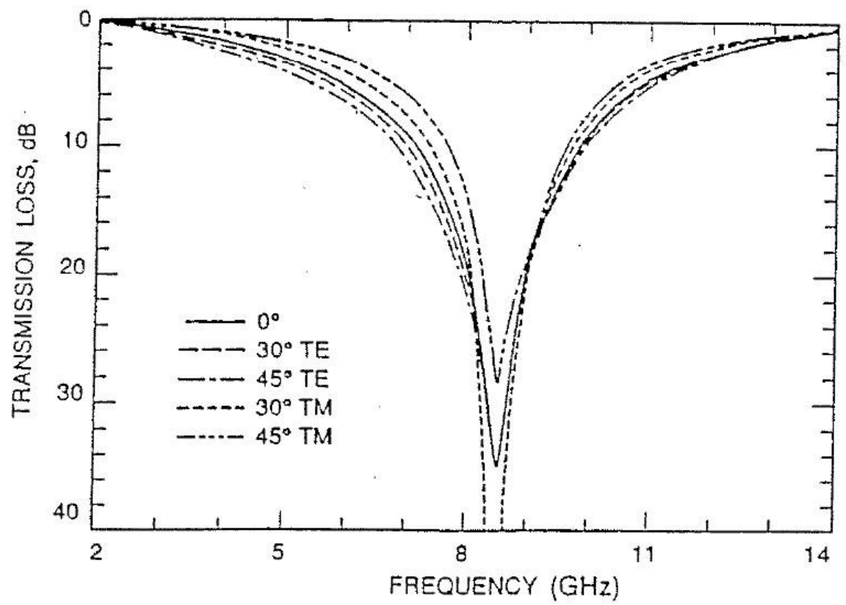

FIGURE 1.4 Transmission performance of a ring-element FSS with dielectrics on both sides (From [32]).

lower than f_0, transmission occurs. Transmission also occurs for frequencies higher than f_0, except when the size of the element is a multiple of the resonant dimension at f_0 and when the element spacing becomes so large that a grating lobe starts to appear (to be discussed later).

1.2 DIELECTRIC LOADING EFFECTS

Dielectrics are often used for stabilizing the drift of the FSS's resonant frequency with the steering of incident angle or for structural support. A number of dielectric loading effects have been published [3, 41–43]. Figure 1.5 shows that resonant frequencies decrease as dielectric thickness increases [42]. Two basic dielectric configurations are shown: (1) the grids are bonded on one side, and (2) the grids are embedded centrally in the dielectrics. For a normally incident thin grid (with a 0.02-mm-thick dielectric $\epsilon_r = 3.0$) the resonant frequency is 20 GHz. As can be seen, the resonant frequency of the *patch* array embedded in the dielectrics (with $\epsilon_d = 4.0$) approaches 10 GHz ($= 20/\sqrt{\epsilon_d}$) as dielectric thickness is increased beyond 5 mm. The passband frequency of the *slot* (aperture element) array in the dielectrics also tends to this value, but it exhibits an oscillatory behavior about 10 GHz. For a patch or slot array bonded on one side of the dielectric (with $\epsilon_d = 4.0$), the resonant frequency approaches 12.5 GHz ($= 20/\sqrt{\epsilon_e}$, with $\epsilon_e = 2.5$, which is the average of 4.0 and 1.0).

The dielectric loading effect of a slot array also depends on incident angle and wave polarizations. For transverse electric (TE) incidence, the resonance decreases as the dielectric thickness increases (similar to normal incidence). For transverse magnetic (TM) incidence, a significant reduction in the dielectric loading effect is noticed as the Brewster angle (63°) is approached. At this angle the air/dielectric interface does not reflect incident waves, and the resonant frequency behaves similarly to that of the patch array (i.e., it remains constant at 10 GHz). In fact, the angular stability of the slot arrays is lost for dielectric thickness greater than 1 mm. However, if the dielectric thickness is a multiple of a quarter-wavelength (i.e., $\epsilon_d = 4$ and $t = 7.5$ mm), the resonant frequency shift again becomes stable.

Note that there is a mismatch loss for a slot array with dielectric on one side, unless its thickness is a multiple of a half-wavelength. For example, the mismatch loss is 2 dB at normal incidence with a $\epsilon_r = 4$ dielectric substrate. However, with an equal thickness of dielectric on both sides of the grid, the reflection at the two air/dielectric interfaces are tuned out at the resonant frequency; consequently there is no passband mismatch loss whatever the dielectric thickness.

One of the most important applications of dielectric loading is the multiband FSS design. For a multiband FSS application, the highest frequency generally determines the element spacing or lattice size. For the triband FSS in Figure 1.6, the element spacing is 0.39 free-space wavelengths at the Ku band (13.8 GHz), too small to accommodate the circumference of the ring

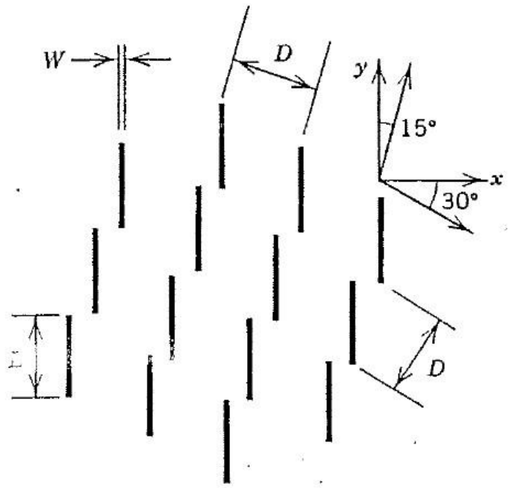

$D = L \approx 7.4$ mm; $W = 0.74$ mm

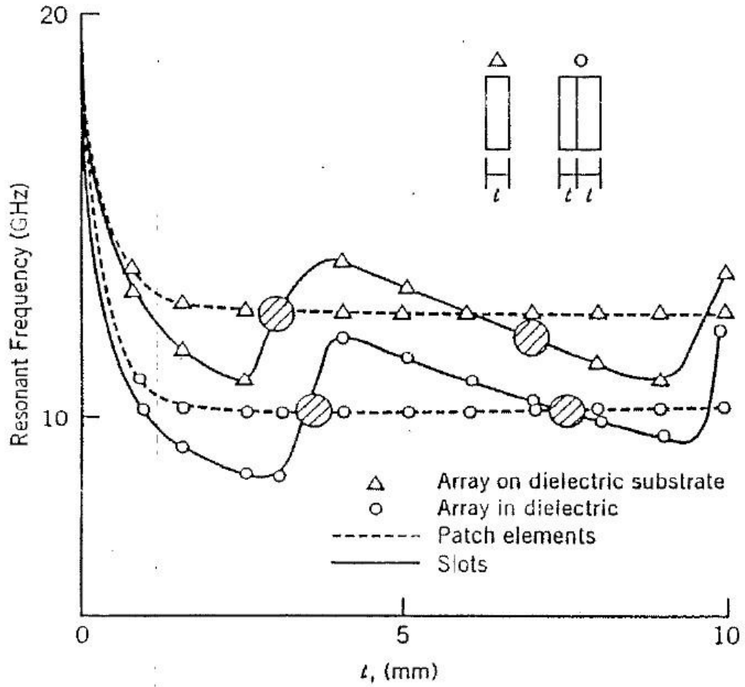

FIGURE 1.5 Variation of resonant frequency with the dielectric thickness for normal incidence (From [42]).

element, which must be one electrical wavelength long at the X band for reflection to occur. One method of achieving both criteria (circumference of one electrical wavelength at the X band and less than half a free-space wavelength spacing at the Ku band) is to use the dielectric loading effect to reduce the ring's physical size. Calculation shows that a triangular lattice can be used with a material of relative dielectric constant 8.0. However, such a material is not commercially available. Hence, a material with a relative dielectric constant of 3.5 (Kevlar epoxy) and 0.064 cm thick is used as the substrate on both side of the ring elements. In this design, the square lattice is adequate to avoid grating lobes. Although this Kevlar epoxy material has a relatively higher loss tangent, it does not introduce significant insertion loss for the FSS because the RF energy travels only perpendicularly through the very thin substrate instead of parallel along the substrate, as in a microstrip or stripline transmission line. Therefore, for the FSS application, the high-dielectric-constant substrate should be kept thin enough to prevent the generation of surface waves, especially at large incident angles. Note that the surface wave (or Wood's anomaly, discussed later) of an FSS grid embedded in dielectrics will not be eliminated but only pushed higher in frequency if the dielectric is thin. Furthermore, the occurrence of grating lobes depends on the physical size of the lattice and *not* on the presence of dielectrics [41].

1.3 GRATING-LOBE PHENOMENON

Grating or Bragg lobes are undesired secondary main beams occurring at angles with higher-order constructive interference when the lattice size

TABLE 1.2. Periodic Array Lattice Type and Grating-Lobe Criteria (From [32])

LATTICE TYPE	MAX. SPACING	$\theta_0 = 0°$	$\theta_0 = 45°$
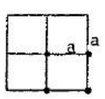 SQUARE SPACING	$\frac{a}{\lambda_0} < \frac{1}{1+\sin\theta_0}$	$\frac{a}{\lambda_0} < 1$	$\frac{a}{\lambda_0} < 0.59$
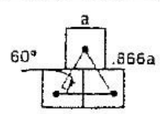 TRIANGULAR SPACING	$\frac{a}{\lambda_0} < \frac{1.15}{1+\sin\theta_0}$	$\frac{a}{\lambda_0} < 1.15$	$\frac{a}{\lambda_0} < 0.67$
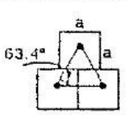 BRICK SPACING	$\frac{a}{\lambda_0} < \frac{1.12}{1+\sin\theta_0}$	$\frac{a}{\lambda_0} < 1.12$	$\frac{a}{\lambda_0} < 0.65$

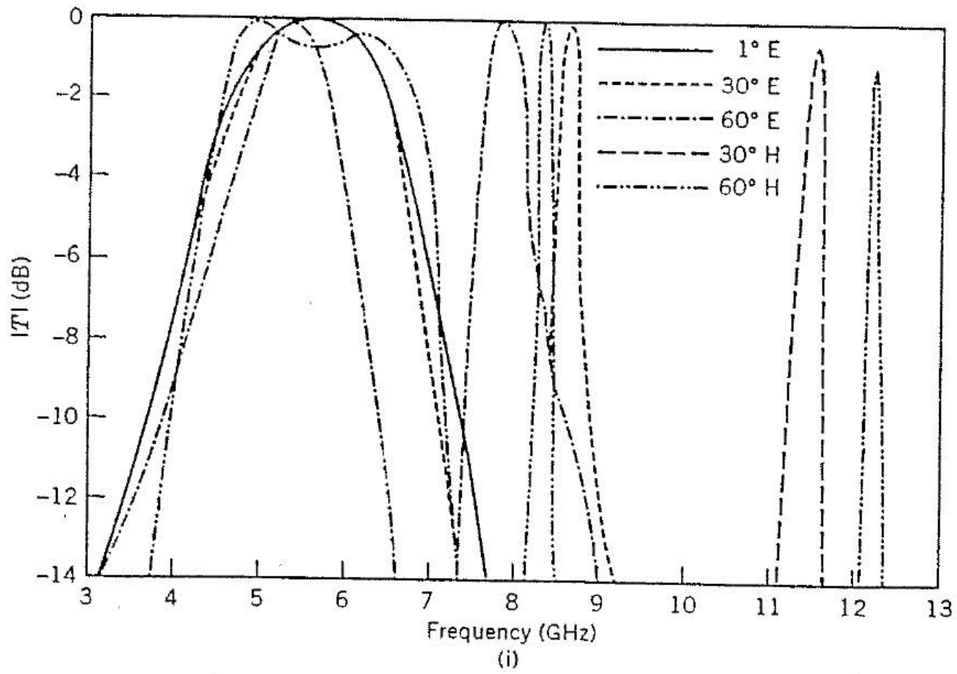

FIGURE 1.6 Transmission performance of a thin-slot FSS (square lattice, period = 1.78 cm, slot length = 1.32 cm, width = 0.128 cm) with dielectrics $\epsilon_r = 4$, thickness = 0.7 and 0.35 cm for case (i) and (ii), respectively) on both sides (© 1978 IEEE).

becomes electrically large. Since period array elements behave similarly to the conventional array, the largest lattice size to avoid grating lobes should obey the same rule that governs a conventional array antenna [8, 9]. A general rule for avoiding grating lobes is that the lattice size should be less than one wavelength for the normal incident case (0° incident angle). For large incident angles, the spacing should be kept below one-half of a free-space wavelength. Table 1.2 lists grating-lobe criteria for square, triangular, and brick lattices. It also shows the maximum lattice size to avoid grating lobes. The square lattice has the most closely packed elements, and the triangular lattice has the largest element spacing. The spacing requirements given in this table prevent the peak of the grating lobe from entering real space. To avoid wasted energy, not even the shoulder region of the grating lobe should enter real space; therefore, the lattice size should be approximately two-thirds or less of that given in Table 1.2.

1.4 WOOD'S ANOMALIES

Wood's anomalies were first observed in the diffraction spectrum of optical gratings in 1902 [44]. They exhibit themselves as rapid variations in the intensity of the various diffracted spectral orders in certain narrow frequency bands, which could not be explained by the grating theory at that time [44]. These anomalies usually occur at frequencies near to or higher than the resonant frequency of any periodic structure. Thus, they have significant impact on the design of periodic structures used in solar filters [45] and FSS radomes [41]. Figure 1.6 (Figures 3 and 5 of Luebbers and Munk [41]) shows the manifestation of these anomalies as the nulls in the transmission characteristics of a slot array. It also shows that the frequency of Wood's anomalies or transmission null decreases as dielectric thickness increases. Further, for a slot array in free space, Wood's anomalies occur just below the frequency at which the grating lobe starts to propagate in real space, which for normal incidence on a rectangular grid array first occurs when the lattice size is one wavelength. It has been shown that these nulls are associated with a surface wave propagating along the surface of the array [41].

1.5 FSS ANALYSIS TECHNIQUES

Numerous methods have been used to analyze FSSs. One of the simplest methods is the equivalent circuit model [26, 27]. In this analysis the various strip segments that form a freestanding patch element in a periodic array are modeled as inductive and capacitive components on a transmission line. From the solution of this circuit, the reflection and transmission coefficients of the FSS screen are found. Since this approach uses the quasi-static approximation to calculate the circuit components, it is only accurate up to

the resonant frequency of the screen. In addition, it cannot model the dielectric loading effects accurately. A sample computer code using this equivalent circuit model is given in the Appendix. The mutual-impedance method (Pelton and Munk [22]), which uses antenna array theory and a knowledge of the mutual impedance between apertures, has also been used successfully.

The modal (or integral equation) method [3, 12, 19, 25, 32, 40, 46] has been the most successful in predicting the performance of periodic structures, particularly in its ability to handle an arbitrary incidence angle. The method begins with the derivation of the integral equation by matching the Floquet modes in space and the aperture or current modes on the periodic surface. The integral equation may be formulated by using the spatial-[12, 19, 32, 40, 41] or the spectral-domain approach [3, 25, 46]. With the spectral-domain approach the complicated integral equation is reduced to a simple algebraic multiplication of simple functions (trigonometric functions and integrals involving them). Next, the method of moments [12] or the conjugate gradient techniques [3] is used to solve the integral equation.

To solve the integral equation, one must reduce the infinite number of equations with an infinite number of unknowns to a finite number of

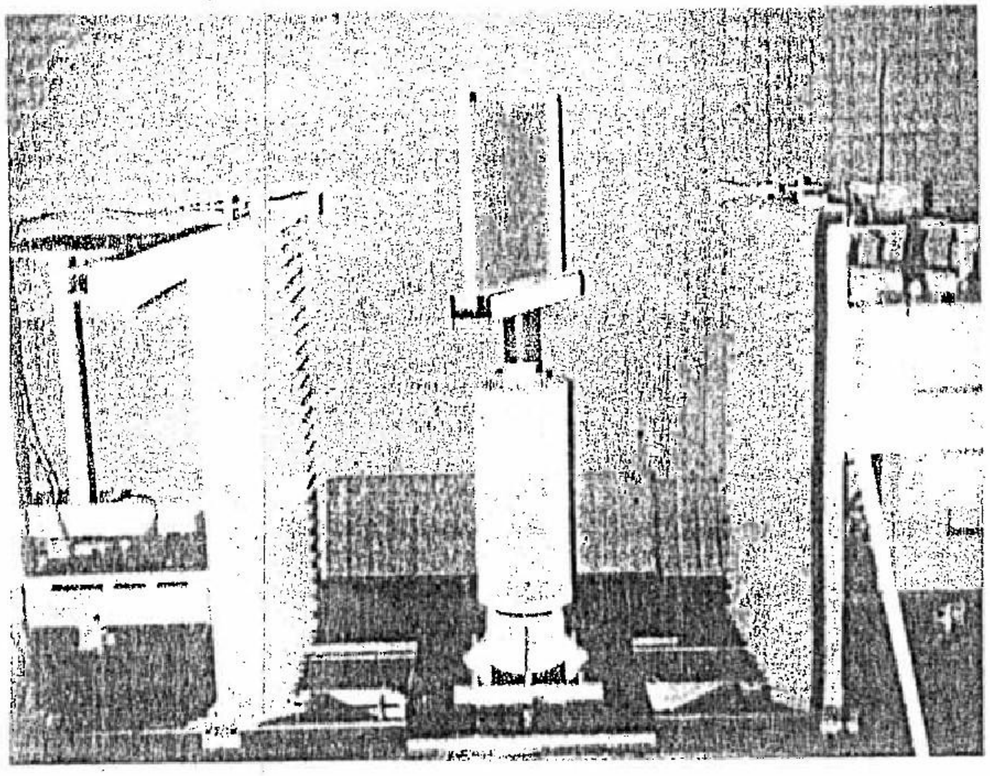

FIGURE 1.7 FSS measurement range.

equations with the same number of unknowns. This must be done in accordance with the relative convergence criteria as indicated in Lee [40]. Further discussion on this subject is given in Chapters 2, 3, and 5.

1.6 MEASUREMENT TECHNIQUES

Various methods have been used to measure transmission and reflection properties of FSS screens. Transmission performance may be tested at room temperature on finite-sized flat panels in an anechoic chamber, as illustrated in Figure 1.7. The measurement setup (Figure 1.8 [46]) uses standard-gain horns as transmitting and receiving antennas. By turning the horn antenna's polarization from vertical to horizontal, one can measure TE and TM transmission characteristics of the test panel between the two horns. In principle, this setup should be able to measure the FSS's reflection characteristics. However, erroneous data were obtained due to the strong edge diffractions from the test panel. These diffractions may be attributed to the horn antenna's large beamwidth and the relatively small FSS panel size.

The waveguide simulation technique [47], used routinely in impedance-matching testing of phased array antennas, provides an alternative for measuring the FSS transmission/reflection performance. However, (1) it is *de-*

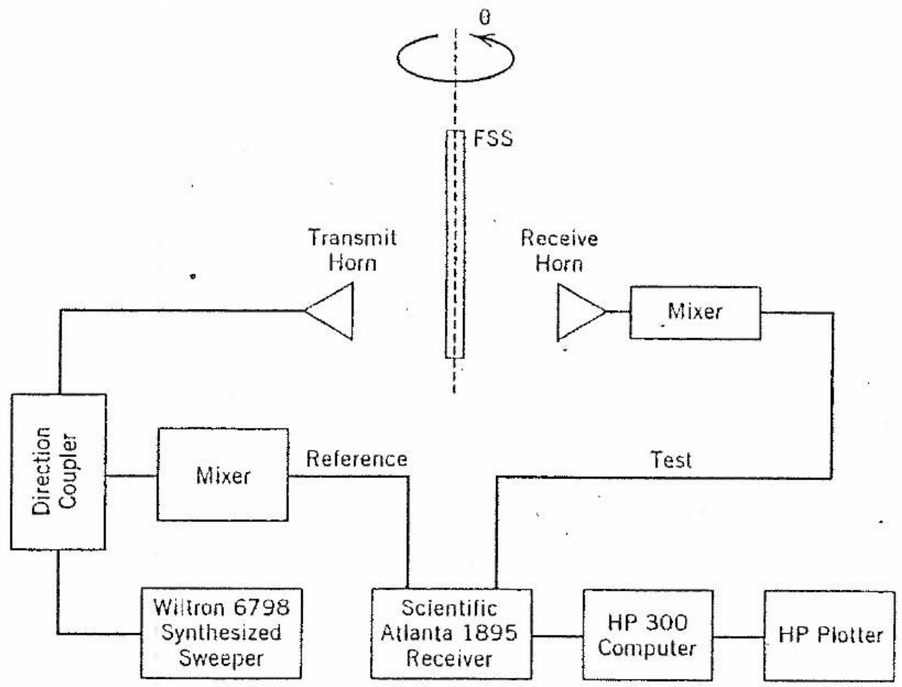

FIGURE 1.8 FSS transmission measurement setup.

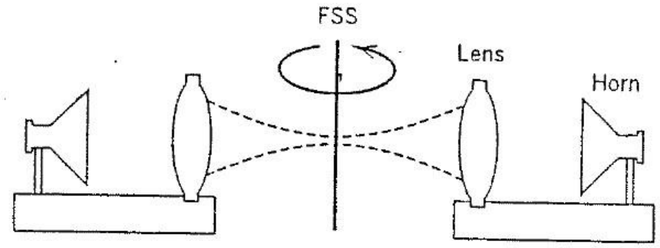

FIGURE 1.9 Precision FSS measurement setup.

structive (i.e., an FSS test sample has to be cut out to fit tightly inside the cross section of the test waveguide), (2) the effective incident angle on the FSS sample changes as the frequency is swept over the waveguide's operating band, and (3) it is limited for TE polarization, since the precise TM waveguide simulator test is very difficult to perform. Despite these limitations, this method is often used to spot-check FSS performance and to provide simple validation checks for FSS analysis/design software.

Finally, the precision setup with horn and lens antennas [48, 49], as shown in Figure 1.9, can be used for *nondestructive* measurements of the FSS transmission and reflection performance with TE and TM polarizations. Since the FSS test panel is illuminated by the narrow Gaussian beam of the lens, the edge diffraction effect is reduced significantly. In addition, large-incident-angle tests can be readily conducted with this approach.

1.7 APPLICATIONS

Periodic structures have a myriad of applications and have contributed significantly toward advancing our living standards. A good example is the screen door of a microwave oven, consisting of a periodic array of metallic holes designed for reflecting microwave energies at 2.45 GHz while allowing light to pass through. This allows us to see the food being cooked inside the oven.

In a dual-reflector antenna system; an FSS can be used as the subreflector. Different frequency feeds are optimized independently and placed at the real and virtual foci of the subreflector. Hence, only a single main reflector is required for multifrequency operation. For example, the FSS on the high-gain antenna (Figure 1.10) of the *Voyager* spacecraft was designed to diplex the S and X bands [21]. The S-band feed is placed at the prime focus of the main reflector, and the X-band feed is placed at the Cassegrain focal point. Note that only one main reflector is required for this two-band operation. Thus, tremendous reductions in mass, volume, and, most important, cost of the antenna system are achieved with the FSS subreflector. For a multifunction reflector antenna, high-performance FSSs are required to diplex two closely

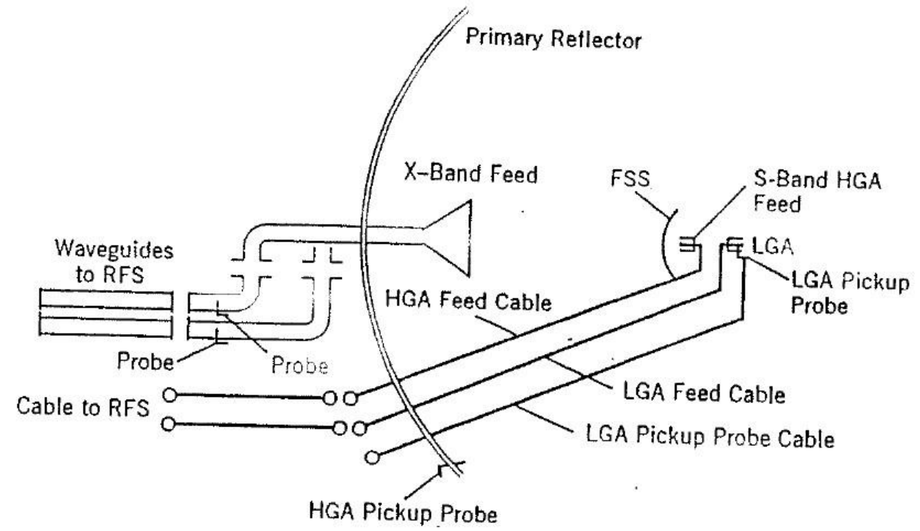

FIGURE 1.10 *Voyager's* dual-frequency reflector antenna with an FSS subreflector.

separated bands or to multiplex three or four bands (discussed in Chapter 4). Further, a dual-frequency, equal-beamwidth, compound reflector antenna (Figure 1.11) has been developed by placing a high-pass FSS at the rim of the solid reflector [50].

Frequency selective surface radomes [51–53] with aperture-type element can be tuned to provide bandpass characteristics. In other words, at the operating (in-band) frequency of the antenna the signal passes through the

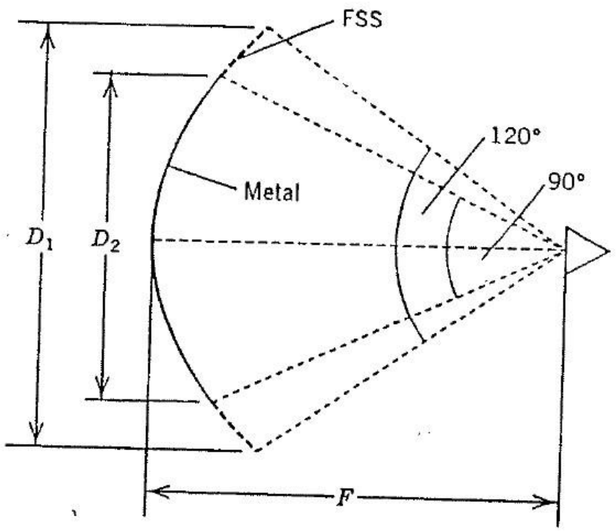

FIGURE 1.11 Compound reflector antenna with an FSS rim (From [50]).

radome with minimum insertion loss, whereas at the out-of-band frequencies the signal is reflected, The radome can usually be designed to blend with the skin of the vehicle so that minimum scattering is achieved. A detailed description of thick- and thin-screen FSS radome is given in Chapter 5.

The effect of the incident angle on the transmitted wave through an aperture-element FSS allows it to be used as a spatial filter [54]. Figure 1.12

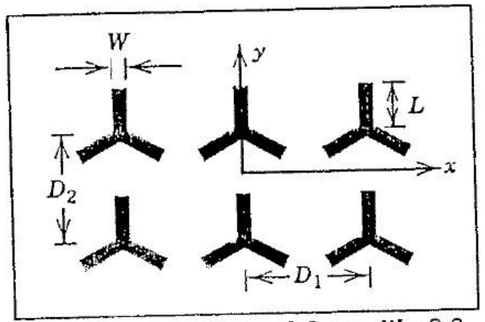

$D_1 = D_2 = 8.9$ mm, $L = 2.0$ mm, $W = 0.2$

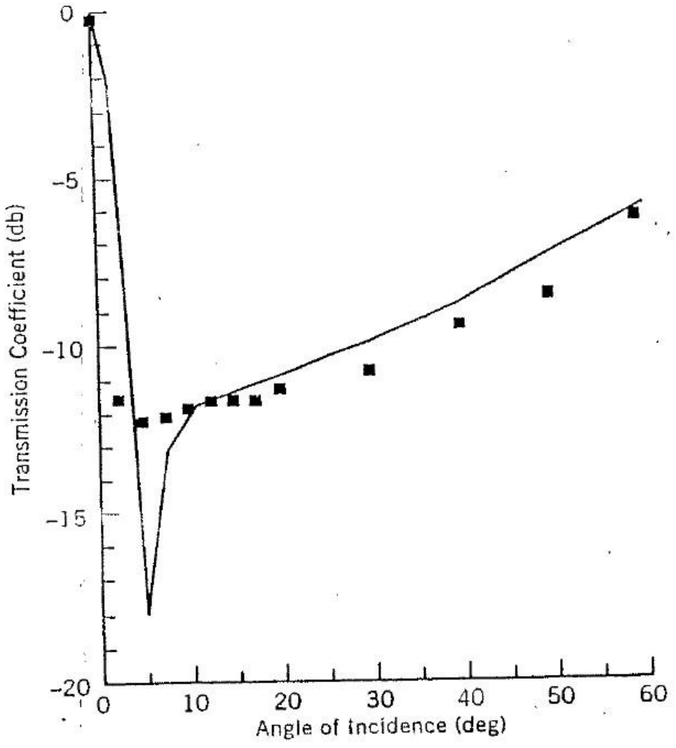

FIGURE 1.12 Angular filtering performance of a tripole slot-element array TM incidence (From Ref. 55 © Wiley, 1993).

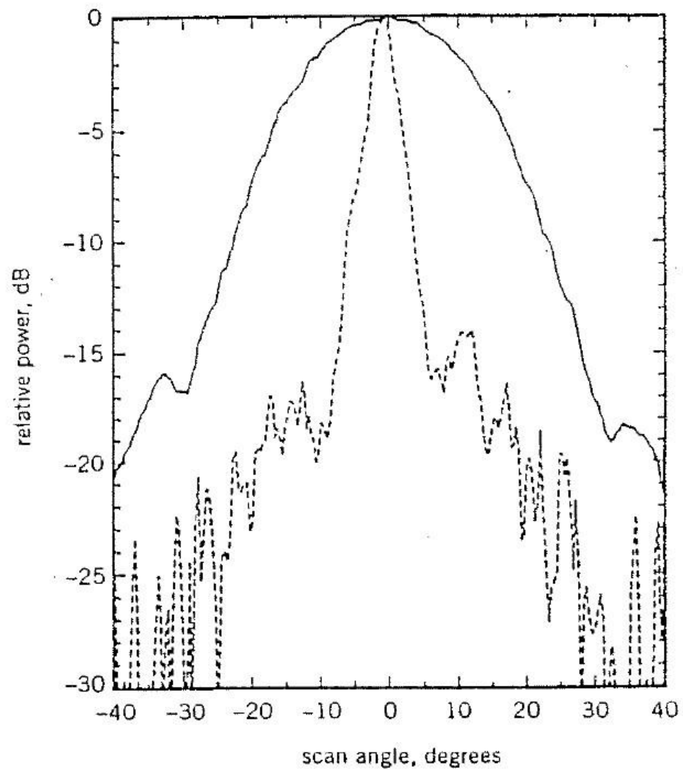

FIGURE 1.13 Horn antenna radiation pattern with (dashed line) and without (solid line) the angular filter of Figure 1.12 (From [55] © Wiley, 1993).

shows the angular filtering characteristics of tripole slot FSS [55]. The spatial filter has applications in sidelobe suppression and beam forming of antenna systems, as shown in Figure 1.13. Other spatial filters are periodic strips [54], FSSs with circular holes [56], cross-dipole slots [55], and microstrip patches [52].

The feasibility of frequency scanning via periodic structures has been demonstrated in Johansson *et al.* [57–61]. The idea is to design the grids (blazed grating) so that the first-order diffracted wave will propagate and serve as a frequency-scanned beam (Figure 1.14) while the specular reflected beam is suppressed. Johansson found that circular-ring patch-element grids [61] give high blazing efficiency (power conversion from incident field to the diffracted field) with circular polarization for a broader bandwidth than does the cross-dipole element [60].

Thick rectangular or circular aperture-element FSSs have been designed for collecting solar energy [45, 62]. This type of FSS is a bandpass screen; that is, it is essentially transparent in the frequency band where the solar cells are most efficient, and it reflects at frequencies outside this band. In the far-infrared region, passive quasi-optical grids are used as beam splitters and

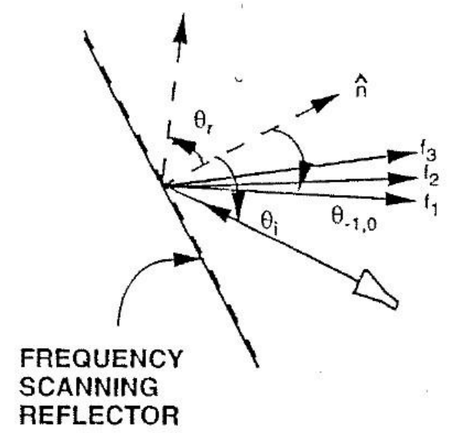

FIGURE 1.14 Frequency scanning reflector antenna with a blazed grating (From [60] © 1989 IEEE).

mirrors [1, 63] for improving pumping efficiency in molecular lasers. A laser cavity mirror is usually a rectangular-mesh grid designed to totally reflect at the wavelength of the energy used to pump the cavity and to partially transmit (0% to 40%) at the lasing wavelength. Since no energy used in the laser pumping is lost at the mirror, the efficiency of the system is optimized. Another interesting quasi-optical application is the use of a sun shield as a thermal control cover of spacecraft antennas [63]. The sun shield consists of a square lattice array of vacuum-deposited aluminum square patches on a thin Kapton film. This grid not only provides for sunlight blockage but also allows for RF signal transmission.

Finally, active grid arrays may be the heart of future low-cost, high-power, solid-state communication, broadcast, and radar systems [4]. Various grid arrays have been demonstrated, including detectors, phased shifters, multipliers, oscillators, amplifiers, and switches [4–7]. In these grid arrays (1) the power is proportional to the area, and (2) the equivalent circuit impedance is determined by the dimensions of the unit cell. These allow great design flexibility. Thus, they provide not only high power and efficiency simultaneously but large dynamic range and low noise. Further discussion on this grid array can be found in Chapters 7 and 8.

REFERENCES

1. R. Ulrich, Far-infrared properties of metallic mesh and its complementary structure. *Infrared Phys.* 7, 37–55 (1967).
2. S. W. Lee, G. Zarrillo, and C. L. Law, Simple formulas for transmission through periodic metal grids or plates. *IEEE Trans. Antennas Propag.* **AP-30**, 904–909 (1982).

3. R. Mittra, C. Chan, and T. Cwik, Techniques for analyzing frequency selective surfaces—a review. *IEEE Proc.* **76**(23), 1593–1615 (1988).
4. J. W. Mink and D. B. Rutlege, Guest editors' overview. Special issue on quasi-optical techniques. *IEEE Trans. Microwave Theory Tech.* **MTT-41**(10), 1661 (1993).
5. W. W. Lam et al., Millimeter-wave diode-grid phase shifters. *IEEE Trans. Microwave Theory Tech.* **MTT-36**(5), 902–907 (1988).
6. R. J. Langley and E. A. Parker, An equivalent circuit study of a PIN diode switches active FSS. Feb. (1990).
7. H. King, et al., Millimeter-wave quasi-optical active arrays. *Proc. Int. Conf. Space Terahertz Tech., 2nd, 1991*, pp. 293–305 (1991).
8. N. Amitay, V. Galindo, and C. P. Wu, *Theory and Analysis of Phased Array Antennas*. Wiley, New York, 1972.
9. A. A. Oliner and G. H. Knittel, eds., *Phased Array Antennas*. Artech House, Norwood, MA, 1972.
10. P. S. Simon et al., Full-wave analysis of an infinite, planar array of linearly polarized, stripline-fed tapered notch elements. *Int. IEEE Antennas Propag. Symp. Dig.*, London, Ontario, Canada, *1991*, pp. 334–337 (1991).
11. E. J. Kuster, et al., Triangular surface-patch modeling for phased arrays and other planar periodic structures with arbitrary elements. *J. Electromagn. Waves Appl.* **6**(12), 1607–1619 (1992).
12. C. C. Chen, Transmission of microwave through perforated flat plates of finite thickness. *IEEE Trans. Microwave Theory Tech.* **MTT-21**(1), 1–6 (1973).
13. R. J. Langley and E. A. Parker, Geometry of wavelengths in a dichroic secondary mirror. *Electron. Lett.* **14**, 443–445 (1978).
14. J. J. Fratamico et al., A wide-scan-quasi-optical frequency diplexer. *IEEE Trans. Microwave Theory Tech.* **MTT-30**, No. 1, 20–27 (1982).
15. R. C. Compton et al., Diffraction properties of a bandpass grid. *Infrared Phys.* **23**(5), 239–245 (1983).
16. P. D. Potter, Improved dichroic reflector design for the 64-m antenna S- and X-band feed systems. *JPL Tech. Rep.*, 32–1526, February, (1974).
17. R. H. Ott et al., Scattering by a two-dimensional periodic array of narrow plates. *Radio Sci.* **2**(11), 1347–1359 (1967).
18. C. C. Chen, Scattering by a two-dimensional periodic array of conducting plates. *IEEE Trans. Antennas Propag.* **AP-18**(5), 660–665 (1970).
19. J. P. Montgomery, Scattering by an infinite periodic array of conductors on a dielectric sheets. *IEEE Trans. Antennas Propag.* **AP-23**(1), 70–75 (1975).
20. S. W. Schneider and B. A. Munk, The scattering properties of super dense arrays of dipoles. *IEEE Trans. Antennas Propag.* **AP-42**(2), 463–472 (1994).
21. G. H. Schennum, Frequency-selective surfaces for multiple frequency antennas. *Microwave J.* **16**(5), 55–57 (1973).
22. E. L. Pelton and B. A. Munk, Scattering from periodic arrays of crossed dipoles. *IEEE Trans. Antennas Propag.* **AP-27**(3), 323–330 (1979).
23. V. Agrawal and W. A. Imbriale, Design of a dichroic Cassegrain subreflector. *IEEE Trans. Antennas Propag.* **AP-27**(4), 466–473 (1979).

24. S. M. A. Hamdy and P. A. Parker, Influence of lattice geometry on transmission of electromagnetic waves through arrays of crossed dipoles. *IEE Proc., Part H: Microwaves, Opt. Antennas* **129**(1), 7–10 (1982).

25. C. H. Tsao and R. Mittra, Spectral-domain analysis of frequency selective surfaces comprised of periodic arrays of cross dipoles and Jerusalem crosses. *IEEE Trans. Antennas Propag.* **AP-32**(5), 478–486 (1984).

26. I. Anderson, On the theory of self-resonant grids. *Bell Syst. Tech. J.* **54**(10), 1725–1731 (1975).

27. R. J. Lagley and A. J. Drinkwater, Improved empirical model for the Jerusalem cross. *IEE Proc., Part H: Microwaves, Opt. Antennas* **129**(1), 1–6 (1982).

28. E. L. Pelton and B. A. Munk, A streamlined metallic radome. *IEEE Trans. Antennas Propag.* **AP-22**(6), 799–803 (1974).

29. B. A. Munk, Periodic surface for large scan angle. U.S. Pat. 3,789,404 (1974).

30. E. A. Parker and S. M. A. Handy, Rings as elements for FSS. *Electron. Lett.* **17**(17), August, pp. 612–614 (1981).

31. E. Parker, S. Hamdy, and R. Langley, Arrays of concentric rings as frequency selective surfaces. *Electron. Lett.* **17**(23), 880 (1981).

32. J. Huang, T. K. Wu, and S. W. Lee, Tri-band FSS with circular ring elements. *IEEE Trans. Antennas Propag.* **AP-42**(2), 166–175 (1994).

33. T K. Wu and S. W. Lee, Multi-band FSS with multi-ring patch elements. *IEEE Trans. Antennas Propag.* **AP-42**(11), 1484–1490 (1994).

34. R. J. Langley and E. A. Parker, Equivalent circuit model for arrays of square loops. *Electron. Lett.* **18**(7), 294–296 (1982).

35. R. J. Langley and E. A. Parker, Double-square frequency-selective surfaces and their equivalent circuit. *Electron. Lett.* **19**(17), 675 (1983).

36. C. K. Lee and R. Langley, Equivalent circuit models for frequency selective surfaces at oblique angle of incidence. *IEE Proc., Part H: Microwaves, Antennas Propag.* **132**(6), 395–398 (1985).

37. T. K. Wu, Single screen triband FSS with double-square-loop elements. *Microwave Opt. Tech. Lett.* **5**(2), 56–59 (1992).

38. H. Rosen, U.S. Pat. 4,785,310 (1988).

39. E. A. Parker et al., FSS. Proceeding ICAP 83, *IEE Conf. Publ.* **219**, 459–463 (1983).

40. S. W. Lee, Scattering by dielectric-loaded screen. *IEEE Trans. Antennas Propag.* **AP-19**(5), 656 (1971).

41. R. J. Luebbers and B. A. Munk, Some effects of dielectric loading on periodic slot arrays. *IEEE Trans. Antennas Propag.* **AP-26**(4), 536–542 (1978).

42. P. Callaghan, E. Parker, and R. Langley, Influence of supporting dielectric layers on the transmission properties of frequency selective surfaces. *IEE Proc., Part H: Microwaves, Antennas Propag.* **138**(5), 448–454 (1991).

43. T. K. Wu, Two layer matching dielectrics for radomes and lenses for wide angles of incidence. U.S. Pat. 5,017,939 (1991).

44. A. Hessel and A. A. Oliner, A new theory of Wood's anomalies on optical gratings. *Appl. Opt.* **4**(10), 1275–1297 (1965).

45. J. Bliek et al., Inductive grids in the region of diffraction anomalies, theory, experiment, and applications. *IEEE Trans. Microwave Theory Tech.* **MTT-28**(10), 1119–1125 (1980).

46. T. Cwik et al., Frequency selective surfaces. *IEEE Antennas Propag. Newsl.*, Feature Article, April (1987).

47. P. W. Hannan and M. A. Balfour, Simulation of a phased array antenna in waveguide. *IEEE Trans. Antennas Propag.* **AP-13**, 342 (1965).

48. D. K. Ghodgaonka, V. V. Varadan, and V. J. Varadan, A free-space method for measurement of dielectric constants and loss tangents at microwave frequencies. *IEEE Trans. Instrum. Meas.* **IM-37**(3), 789–793 (1989).

49. G. Arjavalingam et al., Characterization of quasi-optical filters with picosecond transient radiation. *IEEE Trans. Antennas Propag.* **AP-40**(1), 63–66 (1992).

50. C. K. Lee, R. J. Langley, and E. A. Parker, Compound reflector antennas. *IEE Proc., Part H: Microwaves, Antennas Propag.* **139**(2), 135–138 (1992).

51. B. A. Munk et al., Transmission through a two-layer array of loaded slots. *IEEE Trans. Antennas Propag.* **AP-22**(6), 804–809 (1974).

52. R. Pous and D. M. Pozar, FSS using aperture coupled microstrip patches. *Electron. Lett.* **25**(17), 1136–1138 (1989).

53. T. K. Wu, High Q bandpass structure for the selective transmission and reflection of high frequency signals. U.S. Pat. 5,103,241 (1992).

54. P. R. Franchi and R. J. Mailloux, Theoretical and experimental study of metal grid angular filters for sidelobe suppression. *IEEE Trans. Antennas Propag.* **AP-24**, 174–181 (1976).

55. S. Chandran and J. C. Vardaxoglou, Performance of two single layer FSS as spatial filter. *Microwave Opt. Tech. Lett.* **6**(6), 339–342 (1993).

56. E. L. Rope and G. Tricoles, An angular filter containing three periodically perforated metallic layers. *Int. IEEE Antennas Propag. Symp. Dig.*, Seattle, WA, *1979*, pp. 818–820 (1979).

57. E. V. Jull and N. C. Beaulieu, An unusual reflection grating behavior suitable for efficient frequency scanning. *IEEE Antennas Propag. Symp. Dig.*, Quebec, Canada, *1980*, pp. 189–191 (1980).

58. J. Shmoys and A. Hessel, Analysis and design of frequency scanned transmission gratings. *Radio Sci.* **18**(4), 512–518 (1983).

59. F. S. Johansson, L. G. Josefsson, and T. Lorentzon, A novel frequency scanned reflector antenna. *IEEE Trans. Antennas Propag.* **AP-37**(8), 984–989 (1989).

60. F. S. Johansson, Frequency scanned gratings consisting of photo-etched arrays. *IEEE Trans. Antennas Propag.* **AP-37**(8), 996–1002 (1989).

61. F. S. Johansson, Frequency scanned reflector gratings consisting of ring patches. *IEE Proc., Part H: Microwaves, Antennas Propag.* **138**(4), 273–276 (1991).

62. R. C. McPhedran and D. Maystre, On the theory and solar application of inductive grids. *Appl. Phys.* **14**, 1–20 (1977).

63. T. K. Wu, Quasi-optical grids with thin rectangular patch/aperture elements. *Int. J. Infrared Millimeter Waves* **14**(5), 1017–1033 (1993).

APPENDIX

FORTRAN

Computer Code for Gridded Square-Loop, Square-Loop, or Double-Square-Loop Patch-Element FSS

```
      PROGRAM ECM
C**********************************************************************
C*TO FIND THE FREQUENCY CHARACTERISTICS OF AN FSS WITH GRIDDED-SQUARE
C*LOOP, SQUARE-LOOP AND DOUBLE SQUARE-LOOP PATCH ELEMENTS USING THE
C*EQUATIONS GIVEN IN REFERENCES [34-36].
C*WRITTEN BY TE-KAO WU 8-01-94.
C*
C     *variables: (all dimensions are in inches)
C     *NF: number of frequency points (integer)
C     *FI: beginning frequency (GHz)
C     *DF: Frequency increment (GHz)
C     *ER: effective dielectric constant of the substrate
C     *F:  Frequency (GHz)
C     *PR: reflected power
C     *PT: transmitted power
C     *RDB: reflected power (dB)
C     *TDB: transmitted power (dB)
C     *P: period of the unit cell
C     *
C     *LS = 1 for gridded square-loop patch element FSS
C     *W1: strip width of the grid
C     *W2: strip width of the square-loop
C     *D:  Length of the square-loop side
C     *G:  gap width between the grid and the square-loop
C     *
C     *LS = 2 for square-loop patch element FSS
C     *W: strip width of the square-loop
C     *G: gap width between two square-loop elements
C     *
C     *LS = 3 for double square-loop patch element FSS
C     *W1: strip width of the outer-loop
C     *W2: strip width of the inner-loop
C     *G1: gap width between two double square-loop elements
C     *G2: gap width between the outer and inner loops
C**********************************************************************
      open(5,file='ein.dat')
      open(6,file='eou.dat')
      DIRT=.0001
      READ(5,*)LS,NF,FI,DF
      IF(LS.EQ.2)GO TO 51
      IF(LS.EQ.3)GO TO 52
      WRITE(6,*)"THIS IS GRIDDED SQUARE-LOOP FSS DESIGN"
      READ(5,*)P,W1,W2,D,G,ER
      WRITE(6,1)P,W1,W2,D,G,ER
1     FORMAT(5X,"P",5X,"W1",4X,"W2",4X,"D1",4X,"G1",4X,"ER"
     &/6F6.3)
      W2=w2*2.
```



```
2     FORMAT(/5X,"F",9X,"PR",8X,"PT",8X,"RDB",7X,"TDB"/)
      GO TO 53
51    CONTINUE
      WRITE(6,*)"THIS IS SQUARE-LOOP FSS DESIGN"
      READ(5,*)P,W,G,ER
      D=P-G
      WRITE(6,9)P,W,D,G,ER
9     FORMAT(3X,'P',5X,'W',4X,'D',4X,'G',4X,'ER'
     &/6F6.3)
      w2=w*2.
      GO TO 53
52    CONTINUE
      WRITE(6,*)"THIS IS DOUBLE-SQUARE-LOOP FSS DESIGN"
      READ(5,*)P,W1,D1,G1,ER
      READ(5,*)W2,D2,G2
      WRITE(6,8)P,W1,D1,G1,ER
      WRITE(6,4)W2,D2,G2
4     FORMAT(/5X,"W2",4X,"D2",4X,"G2"/3F7.4)
8     FORMAT(5X,"P",5X,"W1",4X,"D1",4X,"G1",4X,"ER"
     &/6F7.4)
      wt=w2*2.
53    continue
      Write(6,2)
      DOP=D/P
      DO 11 I=1,NF
      F=FI+DF*(I-1)
      WL=11.8/F
      IF(LS.EQ.2)GO TO 55
      IF(LS.EQ.3)Go TO 56
      X3=XG(P,W2,WL)*DOP
      X2=XG(P,W1,WL)
      C1=XG(P,G,WL)
      B1=2.*ER*DOP*C1
      X1=2.*X2*X3/(X2+X3)
      BT=1./X2+1./(X1-1./B1)
      GO TO 54
55    CONTINUE
      X3=XG(P,W2,WL)*DOP
      C1=XG(P,G,WL)
      B1=4.*ER*DOP*C1
      BT=1./(X3-1./B1)
      GO TO 54
56    CONTINUE
      d1p=d1/p
      d2p=d2/p
      Z2=XG(P,W2,WL)
      Z1=XG(P,W1,WL)
      X1=2.*D1P*Z1*Z2/(Z1+Z2)
      X2=D2P*XG(P,WT,WL)
      C1=XG(P,G1,WL)*4.
      B1=.75*ER*D1P*C1
      C2=4.*XG(P,G2,WL)
      B2=ER*D2P*C1*C2/(C1+C2)
      BT=1./(X1-1./B1)+1./(X2-1./B2)
54    PT=1./(1.+.25*BT*BT)
      PR=1.-PT
```

```
      IF(PT.LT.DIRT)PT=DIRT
      IF(PR.LT.DIRT)PR=DIRT
      RDB=10.*ALOG10(PR)
      TDB=10.*ALOG10(PT)
      WRITE(6,3)F,PR,PT,RDB,TDB
11    CONTINUE
3     FORMAT(5F10.4)
      STOP
      END
      FUNCTION XG(P,W,WL)
      HPI=1.5708
      A1=HPI/P
      DL=D/WL
      PL=P/WL
      WA=W/WL
      CS1=1./SIN(A1*W)
      XG=PL*(ALOG(CS1)+FF(PL,WA))
      RETURN
      END
      FUNCTION FF(P,W)
      CA=COS(1.5708*W/P)
      C=CA*CA
      S=1.-C
      Q=(1./SQRT(1.-P*P))-1.
      F1=Q*C*C/(1.+Q*S*S)
      F2=P*C*.25*(1.-3.*S)
      FF=F1+F2*F2
      RETURN
      END
```

Sample Run #1

Input File

```
1,17,1.,1.
0.3543,.022,.0443,.35,.022,1.00
```

Output File

```
 THIS IS GRIDDED SQUARE-LOOP FSS DESIGN
     P      W1     W2     D1     G1     ER
  .354   .022   .044   .350   .022 1.000

     F          PR         PT         RDB        TDB

   1.0000     .9804      .0196     -.0858   -17.0850
   2.0000     .9217      .0783     -.3542   -11.0611
   3.0000     .8235      .1765     -.8434    -7.5324
   4.0000     .6856      .3144    -1.6396    -5.0245
   5.0000     .5088      .4912    -2.9349    -3.0871
   6.0000     .3013      .6987    -5.2093    -1.5574
   7.0000     .0984      .9016   -10.0690     -.4500
   8.0000     .0001      .9999   -40.0000     -.0004
   9.0000     .1513      .8487    -8.2030     -.7122
  10.0000     .5141      .4859    -2.8899    -3.1341
  11.0000     .8286      .1714     -.8167    -7.6593
  12.0000     .9747      .0253     -.1111   -15.9764
  13.0000     .9981      .0019     -.0082   -27.2586
  14.0000     .9602      .0398     -.1762   -14.0045
  15.0000     .8969      .1031     -.4726    -9.8672
  16.0000     .8253      .1747     -.8340    -7.5767
  17.0000     .7532      .2468    -1.2312    -6.0758
```


Sample Run #2

Input File

```
2,18,2.,1.
0.353,.012,.115,1.12
```

Output File

```
 THIS IS SQUARE-LOOP FSS DESIGN
    P      W     D     G     ER
  .353   .012   .238   .115 1.120

     F          PR         PT         RDB        TDB

   2.0000     .0043      .9957    -23.7105     -.0185
   3.0000     .0098      .9902    -20.0672     -.0430
   4.0000     .0182      .9818    -17.3962     -.0798
   5.0000     .0300      .9700    -15.2328     -.1322
   6.0000     .0460      .9540    -13.3685     -.2047
   7.0000     .0678      .9322    -11.6900     -.3047
   8.0000     .0971      .9029    -10.1288     -.4435
   9.0000     .1368      .8632     -8.6399     -.6388
  10.0000     .1908      .8092     -7.1941     -.9195
  11.0000     .2645      .7355     -5.7753    -1.3343

  12.0000     .3645      .6355     -4.3835    -1.9686
  13.0000     .4963      .5037     -3.0430    -2.9779
  14.0000     .6584      .3416     -1.8153    -4.6644
  15.0000     .8298      .1702      -.8105    -7.6893
  16.0000     .9613      .0387      -.1714   -14.1237
  17.0000     .9984      .0016      -.0071   -27.8726
  18.0000     .9305      .0695      -.3130   -11.5777
  19.0000     .7994      .2006      -.9725    -6.9760
```

Sample Run #3

Input File

```
3,17,1.,1.
0.288,.009,.279,.009,1.0
.009,.189,.036
```

Output File

```
 THIS IS DOUBLE-SQUARE-LOOP FSS DESIGN
     P      W1     D1     G1     ER
  .2880  .0090  .2790  .0090 1.0000

     W2     D2     G2
  .0090  .1890  .0360

     F          PR         PT         RDB        TDB

   1.0000     .0199      .9801    -17.0038     -.0875
   2.0000     .0808      .9192    -10.9266     -.3658
   3.0000     .1851      .8149     -7.3260     -.8889
   4.0000     .3346      .6654     -4.7546    -1.7692
   5.0000     .5249      .4751     -2.7995    -3.2319
   6.0000     .7353      .2647     -1.3351    -5.7730
   7.0000     .9180      .0820      -.3715   -10.8630
   8.0000     .9999      .0001      -.0006   -38.4182
   9.0000     .9195      .0805      -.3644   -10.9435
  10.0000     .6826      .3174     -1.6580    -4.9846
  11.0000     .3737      .6263     -4.2751    -2.0320
  12.0000     .1114      .8886     -9.5306     -.5130
  13.0000     .0003      .9997    -34.9848     -.0014
  14.0000     .0927      .9073    -10.3293     -.4225
  15.0000     .3492      .6508     -4.5698    -1.8652
  16.0000     .6467      .3533     -1.8927    -4.5191
  17.0000     .8697      .1303      -.6065    -8.8495
```

CHAPTER TWO

Analysis of Frequency Selective Surfaces

CHI H. CHAN, Department of Electrical Engineering, University of Washington, Seattle, Washington 98195

We discuss a number of techniques for analyzing frequency selective surfaces (FSS). The formulation is based on constructing an integral equation for a single unit cell. The integral equation is modified for periodic cells by the application of Floquet's theorem such that the continuous convolution integral is converted to an infinite summation with each summand being a product of the spectral Green's function and the spectral equivalent surface current. This modified integral equation is discretized into a system of linear equations in the context of the method of moments. Various basis and weighting functions are discussed in conjunction with the choice of a matrix solution. A general procedure of deriving the spectral Green's functions is provided. Illustrative numerical examples are given for various FSS structures discussed.

2.1 FORMULATION OF A FREESTANDING FSS

The technology of frequency selective surfaces has a long history of development since the first grating made of equally spaced hairs was reported by the

Frequency Selective Surface and Grid Array, Edited by T. K. Wu
ISBN 0-471-31189-8

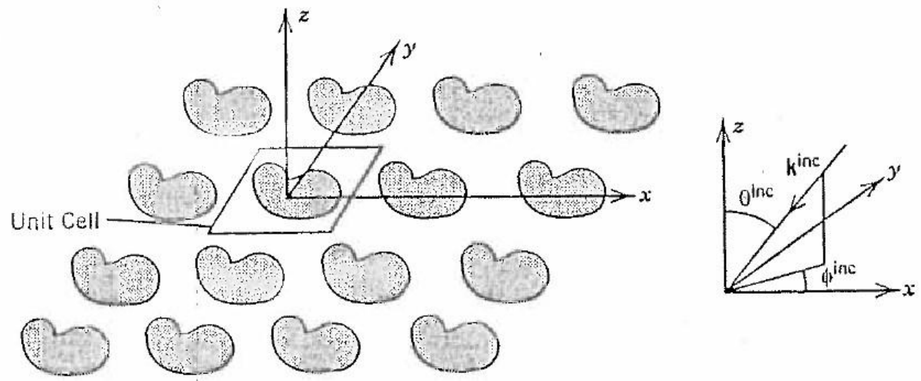

(a)

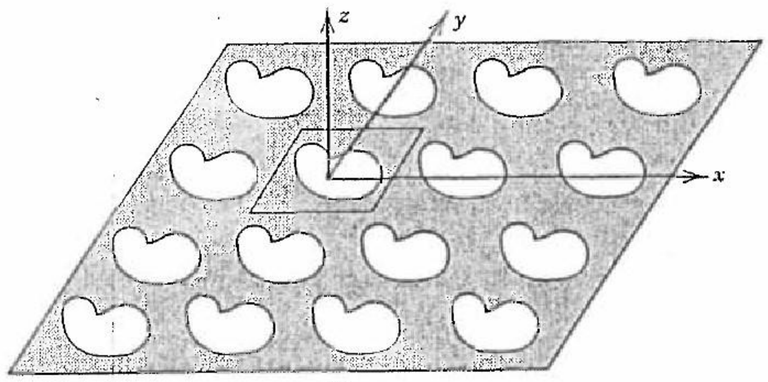

(b)

FIGURE 2.1 Freestanding frequency selective surfaces: (a) conducting patches; (b) apertures.

American physicist David Rittenhouse more than 200 years ago [1]. Contemporary FSSs comprise periodically arranged metallic patch elements or aperture elements within a metallic screen and exhibit resonances at which total reflection (patches) or total transmission (apertures) occurs. Example patch and aperture geometries are shown in Figure 2.1.

Extensive analytic research has been performed to predict the reflection and transmission properties of FSSs. Mittra et al. [2] provides a long list of references pertaining to analyses of FSS; some of the important contributions are cited here as well [3–47]. Based on this extensive body of work, techniques are now available to model FSSs efficiently in a wide range of physical configurations. In this chapter, the techniques currently being used are discussed. Several assumptions have been made: (i) the FSS is infinite in extent, so diffraction from the edges of the surface in a practical situation is ignored, (ii) the incident radiation is a monochromatic plane wave (other sources can be treated as a summation of plane waves), and (iii) the

conducting screen is infinitesimally thin, except for a finite-thickness aperture screen.

The first step in formulating the problem of electromagnetic scattering from an FSS is to relate the fields scattered from the FSS to the surface currents induced on the screen by the incident field. Initially, we consider the scattering of a single freestanding, perfectly conducting patch lying on the x-y plane, as shown in Figure 2.2. We will show how the integral equation corresponding to a single patch is modified to include the contributions from an array of patches. Later we indicate how this formulation can be modified to handle multiple FSS screens (with finite or infinite conductivities) embedded in a layered medium.

The scattered field from a conducting patch on the x-y plane due to an incident plane wave can be calculated from the induced current on the patch radiating in free space. The scattered field at point $\mathbf{r}$ due to a source $\mathbf{r}'$ is [48]

$$\mathbf{E}^s = -j\omega\mu_0\mathbf{A} + \frac{1}{j\omega\epsilon_0}\nabla(\nabla\cdot\mathbf{A}), \tag{2.1}$$

where

$$\mathbf{A}(\mathbf{r}) = \int G(\mathbf{r},\mathbf{r}')\mathbf{J}(\mathbf{r}')\,dr' = G^*\mathbf{J}, \tag{2.2}$$

$$G(\mathbf{r},\mathbf{r}') = \frac{e^{-jk_0|\mathbf{r}-\mathbf{r}'|}}{4\pi|\mathbf{r}-\mathbf{r}'|}, \tag{2.3}$$

k_0 is the wave number $k_0 = \omega\sqrt{\mu_0\epsilon_0}$, the asterisk represents a convolution operation, $\mathbf{J}$ is the induced surface current on the conductor, and G is the free-space Green's function. On the conducting patch, the tangential electric field, denoted by a subscript t, vanishes:

$$\mathbf{E}_t = \mathbf{E}_t^s + \mathbf{E}_t^{\text{inc}} = 0. \tag{2.4}$$

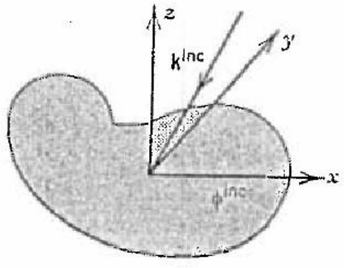

FIGURE 2.2 Scattering from a single conducting patch.

The superscripts s and inc correspond to the scattered and incident fields, respectively. Subsequently Eq. (2.1) becomes

$$\mathbf{E}_t^{\text{inc}}(\mathbf{r}) = j\omega\mu_0 \mathbf{A}_t(\mathbf{r}) - \frac{1}{j\omega\epsilon_0}\left[\nabla(\nabla \cdot \mathbf{A}(\mathbf{r}))\right]_t. \tag{2.5}$$

Equation (2.5) is the electric-field integral equation (EFIE) [49] for the perfectly electric conducting (PEC) patch. For a planar infinitesimally thin surface only surface current components J_x and J_y exist, and hence, only A_x and A_y are nonzero. Therefore, we have Eq. (2.5) in matrix form as [29]

$$-\begin{bmatrix} E_x^{\text{inc}} \\ E_y^{\text{inc}} \end{bmatrix} = \frac{-j\omega\mu_0}{k_0^2}\begin{bmatrix} k_0^2 + \dfrac{\partial^2}{\partial x^2} & \dfrac{\partial^2}{\partial x\,\partial y} \\ \dfrac{\partial^2}{\partial x\,\partial y} & k_0^2 + \dfrac{\partial^2}{\partial y^2} \end{bmatrix}\begin{bmatrix} A_x \\ A_y \end{bmatrix}, \tag{2.6}$$

where $A_x = G^* J_x$ and $A_y = G^* J_y$. Defining a Fourier transform pair as

$$\tilde{f}(\alpha,\beta) = \int_{-\infty}^{\infty}\int_{-\infty}^{\infty} f(x,y) e^{-j\alpha x} e^{-j\beta y}\,dx\,dy, \tag{2.7}$$

$$f(x,y) = \frac{1}{(2\pi)^2}\int_{-\infty}^{\infty}\int_{-\infty}^{\infty} \tilde{f}(\alpha,\beta) e^{j\alpha x} e^{j\beta y}\,d\alpha\,d\beta, \tag{2.8}$$

one can replace the convolution and partial derivatives appearing in Eq. (2.6) by $G^*\mathbf{J} \leftrightarrow \tilde{G}\tilde{\mathbf{J}}$, $\partial \mathbf{A}/\partial x \leftrightarrow j\alpha \mathbf{A}$, and $\partial \mathbf{A}/\partial y \leftrightarrow j\beta \mathbf{A}$ in the Fourier domain. After taking the inverse Fourier transform to obtain the spatial domain expression, Eq. (2.6) now reads

$$-\begin{bmatrix} E_x^{\text{inc}}(x,y) \\ E_y^{\text{inc}}(x,y) \end{bmatrix} = \frac{1}{2\pi}\int_{-\infty}^{\infty}\int_{-\infty}^{\infty} \frac{1}{j\omega\epsilon_0}\begin{bmatrix} k_0^2 - \alpha^2 & -\alpha\beta \\ -\alpha\beta & k_0^2 - \beta^2 \end{bmatrix}\tilde{\mathbf{G}}\begin{bmatrix} \tilde{J}_x \\ \tilde{J}_y \end{bmatrix} e^{j\alpha x} e^{j\beta y}\,d\alpha\,d\beta, \tag{2.9}$$

where

$$\tilde{\mathbf{G}} = \frac{-j}{2\sqrt{k_0^2 - \alpha^2 - \beta^2}}\mathbf{I} \quad \text{for } k_0^2 > \alpha^2 + \beta^2,$$

$$= \frac{1}{2\sqrt{\alpha^2 + \beta^2 - k_0^2}}\mathbf{I} \quad \text{otherwise } (\mathbf{I} \text{ is an identity tensor}). \tag{2.10}$$

The proper branch of the square root in Eq. (2.10) is chosen to satisfy the radiation condition.

Note that we have formulated the EFIE for a single patch only. To extend the spectral domain method to a periodic array of patches, let us first consider the periodicity in the x direction only. To satisfy Floquet's theorem for periodic structures, the current must be in the form [44, 50]

$$J(x + a) = J(x) e^{jk_x^{\text{inc}} a}, \tag{2.11}$$

where k_x^{inc} and a are the incident wave number and periodicity in the x direction, respectively. Defining a new function $J'(x) = J(x)e^{jk_x^{\text{inc}} a}$, we have

$$J'(x + a) = J(x + a)e^{-jk_x^{\text{inc}}(x+a)} = J(x)e^{jk_x^{\text{inc}} a} e^{-jk_x^{\text{inc}}(x+a)}$$

$$= J(x)e^{-jk_x^{\text{inc}} x} = J'(x). \tag{2.12}$$

Hence, $J'(x)$ is a periodic function with a periodicity of a that can be represented by the sum of its Fourier components:

$$J'(x) = \sum_{m=-\infty}^{\infty} \tilde{J}_m e^{j(2m\pi/a)x}. \tag{2.13}$$

As a result, $J(x)$ can be expressed as

$$J(x) = \sum_{m=-\infty}^{\infty} \tilde{J}_m e^{j(2m\pi/a + k_x^{\text{inc}})x}. \tag{2.14}$$

If we carry out the same procedure with k_y^{inc} and b, the incident wave number and periodicity in the y direction, respectively, Eq. (2.9) reads

$$-\begin{bmatrix} E_x^{\text{inc}}(x,y) \\ E_y^{\text{inc}}(x,y) \end{bmatrix} = \frac{2\pi}{j\omega\epsilon_0 ab}\sum_{m=-\infty}^{\infty}\sum_{n=-\infty}^{\infty}\begin{bmatrix} k_0^2 - \alpha_m^2 & -\alpha_m\beta_n \\ -\alpha_m\beta_n & k_0^2 - \beta_n^2 \end{bmatrix}\tilde{\mathbf{G}}(\alpha_m,\beta_n) \cdot \begin{bmatrix} \tilde{J}_x(\alpha_m,\beta_n) \\ \tilde{J}_y(\alpha_m,\beta_n) \end{bmatrix} e^{j\alpha_m x} e^{j\beta_n y}, \tag{2.15}$$

where

$$\alpha_m = \frac{2m\pi}{a} + k_x^{\text{inc}} \quad \text{and} \quad \beta_n = \frac{2n\pi}{b} + k_y^{\text{inc}}. \tag{2.16}$$

For a skewed grid as depicted in Figure 2.3, the Fourier transform variables have to be redefined through the use of a reciprocal lattice [29, 51]. They are listed here as

$$\alpha_{mn} = \frac{2m\pi}{a} + k_x^{\text{inc}} \quad \text{and} \quad \beta_{mn} = \frac{2n\pi}{b \sin \Omega} - \frac{2m\pi}{a} \cot \Omega + k_y^{\text{inc}}. \tag{2.17}$$

Note that $\alpha_{mn} = \alpha_m$ and $\beta_{mn} = \beta_n$ when $\Omega = 90°$.

For an aperture-type (inductive) FSS as depicted in Figure 2.1(b) [3, 8, 9], we can apply the concepts of duality to Eq. (2.1) to relate the scattered magnetic field and the magnetic surface current. Enforcing the continuity of the total magnetic field on either side of the aperture, one obtains the following equation:

$$-\begin{bmatrix} H_x^{\text{inc}}(x, y) \\ H_y^{\text{inc}}(x, y) \end{bmatrix} = \frac{4\pi}{j\omega\mu_0 ab} \sum_{m=-\infty}^{\infty} \sum_{n=-\infty}^{\infty} \begin{bmatrix} k_0^2 - \alpha_{mn}^2 & -\alpha_{mn}\beta_{mn} \\ -\alpha_{mn}\beta_{mn} & k_0^2 - \beta_{mn}^2 \end{bmatrix} \tilde{\mathbf{G}}(\alpha_{mn}, \beta_{mn}) \cdot \begin{bmatrix} \tilde{M}_x(\alpha_{mn}, \beta_{mn}) \\ \tilde{M}_y(\alpha_{mn}, \beta_{mn}) \end{bmatrix} e^{j\alpha_{mn}x} e^{j\beta_{mn}y}. \tag{2.18}$$

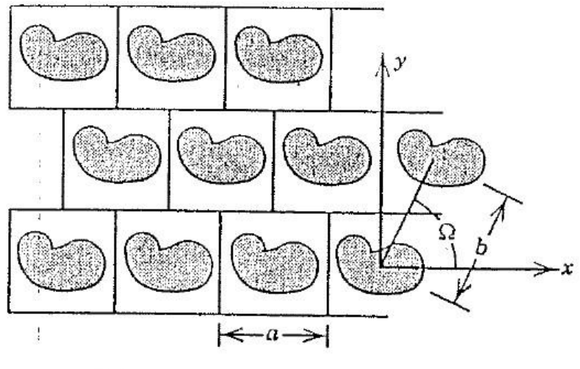

FIGURE 2.3 A skewed-grid FSS.

Here M is the equivalent magnetic surface current at the aperture. A detailed formulation of Eq. (2.18) will be presented later. The solution of Eq. (2.18) yields the unknown magnetic surface current distribution in the aperture of an inductive FSS. Equation (2.18), however, is valid only for a perfectly conducting FSS. If the screen has a finite conductivity, we must formulate the problem in terms of the surface currents on the conducting portions of the screen rather than the equivalent magnetic currents in the aperture, because the aperture is short-circuited by a perfect electric conducting plane in the process of formulating the integral equation.

2.2 SOLUTION OF THE OPERATOR EQUATION

Equations (2.15) and (2.18), governing the characteristics of the patch and aperture FSSs, can be solved with the method of moments. Specifically, we present the spectral Galerkin method because the equations are already formulated conveniently in the spectral domain.

As a first step, we rewrite Eqs. (2.15) and (2.18) in the symbolic form

$$\mathbf{Lu} = \mathbf{g} = \left(\hat{x}\hat{x}L_{xx} + \hat{x}\hat{y}L_{xy} + \hat{y}\hat{x}L_{yx} + \hat{y}\hat{y}L_{yy}\right) \cdot \left(\hat{x}u_x + \hat{y}u_y\right) = \left(\hat{x}g_x + \hat{y}g_y\right), \tag{2.19}$$

where $\mathbf{u}$ represents either the unknown induced current $\mathbf{J}$ or $\mathbf{M}$, $\mathbf{g}$ corresponds to the known incident $\mathbf{E}^{\text{inc}}$ and $\mathbf{H}^{\text{inc}}$ field, and $\mathbf{L}$ is the operator relating the unknown $\mathbf{u}$ to the incident field $\mathbf{g}$. The method of moments begins by expressing $\mathbf{u}$ in terms of a set of known basis functions $\mathbf{f}$

$$\mathbf{u} = \sum_{i=1}^{N} C_i \mathbf{f}_i = \sum_{i=1}^{N} \left(\hat{x}C_{xi}f_{xi} + \hat{y}C_{yi}f_{yi}\right), \tag{2.20}$$

where the C's are unknown coefficients to be determined. To convert the operator equation (2.19) to a matrix equation, we substitute Eq. (2.20) into (2.19). In the method of moments, the operator equation is modified by forming a scalar product between it and a "test function." In Galerkin's method [37, 49], the test function is chosen to be the same function as the basis function. Consequently, Eq. (2.19) is now converted to a matrix equation

$$\begin{bmatrix} \left\langle f_{xi}, L_{xx} \sum_{j=1}^{N} f_{xj} \right\rangle & \left\langle f_{xi}, L_{xy} \sum_{j=1}^{N} f_{yj} \right\rangle \\ \left\langle f_{yi}, L_{yx} \sum_{j=1}^{N} f_{xj} \right\rangle & \left\langle f_{yi}, L_{yy} \sum_{j=1}^{N} f_{yj} \right\rangle \end{bmatrix} \begin{bmatrix} C_{xj} \\ C_{yj} \end{bmatrix} = \begin{bmatrix} \langle f_{xi}, g_x \rangle \\ \langle f_{yi}, g_y \rangle \end{bmatrix}, \tag{2.21}$$

where the scalar product $\langle a, b \rangle$ is defined as

$$\langle a, b \rangle = \int_{\text{unit cell}} a^* b \, ds, \tag{2.22}$$

a^* is the complex conjugate of a, and the integration is over the area of the unit cell as depicted in Figure 2.1.

The efficiency with which the solution for Eq. (2.21) can be derived for a desired accuracy depends on the choice of basis functions, which are often governed by the geometry of the patch or aperture in the unit cell. Matrix fill time, matrix size, and solution technique of the matrix equation all depend on basis functions, it is important to consider several factors that dictate their choice. First, in order that the number of basis functions used to represent the unknown current be minimal, and therefore the matrix size be small, it is desirable that these functions satisfy the appropriate edge condition [52]. For example, the current component parallel to a conducting edge must be singular. In contrast, the component normal to the edge must vanish. The enforcement of the rate of singularity or the rate of vanishing when approaching the edge, however, is not strictly required [53, 54]. Second, it is convenient to choose basis functions that are analytically Fourier transformable so that numerical evaluation of their transform is not required. It is also desirable that numerical values of these transformed functions be easily computed. Third, in order that the scalar products appearing in the matrix elements be calculated without an inordinately large investment in computer time, the transforms of the basis functions must decay reasonably rapidly for large α and β. Finally, if the number of basis functions needed to accurately represent the unknown current density becomes so large that the matrix solve time dominates the matrix solution, then an iterative scheme (e.g., conjugate gradient method) may be more computationally efficient than direct simultaneous solution (e.g., Gaussian elimination) of the set of equations represented by Eq. (2.21). The iterative procedure is preferable, especially for a multilayered FSS screen in which the number of unknowns is usually too large for the core memory of the computer.

In general, there are two categories of basis functions used to represent the unknown surface currents in the moment method, namely, entire-domain and subdomain basis functions. First, consider entire-domain functions. These functions span the entire support of the unknown, the patch or the aperture in an FSS cell, and are typically tailored for the specific geometry of the region over which the unknown is being expanded. Examples of such element geometries are dipole, square patch, circular patch, cross, and Jerusalem cross, for which entire-domain functions have been successfully applied [5, 7, 12, 25, 29, 37]. Circular rings and square loops have also been studied extensively [28, 30–32, 35]. These element geometries are illustrated in Figure 2.4 [2].

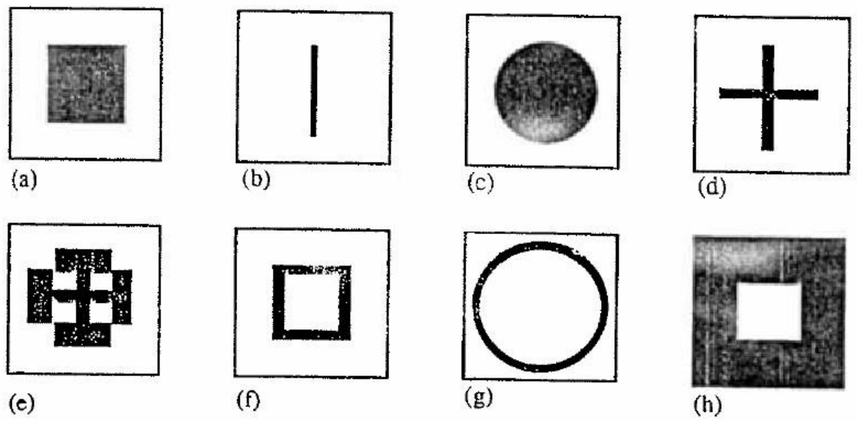

FIGURE 2.4 Some typical FSS unit-cell geometries: (a) square patch; (b) dipole; (c) circular patch; (d) cross dipole; (e) Jerusalem cross; (f) square loop; (g) circular loop; (h) square aperture.

The most important advantage of using the entire-domain type of basis functions is that the size of the resulting moment method matrix is usually much smaller than that for the subdomain functions; thus, entire-domain basis functions chosen according to the considerations listed earlier provide an efficient solution for the spectral response of the FSS screen. However, for arbitrary unit-cell geometries, suitable entire-domain basis functions are not, in general, available. Furthermore, when the finite conductivity of the conducting surface is not uniform, the entire-domain basis functions that proved useful for the perfectly conducting FSS are no longer suitable. A bismuth-loaded aluminum I-pole array [55] is an FSS with nonuniform conductivity loading. Thus, for treating FSS screens comprising arbitrarily shaped unit-cell geometry and for aperture screens with finite conductivities, subdomain basis functions have been found to be more suitable than entire-domain functions [36, 41, 42, 46, 56].

We now discuss two approaches for solving the operator equation for the induced current on the screen. We employ the direct matrix inversion approach via Gaussian elimination when the entire-domain basis functions are available. In contrast, when subdomain basis functions are used, we solve the matrix equation by the conjugate gradient method. Note that the two matrix solution techniques and the two types of basis functions are interchangeable, although the chosen combination may not have optimal efficiency.

Let us first consider the entire-domain basis functions. Using Galerkin's method with a suitable set of basis functions, we obtain the following matrix equation for Eq. (2.15) with all the multiplication constants absorbed into the

matrix element $\tilde{G}$:

$$\begin{bmatrix} \int J_{xi}^{*} E_x^{\text{inc}}\, ds \\ \int J_{yi}^{*} E_y^{\text{inc}}\, ds \end{bmatrix} = \sum_{j=1}^{N} \sum_{m=-\infty}^{\infty} \sum_{n=-\infty}^{\infty} \begin{bmatrix} \tilde{J}_{xi}^{*} & 0 \\ 0 & \tilde{J}_{yi}^{*} \end{bmatrix} \begin{bmatrix} \tilde{G}_{xx} & \tilde{G}_{xy} \\ \tilde{G}_{yx} & \tilde{G}_{yy} \end{bmatrix} \times \begin{bmatrix} \tilde{J}_{xj}(\alpha_{mn}, \beta_{mn}) & 0 \\ 0 & \tilde{J}_{yj}(\alpha_{mn}, \beta_{mn}) \end{bmatrix} \begin{bmatrix} C_{xj} \\ C_{yj} \end{bmatrix}. \quad (2.23)$$

The asymptotic behavior of the transforms of the basis and test functions determines the number of terms needed in the doubly infinite summations, which determines the numerical efficiency of the solution. For some geometries (e.g., a rectangular patch), the number of terms in the double summation is easily related to the total number of specific entire-domain basis functions (sine and cosine functions) used. The minimum number of terms needed to obtain accurate weighting coefficient C's in Eq. (2.23) is governed by the "relative convergence" criterion [57–60]. Note that if spectral Green's functions taking into account dielectric support and different kinds of basis functions are employed, relative convergence may not exist [61]. For other geometries, this criterion is not as easily found. In general, one should gradually increase the number of summations until the matrix elements converge. The integrals on the left-hand side of Eq. (2.23) can be identified as the complex conjugate of the Fourier transforms of the test functions evaluated at $\alpha = \alpha_{00} = k_x^{\text{inc}}$ and $\beta = \beta_{00} = k_y^{\text{inc}}$.

The choices of entire-domain basis functions for some typical FSS geometries are listed in Mittra et al. [2] and are given here:

(1) Rectangular aperture or patch

$$J_{x\,pq}(x, y) \text{ or } M_{x\,pq}(x, y) = \hat{x} \sin\left[\frac{q\pi}{c}\left(x + \frac{c}{2}\right)\right] \frac{T_p(2y/d)}{\left[1 - (2y/d)^2\right]^{1/2}}, \quad (2.24)$$

$$J_{y\,rs}(x, y) \text{ or } M_{y\,rs}(x, y) = \hat{y} \frac{T_s(2x/c)}{\left[1 - (2x/c)^2\right]^{1/2}} \sin\left[\frac{r\pi}{d}\left(y + \frac{d}{2}\right)\right], \quad (2.25)$$

where $p, s = 0, 1, \ldots$, $q, r = 1, 2, \ldots$, and T_i is the ith-order Chebyshev function of the first kind. The lengths of the edges of the patch or aperture in the x and y directions are c and d, respectively.

(2) Circular aperture or patch

$$J_{p\,rs}(\rho, \phi) \text{ or } M_{p\,rs}(\rho, \phi) = \hat{\rho}\left[1 - \left(\frac{2}{d}\rho\right)^2\right]^{1/2} U_r\left(\frac{2}{d}\rho\right) e^{js\phi} \quad (2.26)$$

and

$$J_{\phi\,pq}(\rho, \phi) \text{ or } M_{\phi\,pq}(\rho, \phi) = \hat{\phi} \frac{T_p(2\rho/d)}{\left[1 - (2\rho/d)^2\right]^{1/2}} e^{jq\phi}, \quad (2.27)$$

where $p = 0, 1, 2, \ldots$, $r = 1, 2, 3, \ldots$, $q, s = 0, \pm 1, \pm 2, \ldots$, and U_r is the rth-order Chebyshev function of the second kind. The radius of the circular patch or aperture is d.

(3) Thin dipole or slot

$$J_{yp} \text{ or } M_{yp} = \hat{y} \sin\left[\frac{p\pi}{L}\left(y + \frac{L}{2}\right)\right] P_x(0, W) P_y(0, L), \quad (2.28)$$

$$J_x \text{ or } M_x = 0, \quad (2.29)$$

where $p = 1, 2, \ldots$, $q = 0, 1, 2, \ldots$, W and L are the width and length of the dipole or slot, respectively, and

$$P_x(x_0, D) = \begin{cases} 1, & |x - x_0| \le \dfrac{D}{2}, \\ 0, & \text{otherwise}, \end{cases}$$

and

$$P_y(y_0, D) = \begin{cases} 1, & |y - y_0| \le \dfrac{D}{2}, \\ 0, & \text{otherwise}. \end{cases}$$

(4) Cross-dipole or slot

$$J_{xp} \text{ or } M_{xp} = \hat{x}\left\{C_{1p} \sin\left[\frac{p\pi}{L}\left(x + \frac{L}{2}\right)\right] + \operatorname{sgn}(x) B \cos\left(\frac{\pi}{L}x\right)\right\} \cdot P_x(0, L) P_y(0, W), \quad (2.30)$$

$$J_{yp} \text{ or } M_{yp} = \hat{y}\left\{C_{2p} \sin\left[\frac{p\pi}{L}\left(y + \frac{L}{2}\right)\right] - \operatorname{sgn}(y) B \cos\left(\frac{\pi}{L}y\right)\right\} \cdot P_x(0, w) P_y(0, L), \quad (2.31)$$

$$\operatorname{sgn}(x) = \begin{cases} 1, & \text{when } x \ge 0, \\ -1, & \text{otherwise}, \end{cases}$$

and $p = 1, 2, \ldots$. In writing Eqs. (2.30) and (2.31) with C_{1p} and C_{2p} unknown constants; we require the weighting coefficients of the x and y components to be equal.

(5) Jerusalem cross

x-directed current J_x or M_x

$$\hat{x}\sin\left[\frac{p\pi}{L}\left(x+\frac{L}{2}\right)\right]P_x(0,L)\,P_y(0,W), \tag{2.32}$$

$$\hat{x}\sin\left[\frac{p\pi}{D}\left(x+\frac{D}{2}\right)\right]P_x(0,D)\,P_y\left(\frac{\pm(L-W)}{2},W\right), \tag{2.33}$$

where $p = 1, 2, \ldots$.

y-directed current J_y or M_y

$$\hat{y}\sin\left[\frac{p\pi}{L}\left(y+\frac{L}{2}\right)\right]P_y(0,L)\,P_x(0,W), \tag{2.34}$$

$$\hat{y}\sin\left[\frac{p\pi}{D}\left(y+\frac{D}{2}\right)\right]P_y(0,D)\,P_x\left(\frac{\pm(L-W)}{2},W\right). \tag{2.35}$$

junction basis functions

$$\begin{aligned}&\hat{x}\,\mathrm{sgn}(x)\sin\frac{\pi x}{L}P_x(0,L)\,P_y(0,W)\\&\quad+\frac{1}{2}\hat{y}\,\mathrm{sgn}(y)\cos\frac{\pi y}{D}P_x\left(\frac{L-W}{2},W\right)P_y(0,D)\\&\quad-\frac{1}{2}\hat{y}\,\mathrm{sgn}(y)\cos\frac{\pi y}{D}P_x\left(\frac{-L+W}{2},W\right)P_y(0,D),\end{aligned} \tag{2.36}$$

$$\begin{aligned}&\hat{y}\,\mathrm{sgn}(y)\sin\frac{\pi y}{L}P_y(0,L)\,P_x(0,W)\\&\quad+\frac{1}{2}\hat{x}\,\mathrm{sgn}(x)\cos\frac{\pi x}{D}P_y\left(\frac{L-W}{2},W\right)P_x(0,D)\\&\quad-\frac{1}{2}\hat{x}\,\mathrm{sgn}(x)\cos\frac{\pi x}{D}P_y\left(\frac{-L+W}{2},W\right)P_x(0,D),\end{aligned} \tag{2.37}$$

$$\begin{aligned}&\hat{x}\sin\frac{\pi x}{L}P_x(0,L)\,P_y(0,W)+\frac{1}{2}\hat{y}\,\mathrm{sgn}(y)\cos\frac{\pi y}{D}P_x\left(\frac{L-W}{2},W\right)P_y(0,D)\\&\quad+\frac{1}{2}\hat{y}\,\mathrm{sgn}(y)\cos\frac{\pi y}{D}P_x\left(\frac{-L+W}{2},W\right)P_y(0,D),\end{aligned} \tag{2.38}$$

$$\begin{aligned}&\hat{y}\sin\frac{\pi y}{L}P_y(0,L)\,P_x(0,W)+\frac{1}{2}\hat{x}\,\mathrm{sgn}(x)\cos\frac{\pi x}{D}P_y\left(\frac{L-W}{2},W\right)P_x(0,D)\\&\quad+\frac{1}{2}\hat{x}\,\mathrm{sgn}(x)\cos\frac{\pi x}{D}P_y\left(\frac{-L+W}{2},W\right)P_x(0,D),\end{aligned} \tag{2.39}$$

$$\hat{x}\,\mathrm{sgn}(x)\cos\frac{\pi x}{L}P_x(0,L)\,P_y(0,D)-\hat{y}\,\mathrm{sgn}(y)\cos\frac{\pi y}{L}P_x(0,W)\,P_y(0,L). \tag{2.40}$$

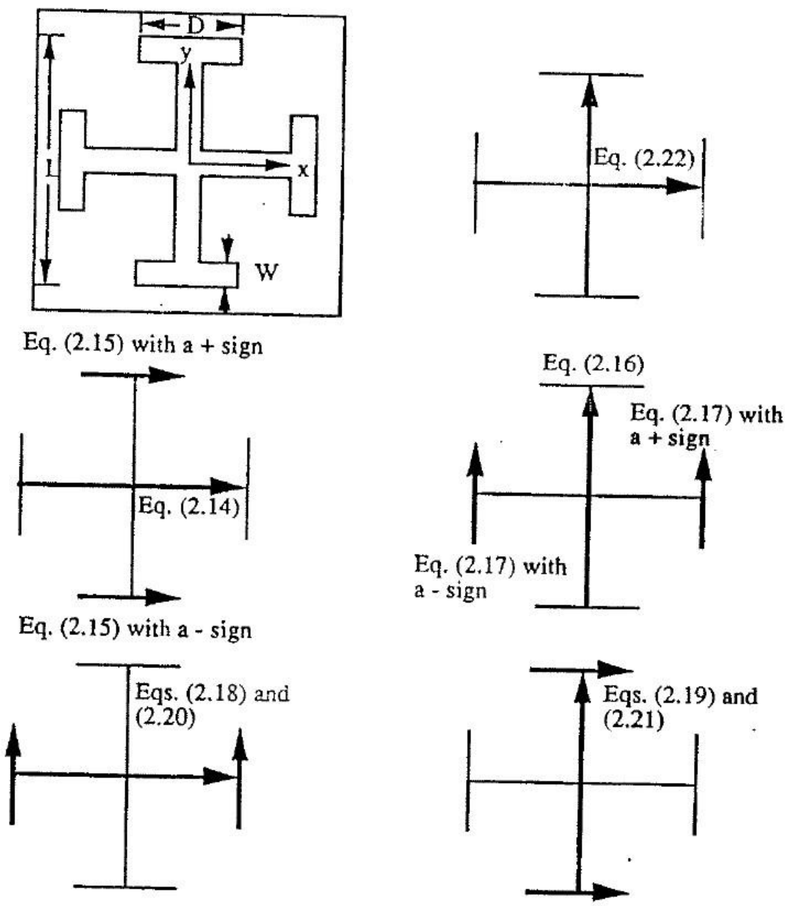

FIGURE 2.5 Basis functions for currents on a Jerusalem cross.

The parameters L, D, and W are defined in Figure 2.5 along with the location of each basis function.

Note that the edge conditions of currents normal and parallel to a conducting edge are enforced, but the rate of singularity and the rate of vanishing are not imposed for all the basis functions. The phase change of the current across the unit cell is provided by the linear combinations of the basis functions multiplied by their respective complex weighting coefficients. This phase variation can also be obtained by modifying the basis functions with a multiplication factor $e^{j(k_x^{inc}x+k_y^{inc}y)}$. This factor does not complicate the numerical evaluation since it only causes a phase shift to the Fourier transform of the basis functions. As illustrated in the numerical example discussed later, the solution converges more rapidly with the number of basis functions when this phase factor is included.

As mentioned, the basis functions are required to be analytically Fourier transformable. For example, the Fourier transforms of the basis functions in

Eqs. (2.24) and (2.25) are

$$\tilde{J}_{x\,pq} = c'\left\{\operatorname{sinc}\left(\frac{p\pi}{2} + \frac{c}{2}\alpha\right) + (-1)^{p-1}\operatorname{sinc}\left(\frac{p\pi}{2} - \frac{c}{2}\alpha\right)\right\}J_q\left(\frac{d}{2}\beta\right), \quad (2.41)$$

$$\tilde{J}_{y\,rs} = c''J_r\left(\frac{c}{2}\alpha\right)\left\{\operatorname{sinc}\left(\frac{s\pi}{2} + \frac{d}{2}\beta\right) + (-1)^{s-1}\operatorname{sinc}\left(\frac{s}{2} - \frac{d}{2}\beta\right)\right\}. \quad (2.42)$$

The multiplication constants c' and c'' can be absorbed into the weighting coefficients and, therefore, will not be required in the evaluation of current and reflection and transmission coefficients. Here J_q and J_s are qth- and sth-order Bessel functions, respectively.

When the conducting screen has a finite conductivity, Eq. (2.23) has to be modified to satisfy the impedance boundary condition [62]. The modified equation is

$$\begin{bmatrix} \int J_{xi}^* E_x^{\text{inc}}\, ds \\ \int J_{yi}^* E_y^{\text{inc}}\, ds \end{bmatrix} = \sum_j \sum_m \sum_n \begin{bmatrix} \tilde{J}_{xi}^* & 0 \\ 0 & \tilde{J}_{yi}^* \end{bmatrix}\begin{bmatrix} \tilde{G}_{xx} & \tilde{G}_{xy} \\ \tilde{G}_{yx} & \tilde{G}_{yy} \end{bmatrix}$$
$$\times \begin{bmatrix} \tilde{J}_{xj}(\alpha_{mn}, \beta_{mn}) & 0 \\ 0 & \tilde{J}_{yj}(\alpha_{mn}, \beta_{mn}) \end{bmatrix}\begin{bmatrix} C_{xj} \\ C_{yj} \end{bmatrix}$$
$$- Z_s \begin{bmatrix} \int J_{xi}^* J_{xj}\, ds \\ \int J_{yi}^* J_{yj}\, ds \end{bmatrix}, \qquad i = 1, 2, \ldots . \quad (2.43)$$

where Z_s is the surface impedance. Note that the integrals on the right-hand side have to be evaluated numerically.

Typically, the matrix size associated with Eq. (2.23) is about 20×20 (or less) when entire-domain basis functions are employed. In contrast, the number of subdomain basis functions required to represent the current accurately is often larger by an order of magnitude. Moreover, the Fourier transforms of the subdomain basis functions do not decay very rapidly until m and n are quite large in α_{mn} and β_{mn}; hence, more Floquet harmonic terms are needed for the double summation to converge. However, as we described, it is possible to accelerate the summation by using the fast Fourier transform (FFT) algorithm when the unit cell is discretized uniformly. If one finds that the matrix size in Eq. (2.23) becomes prohibitively large for subdomain functions and it becomes impractical to use conventional elimination schemes to solve the matrix equation, one may be forced to resort to iterative techniques instead.

One of the most frequently used subdomain basis functions is the rooftop [63], which has a triangular or piecewise-linear dependence in the direction of the current and a pulse or stepwise-constant dependence in the orthogonal direction, as shown in Fig. 2.6. It is expedient to discretize the unit cell into an $N \times N$ grid and to employ equal-size rooftop basis functions. Such a discretization scheme efficiently allows the use of the FFT to carry out the double summation appearing in the operator equation [64]. Note that the skew angle must be 90° to use FFT. Details of this summing procedure will be given shortly.

Let us direct our attention to the more general problem of solving for the current density distribution, which appears as the unknown in Eq. (2.43). The representations for J_x and J_y take the form

$$J_x = \sum_{-N/2}^{N/2-1} \sum_{-N/2}^{N/2-1} I_x(m, n) B_x(m, n), \quad (2.44)$$

$$J_y = \sum_{-N/2}^{N/2-1} \sum_{-N/2}^{N/2-1} I_y(m, n) B_y(m, n), \quad (2.45)$$

where B_x and B_y are the subdomain basis functions and I_x and I_y are the unknown amplitudes of the current elements corresponding to the subsections that reside within the conducting or resistive surface. It is evident that the element weights for the subdomains that fall outside the patches are to be set identically equal to zero.

The current basis functions are described by the following equations:

$$B_x(m, n) = \Lambda_x(m + 1/2)\Pi_x(n), \quad (2.46)$$

$$B_y(m, n) = \Lambda_y(m)\Pi_y(n + 1/2), \quad (2.47)$$

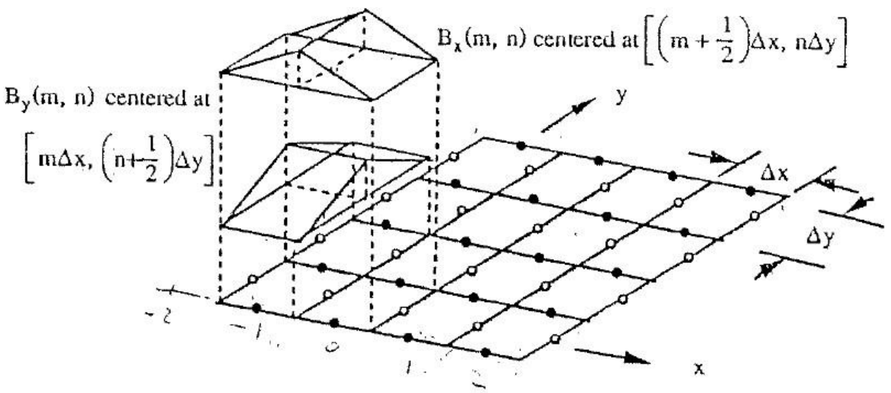

FIGURE 2.6 Rooftop basis functions.

where for the rooftop discretization one has

$$\Pi_x(n) = \begin{cases} 1, & |y - n\,\Delta y| < \dfrac{\Delta y}{2}, \\ 0, & \text{elsewhere}, \end{cases} \tag{2.48}$$

$$\Lambda_x(m) = \begin{cases} 1 - \dfrac{|x - m\,\Delta x|}{\Delta x}, & |x - m\,\Delta x| < \Delta x, \\ 0, & \text{elsewhere}, \end{cases} \tag{2.49}$$

where $\Delta x = a/N$ and $\Delta y = b/N$. Expressions similar to Eqs. (2.48) and (2.49) can be defined for Π_y and Λ_y. Note that the centers of $B_x(m, n)$ and $B_y(m, n)$ are offset by $(\Delta x/2, -\Delta y/2)$. For details of the discretization procedure, refer to Chan and Mittra [56] and Glisson and Wilton [63].

Denoting the test and basis functions in Eq. (2.43) as T and B, we write the resulting operator equation as

$$-\begin{bmatrix} E_{x0}\tilde{T}_x^*(0,0)\,P^*\left(p + \frac{1}{2}, q\right) \\ E_{y0}\tilde{T}_y^*(0,0)\,P^*\left(p, q + \frac{1}{2}\right) \end{bmatrix}$$

$$= \sum_{p'=-N/2}^{N/2-1} \sum_{q'=-N/2}^{N/2-1} \sum_{m=-N/2}^{N/2-1} \sum_{n=-N/2}^{N/2-1} \begin{bmatrix} \tilde{G}'_{xx}(m,n) & \tilde{G}'_{xy}(m,n) \\ \tilde{G}'_{yx}(m,n) & \tilde{G}'_{yy}(m,n) \end{bmatrix}$$

$$\cdot e^{j2\pi m\bar{p}/N} e^{j2\pi n\bar{q}/N} \begin{bmatrix} P^*(\bar{p},\bar{q})P^*\left(\bar{p} + \frac{1}{2}, \bar{q} - \frac{1}{2}\right) \\ P^*\left(\bar{p} - \frac{1}{2}, \bar{q} + \frac{1}{2}\right)P^*(\bar{p},\bar{q}) \end{bmatrix} \begin{bmatrix} I_x(p',q') \\ I_y(p',q') \end{bmatrix}$$

$$+ Z_s \begin{bmatrix} F_x(p,q) & 0 \\ 0 & F_y(p,q) \end{bmatrix} \begin{bmatrix} I_x(p,q) \\ I_y(p,q) \end{bmatrix}, \tag{2.50}$$

with $\bar{p} = p - p'$ and $\bar{q} = q - q'$. The term P is defined as

$$P(p,q) = e^{-j(k_x^{\text{inc}} p\,\Delta x + k_y^{\text{inc}} q\,\Delta y)}, \tag{2.51}$$

and E_{x0} and E_{y0} are the magnitudes of the x and y components of the incident field, respectively. The first two summations on the right-hand side of Eq. (2.50) correspond to summing the scattered field at a testing location due to each of the basis functions. The next two summations correspond to transforming the scattered field in the spectral domain into the spatial domain. The Fourier transform of $B_x(p', q')$ is equal to the same function centered at the origin multiplied by a phase shift $e^{-j(\alpha_m p'\,\Delta x + \beta_n q'\,\Delta y)}$. The inner product of the scattered field and the test function $T_x(p, q)$ corresponds to taking the complex conjugate of the Fourier transform of the test

function as in the first term on the right-hand side of Eq. (2.43). Once again this introduces a phase shift of $e^{j(\alpha_m p\,\Delta x + \beta_n q\,\Delta y)}$, and the net phase shift is therefore given by $e^{j(\alpha_m \bar{p}\,\Delta x + \beta_n \bar{q}\,\Delta y)}$. Recall from Eq. (2.16) that the next phase shift is then decomposed into two terms given by $e^{j2\pi mp/N} e^{j2\pi nq/N} P^*(\bar{p}, \bar{q})$. Other phase terms, $P^*(\bar{p} + \frac{1}{2}, \bar{q} - \frac{1}{2})$ and $P^*(\bar{p} - \frac{1}{2}, \bar{q} + \frac{1}{2})$, result from the offset of the centers of the x and y basis functions. After rearranging the order of summation, we write Eq. (2.50) as

$$-\begin{bmatrix} E_{x0}\tilde{T}_x^*(0,0)\,P^*\left(p + \frac{1}{2}, q\right) \\ E_{y0}\tilde{T}_y^*(0,0)\,P^*\left(p, q + \frac{1}{2}\right) \end{bmatrix}$$

$$= \sum_{m=-N/2}^{N/2-1} \sum_{n=-N/2}^{N/2-1} \begin{bmatrix} \tilde{G}'_{xx}(m,n) & \tilde{G}'_{xy}(m,n) \\ \tilde{G}'_{yx}(m,n) & \tilde{G}'_{yy}(m,n) \end{bmatrix}$$

$$\cdot \sum_{p'=-N/2}^{N/2-1} \sum_{q'=-N/2}^{N/2-1} \begin{bmatrix} e^{-j(\alpha_{p'} m\,\Delta x + \beta_{q'} n\,\Delta y)} & 0 \\ 0 & e^{-j(\alpha_{p'} m\,\Delta x + \beta_{q'} n\,\Delta y)} \end{bmatrix}$$

$$\times \begin{bmatrix} I_x(p',q') \\ I_y(p',q') \end{bmatrix} e^{j(\alpha_m p\,\Delta x + \beta_m q\,\Delta y)}$$

$$+ Z_s \begin{bmatrix} F_x(p,q) & 0 \\ 0 & F_y(p,q) \end{bmatrix} \begin{bmatrix} I_x(p,q) \\ I_y(p,q) \end{bmatrix}. \tag{2.52}$$

Equation (2.52) has been written such that the summation can be performed simultaneously by using the FFT algorithm. Symbolically, Eq. (2.52) reads

$$-\begin{bmatrix} E_{x0}\tilde{T}_x^*(0,0)\,P^*\left(p + \frac{1}{2}, q\right) \\ E_{y0}\tilde{T}_y^*(0,0)\,P^*\left(p, q + \frac{1}{2}\right) \end{bmatrix}$$

$$= \begin{bmatrix} P^*(p,q) & 0 \\ 0 & P^*(p,q) \end{bmatrix} \text{FFT}^{-1}$$

$$\cdot \left\{ \begin{bmatrix} \tilde{G}'_{xx}(m,n) & \tilde{G}'_{xy}(m,n) \\ \tilde{G}'_{yx}(m,n) & \tilde{G}'_{yy}(m,n) \end{bmatrix} \cdot \left\{ \text{FFT} \begin{bmatrix} P(p',q')0 \\ 0P(p',q') \end{bmatrix} \begin{bmatrix} I_x(p',q') \\ I_y(p',q') \end{bmatrix} \right\} \right\}$$

$$+ Z_s \begin{bmatrix} F_x(p,q) & 0 \\ 0 & F_y(p,q) \end{bmatrix} \begin{bmatrix} I_x(p,q) \\ I_y(p,q) \end{bmatrix}. \tag{2.53}$$

In Eqs. (2.50), (2.52), and (2.53), the modified spectral Green's functions are

$$\tilde{G}'_{xx}(m,n) = \frac{1}{N^2}\sum_{r=-\infty}^{\infty}\sum_{s=-\infty}^{\infty}\tilde{G}_{xx}(m',n')\tilde{B}_x(m',n')\tilde{T}_x^*(m',n'), \quad (2.54)$$

$$\tilde{G}'_{xy}(m,n) = \frac{1}{N^2}\sum_{r=-\infty}^{\infty}\sum_{s=-\infty}^{\infty}\tilde{G}_{xy}(m',n')\tilde{B}_y(m',n')\tilde{T}_x^*(m',n') \times e^{j(\alpha_{m'}\Delta x/2-\beta_{n'}\Delta y/2)}, \quad (2.55)$$

$$\tilde{G}'_{yx}(m,n) = \frac{1}{N^2}\sum_{r=-\infty}^{\infty}\sum_{s=-\infty}^{\infty}\tilde{G}_{yx}(m',n')\tilde{B}_x(m',n')\tilde{T}_y^*(m',n') \times e^{-j(\alpha_{m'}\Delta x/2-\beta_{n'}\Delta y/2)}, \quad (2.56)$$

$$\tilde{G}'_{yy}(m,n) = \frac{1}{N^2}\sum_{r=-\infty}^{\infty}\sum_{s=-\infty}^{\infty}\tilde{G}_{yy}(m',n')\tilde{B}_y(m',n')\tilde{T}_y^*(m',n'). \quad (2.57)$$

$\tilde{B}$ and $\tilde{T}$ are the Fourier transforms of the basis and test functions, respectively. The asterisk represents complex conjugate. When an $N \times N$ FFT is used, $n' = n + rN$ and $m' = m + sN$, $-N/2 \le n, m \le N/2 - 1$. The summations in r and s are typically done from -4 to 4. The resistance terms F in Eqs. (2.50), (2.52), and (2.53) will be defined shortly.

The unknown weighting coefficients can be obtained either by a direct solution of the matrix equation or by using an iterative procedure, such as the conjugate gradient method (CGM) [65, 66]. One distinct difference between the numerical implementation of the direct matrix method and the iterative procedure lies in the manner in which the double summation is evaluated in these two schemes. In the conventional direct matrix method [36], each matrix element is a double summation with the index ranging from $-N_N$ to N_N, and the computation of these double summations is usually time consuming. A more efficient way to evaluate the matrix elements is to first compute the double summations in Eqs. (2.54) to (2.57) and then carry out the double summations in Eq. (2.50) by the FFT. When the matrix size becomes prohibitively large, Eq. (2.53) is cast in a form suitable for applying the iterative procedure based on the CGM. For completeness, the CGM algorithm is listed in Table 2.1.

The rate of convergence of the iteration algorithm based on CGM depends on the condition number of the operator [67]—the higher the condition number, the slower the convergence. The condition number of a matrix is a measure of the determinant of the matrix in magnitude relative to the cofactors of elements of that matrix when the largest matrix element has been normalized to 1 [68]. The choice of the basis and test functions plays an important role in determining the condition number [56]. We consider two test functions, namely, the rooftop and the razor-blade functions, and compare the convergence of the iterative procedures for these two choices. The

TABLE 2.1. The Conjugate Gradient Algorithm

$Lu = g$
Initial guess: $u_0 = 0$
Initial residual: $R_0 = g$
Initial error: $\text{error}_0 = \langle R_0, R_0 \rangle$
$u_1 = L_A R$, L_A is the adjoint operator of L
$a = \langle u_1, u_1 \rangle$
$g_1 = Lu_1$
$b = \langle g_1, g_1 \rangle$
$\eta = a/b$
$U_1 = u_0 + \eta u_1$
1: **********$n = n + 1$**********
$a_1 = a$
$u'_n = L_A R_n$
$a = \langle u'_n, u'_n \rangle$
$u_n = u'_n + a/a_1 u_{n-1}$
$g_n = Lu_n$, $b = \langle g_n, g_n \rangle$, $\eta = a/b$
$R_n = R_{n-1} - \eta g_n$, $U_n = U_{n-1} + u_n$
$\text{error}_n = \langle R_n, R_n \rangle$
percentage error = $\text{sqrt}(\text{error}_n/\text{error}_0) \times 100\%$
if error ⟨prescribed value of n⟩ maximum value → stop
otherwise go to 1 to continue

x-directed razor-blade function is defined as follows:

$$T_x(m,n) = \begin{cases} 1, & |x - m\Delta x| \le \dfrac{\Delta x}{2} \quad \text{and} \quad y - n\Delta y = 0, \\ 0, & \text{elsewhere.} \end{cases} \quad (2.58)$$

This function has a support of Δx in the x direction and is a delta function in the y direction. A similar expression can be defined for the y-directed razor-blade function. The Fourier transforms of the two test functions are
Rooftop

$$\tilde{T}_x(m,n) = \left[\frac{\sin(\alpha_m \Delta x/2)}{\alpha_m \Delta x/2}\right]^2 \frac{\sin(\beta_n \Delta y/2)}{\beta_n \Delta y/2}, \quad (2.59)$$

$$\tilde{T}_y(m,n) = \frac{\sin(\alpha_m \Delta x/2)}{\alpha_m \Delta x/2}\left[\frac{\sin(\beta_n \Delta y/2)}{\beta_n \Delta y/2}\right]^2, \quad (2.60)$$

Razor blade

$$\tilde{T}_x(m,n) = \frac{\sin(\alpha_m \Delta x/2)}{\alpha_m \Delta x/2}, \tag{2.61}$$

$$\tilde{T}_y(m,n) = \frac{\sin(\beta_n \Delta y/2)}{\beta_n \Delta y/2}. \tag{2.62}$$

Substituting these basis and test functions in Eqs. (2.54) to (2.57), one can obtain the relationship between the scattered field and the unknown weighting coefficient, either in a matrix form as shown in Eq. (2.50) or in an operator form as in Eq. (2.53). Unlike the scattered field terms, the surface resistance terms, F, in Eqs. (2.50) and (2.53) consist of simple multiplication operations instead of convolutions. Each of these resistance terms F is the scalar product of the basis and test functions that can be carried out analytically. The resistance functions F_x and F_y in Eqs. (2.50) and (2.53) are

$$F_x(m,n) = C_1\delta(m-1,n) + C_2\delta(m,n) + C_1(m+1,n), \tag{2.63}$$

$$F_y(m,n) = D_1\delta(m,n-1) + D_2\delta(m,n) + D_1(m,n+1), \tag{2.64}$$

where the Kronecker δ function is defined as

$$\delta(m,n) = \begin{cases} 1 & \text{when } m = r \text{ and } n = s, \\ 0 & \text{elsewhere,} \end{cases} \tag{2.65}$$

and s and r are the indices of the current elements I_x and I_y in Eqs. (2.50) and (2.53). The C and D values will be defined shortly for the rooftop and razor-blade test functions. In addition, some modifications are necessary for the edge element for which $m = -N/2$ or $N/2 - 1$ and $n = -N/2$ or $N/2 - 1$. The δ functions in Eqs. (2.63) and (2.64) are to be modified as follows:

$$m = -\frac{N}{2}, \qquad \delta(m-1,n) \to e^{jk_x^{\text{inc}}a}\delta\left(\frac{N}{2}-1,n\right), \tag{2.66}$$

$$m = \frac{N}{2}-1, \qquad \delta(m+1,n) \to e^{-jk_x^{\text{inc}}a}\delta\left(-\frac{N}{2},n\right), \tag{2.67}$$

$$n = -\frac{N}{2}, \qquad \delta(m,n-1) \to e^{jk_y^{\text{inc}}b}\delta\left(m,\frac{N}{2}-1\right), \tag{2.68}$$

$$n = \frac{N}{2}-1, \qquad \delta(m,n+1) \to e^{-jk_y^{\text{inc}}b}\delta\left(m,-\frac{N}{2}\right). \tag{2.69}$$

For rooftop basis and razor-blade testing, one has

$$C_1 = D_1 = \frac{\Delta x\,\Delta y}{8}, \tag{2.70}$$

$$C_2 = D_2 = \frac{3\Delta x\,\Delta y}{4}. \tag{2.71}$$

On the other hand, for the same basis functions but rooftop testing, the C's and D's reduce to

$$C_1 = D_1 = \frac{\Delta x\,\Delta y}{6}, \tag{2.72}$$

$$C_2 = D_2 = \frac{2\Delta x\,\Delta y}{3}. \tag{2.73}$$

Next, we consider the problem of truncating the doubly infinite summations in Eqs. (2.54) through (2.57). When the truncation criterion is chosen such that r and s in Eqs. (2.54) to (2.57) are both zero, it is seen that only $N \times N$ Floquet harmonics are retained in the doubly infinite summation when an $N \times N$ FFT is employed. This approximation is used in Montgomery and Davey [41], Christodoulou and Kauffman [42], and Cwik and Mittra [46] and is valid only if the contributions of the remainder of the Floquet harmonics are negligible; however, in most cases, this assumption usually leads to a less accurate solution.

For the razor-blade test function, the asymptotic behavior of the summand in the infinite summation appears in Eqs. (2.54) to (2.57) and is

$$\frac{1}{mn(m^2+n^2)^{1/2}}. \tag{2.74}$$

Owing to the asymptotic behavior of the summand, the convergence of the summation is relatively slow. However, for the rooftop test function, the asymptotic behavior takes the form

$$\frac{1}{(mn)^2(m^2+n^2)^{1/2}}. \tag{2.75}$$

For this choice of test function, the series in Eqs. (2.54) to (2.57) converge considerably faster and the number of terms in each of the summations can be reduced by about a factor of 2. Choosing a test function with a superior asymptotic behavior not only improves the rate of convergence for the double summation but it also accelerates the convergence of the iteration algorithm as well.

Let us now consider the procedure for solving Eq. (2.53) by the CGM, outlined briefly in Table 2.1. As we see, it is necessary to construct an adjoint operator and define an inner product. For a matrix operator, its adjoint operator is the transpose of its complex conjugate. Consider the FFT as a matrix operator. The transpose of the complex conjugate of the FFT operation is simply the inverse FFT operation, and vice versa. In view of this, the adjoint operators for Eqs. (2.53) can be written as

$$\left\{\begin{bmatrix} P^* & 0 \\ 0 & P^* \end{bmatrix} \text{FFT}^{-1} \begin{bmatrix} \tilde{G}_{xx}^{t*} & \tilde{G}_{yx}^{t*} \\ \tilde{G}_{xy}^{t*} & \tilde{G}_{yy}^{t*} \end{bmatrix} \text{FFT} \begin{bmatrix} P & 0 \\ 0 & P \end{bmatrix} + Z_s^* \begin{bmatrix} F_x & 0 \\ 0 & F_y \end{bmatrix}\right\}. \quad (2.76)$$

Note that the complex conjugate transposition of the resistance matrix operations in Eqs. (2.52) and (2.53) involving F remains unchanged since the matrix is real and symmetric, as seen in Eq. (2.76).

The unknowns of operator equation (2.53) are the amplitudes of the basis functions; hence, the inner product can be defined as

$$\langle \mathbf{J}, \mathbf{J} \rangle = \sum_{-N/2}^{N/2-1} \sum_{-N/2}^{N/2-1} |I_x(m,n)|^2 + |I_y(m,n)|^2. \quad (2.77)$$

Once the operator and the adjoint operator have been identified for an equation to be solved and the inner product has been defined, one can follow the procedure in Table 2.1 to determine the unknown amplitudes of the subdomain basis functions in Eq. (2.64). However, if the number of unknowns is only moderate, one can employ a direct matrix method for matrix solution, usually with a considerable saving of time, because the FFT size remains unchanged regardless of the number of unknowns residing on the $N \times N$ grid.

2.3 FSS IN A MULTILAYERED MEDIUM

Of considerable practical interest are the extensions of the formulations presented for the patch- and aperture-type FSSs to screens (i) embedded in a dielectric medium of finite thickness, (ii) printed on a substrate, (iii) with a substrate and a superstrate, and to (iv) multiple screens for additional degrees of design freedom. We now show how these could be analyzed in a relatively straightforward manner. To modify the operator equation derived earlier for the induced current on the freestanding screen, we simply replace the spectral dyadic Green's function in Eq. (2.23) with a new Green's function that accounts for the substrate and the superstrate. The spectral dyadic Green's function for a layered dielectric medium can be conveniently obtained via the spectral-domain immitance approach, which has been described in Itoh [69] in connection with printed circuit transmission line problems.

The configuration of the multilayered FSS is depicted in Figure 2.7. The relative permittivities and permeabilities can be complex. The incident field will induce currents on the conducting surfaces, which, in turn, radiate scattered fields. For a multilayered FSS with M conducting screens, the scattered fields or the induced currents on each of the conducting surfaces are related to the incident fields by the equation

$$-\begin{bmatrix} E_{ix}^{\text{inc}} \\ E_{iy}^{\text{inc}} \end{bmatrix} = \sum_{j=1}^{M} \sum_{m=-\infty}^{\infty} \sum_{n=-\infty}^{\infty} \begin{bmatrix} \tilde{G}_{xx}^{ij} & \tilde{G}_{xy}^{ij} \\ \tilde{G}_{yx}^{ij} & \tilde{G}_{yy}^{ij} \end{bmatrix} \begin{bmatrix} \tilde{J}_{jx} \\ \tilde{J}_{jy} \end{bmatrix} e^{jk_{xm}x} e^{j\beta_n y}. \quad (2.78)$$

The subscript i corresponds to the ith conducting surface, where $i = 1, 2, \ldots, M$. The left-hand side of Eq. (2.78) corresponds to the sum of the scattered fields due to the current on each of the M surfaces. The unknown electric currents $\mathbf{J}_j$ in each screen are expanded in basis functions weighted with unknown coefficients. The unknown coefficients are then determined with Galerkin's method. To solve for these coefficients, we need the incident fields on the conducting surfaces and the spectral Green's functions.

Using the spectral-domain immittance approach [69], from Eq. (2.1) and

$$\mathbf{H}^s = \nabla \times \mathbf{A}, \quad (2.79)$$

we have

$$H_z^s = \frac{\partial}{\partial x} A_y - \frac{\partial}{\partial y} A_x, \quad (2.80)$$

$$E_z^s = \frac{1}{j\omega\epsilon} \frac{\partial}{\partial z} \left(\frac{\partial}{\partial x} A_x + \frac{\partial}{\partial y} A_y \right). \quad (2.81)$$

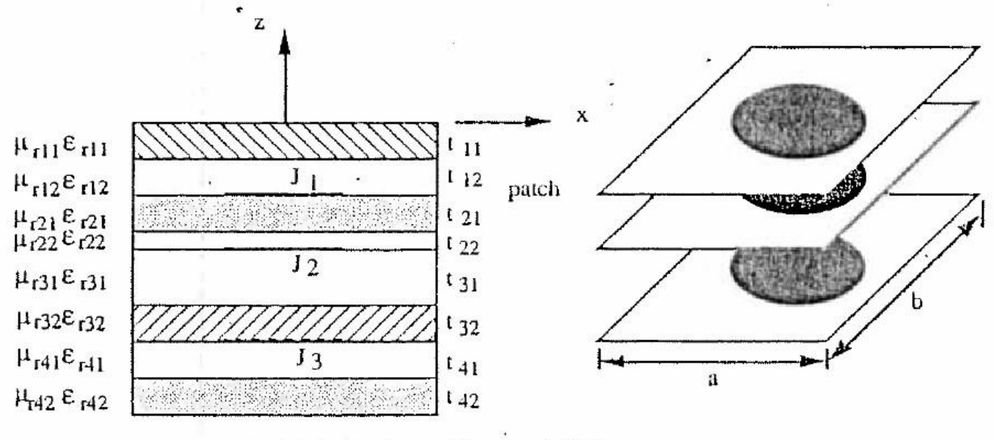

FIGURE 2.7 A multilayered FSS.

In the Fourier domain, these equations become

$$\tilde{H}_z^s \propto \frac{-\alpha}{\sqrt{\alpha^2+\beta^2}}\tilde{J}_y + \frac{\beta}{\sqrt{\alpha^2+\beta^2}}\tilde{J}_x, \tag{2.82}$$

$$\tilde{E}_z^s \propto \frac{\alpha}{\sqrt{\alpha^2+\beta^2}}\tilde{J}_x + \frac{\beta}{\sqrt{\alpha^2+\beta^2}}\tilde{J}_y, \tag{2.83}$$

with the subscripts in α and β omitted for convenience. A new coordinate system is defined in Figure 2.8 such that

$$\begin{bmatrix} u \\ v \end{bmatrix} = \begin{bmatrix} \sin\theta & -\cos\theta \\ \cos\theta & \sin\theta \end{bmatrix}\begin{bmatrix} x \\ y \end{bmatrix}, \tag{2.84}$$

where $\cos\theta = \alpha/\sqrt{\alpha^2+\beta^2}$ and $\sin\theta = \beta/\sqrt{\alpha^2+\beta^2}$. In the spectral domain, the induced current becomes

$$\tilde{\mathbf{J}} = \hat{x}\tilde{J}_x + \hat{y}\tilde{J}_y = \hat{u}\tilde{J}_u + \hat{v}\tilde{J}_v. \tag{2.85}$$

Hence, from Eq. (2.82), the v component of the spectral current yields

$$\tilde{H}_z^s \propto \frac{-\alpha}{\sqrt{\alpha^2+\beta^2}}\tilde{J}_v \sin\theta + \frac{\beta}{\sqrt{\alpha^2+\beta^2}}\tilde{J}_v \cos\theta = 0. \tag{2.86}$$

Similarly, from Eq. (2.83), the u component of the spectral current yields

$$\tilde{E}_z^s \propto \frac{\alpha}{\sqrt{\alpha^2+\beta^2}}\tilde{J}_u \sin\theta - \frac{\beta}{\sqrt{\alpha^2+\beta^2}}\tilde{J}_u \cos\theta = 0. \tag{2.87}$$

One can see that the u components of all the currents generate the TE (to z) fields and the v components generate the TM (to z) fields. After the TE and TM fields are decomposed in the spectral domain, we can use the transmission line model to relate the scattered field and the surface current for the u and v components separately.

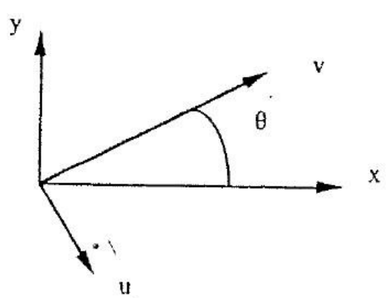

FIGURE 2.8 A new coordinate system.

Assume the scattered TE field at the ith conducting screen due to the current on the jth screen is

$$\begin{bmatrix} \tilde{E}_{iu}^s \\ \tilde{E}_{iv}^s \end{bmatrix} = \begin{bmatrix} \tilde{Z}^{\mathrm{TE}\,ij} & 0 \\ 0 & \tilde{Z}^{\mathrm{TM}\,ij} \end{bmatrix}\begin{bmatrix} \tilde{J}_{ju} \\ \tilde{J}_{jv} \end{bmatrix}. \tag{2.88}$$

With the two coordinate systems related by Eq. (2.84), Eq. (2.88) can be rewritten in x-y coordinates as

$$\begin{bmatrix} \tilde{E}_{ix}^s \\ \tilde{E}_{iy}^s \end{bmatrix} = \begin{bmatrix} \tilde{Z}^{\mathrm{TE}\,ij}\sin^2\theta + \tilde{Z}^{\mathrm{TM}\,ij}\cos^2\theta & \left(\tilde{Z}^{\mathrm{TM}\,ij} - \tilde{Z}^{\mathrm{TE}\,ij}\right)\cos\theta\sin\theta \\ \left(\tilde{Z}^{\mathrm{TM}\,ij} - \tilde{Z}^{\mathrm{TE}\,ij}\right)\cos\theta\sin\theta & \tilde{Z}^{\mathrm{TM}\,ij}\sin^2\theta + \tilde{Z}^{\mathrm{TE}\,ij}\cos^2\theta \end{bmatrix}\begin{bmatrix} \tilde{J}_{jx} \\ \tilde{J}_{jy} \end{bmatrix}$$

$$= \begin{bmatrix} \tilde{G}_{xx}^{ij} & \tilde{G}_{xy}^{ij} \\ \tilde{G}_{yx}^{ij} & \tilde{G}_{yy}^{ij} \end{bmatrix}\begin{bmatrix} \tilde{J}_{jx} \\ \tilde{J}_{jy} \end{bmatrix}. \tag{2.89}$$

Therefore, to derive the Green's function, one needs to derive Z in Eq. (2.89). Consider the situation depicted in Figure 2.9 and its transmission line equivalent model. The input admittance looking downward can be obtained through the successive use of the transmission line equation:

$$Y_{\mathrm{in}} = Y_0\frac{Y_0 + Y_L\coth\gamma_0 t}{Y_0\coth\gamma_0 t + Y_L}, \tag{2.90}$$

where Y_0 is the characteristic admittance of the medium. Similarly, the input admittance looking upward can also be obtained from Eq. (2.90). For Figure 2.9 the input admittance looking downward is

$$Y_{\mathrm{in}} = Y_{02}\frac{Y_{02} + Y_{L'}\coth\gamma_{02}t_2}{Y_{02}\coth\gamma_{02}t_2 + Y_{L'}},$$

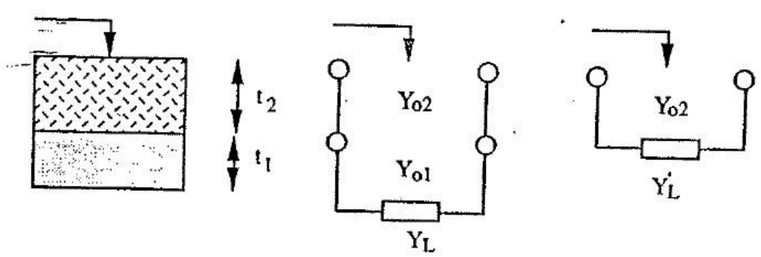

FIGURE 2.9 Equivalent transmission line mode.

where

$$Y_L = Y_{01}\frac{Y_{01} + Y_L \coth \gamma_{01} t_1}{Y_{01} \coth \gamma_{01} t_1 + Y_L}.$$

The TE and TM case characteristic admittance of a medium are defined as follows:

$$Y_0^{\text{TE}} = \frac{\gamma}{j\omega\mu} \quad \text{and} \quad Y_0^{\text{TM}} = \frac{j\omega\epsilon}{\gamma}, \tag{2.91}$$

where $\gamma = \sqrt{\alpha_m^2 + \beta_n^2 - \epsilon_r \mu_r k_0^2}$. The input impedance that relates the current on the jth screen and the scattered field on the jth screen due to this current is then

$$Z^{\text{TM,TE}\,ij} = \frac{1}{Y^{e,h}_{\text{bottom}} + Y^{e,h}_{\text{top}}}, \tag{2.92}$$

where Y_{bottom} and Y_{top} represent the input admittance looking downward and upward at the ith screen, respectively. The superscript e corresponds to the TM case, and the superscript h corresponds to the TE case. On the other hand, when the scattered field is evaluated at a distance t away from the current source as depicted in Figure 2.10, one needs to modify Eq. (2.92). In Figure 2.10, Y_L is the input admittance looking upward from the top surface; that is, it includes all layers above the ith screen. To transfer the impedance to a distance t, one needs to multiply Eq. (2.92) by the factor

$$Y_{\text{transfer}} = \frac{Y_0}{Y_0 \cos \gamma t + Y_L \sin \gamma t}. \tag{2.93}$$

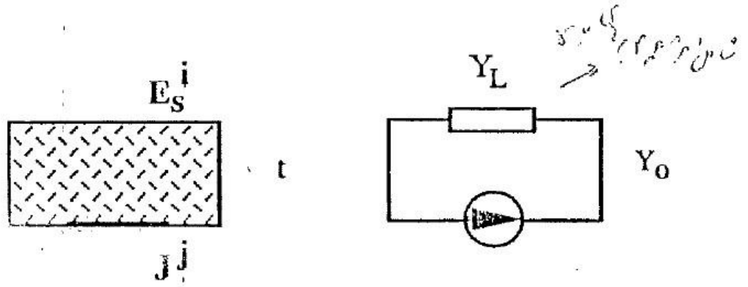

FIGURE 2.10 Relation between the current and the scattered field at different z locations.

Therefore,

$$Z^{\text{TM,TE}\,ij} = \frac{1}{Y^{e,h}_{\text{bottom}} + Y^{e,h}_{\text{top}}} Y^{e,h}_{\text{transfer}}. \tag{2.94}$$

If the scattered field is evaluated two layers from the source, one needs to multiply Eq. (2.94) by the factor in Eq. (2.93) with Y_L, Y_0, γ, and t replaced by the new ones. From this approach, we can derive the spectral Green's function relating the jth current and the ith scattered field. To complete the formulation, one also needs the incident field on the left-hand side of Eq. (2.78).

The incident fields for TE and TM polarizations can be derived by using the z-directed potential ψ. The incident field is calculated in the presence of the dielectric structures but with all conducting patches removed. A general configuration is depicted in Figure 2.11. The potential of each region is defined as follows:

$$\psi_0^{\text{TM,TE}} = e^{j\alpha_0 x} e^{j\beta_0 y} e^{\gamma_0 z} + R e^{j\alpha_0 x} e^{j\beta_0 y} e^{-\gamma_0 z}, \tag{2.95a}$$

$$\psi_1^{\text{TM,TE}} = e^{j\alpha_0 x} e^{j\beta_0 y} (C_{11} \cosh \gamma_1 z + C_{12} \sinh \gamma_1 z), \tag{2.95b}$$

$$\vdots$$

$$\psi_M^{\text{TM,TE}} = e^{j\alpha_0 x} e^{j\beta_0 y} (C_{M1} \cosh \gamma_M z + C_{M2} \sinh \gamma_M z), \tag{2.95c}$$

$$\psi_{M+1}^{\text{TM,TE}} = T e^{j\alpha_0 x} e^{j\beta_0 y} e^{\gamma_0 z}, \tag{2.95d}$$

where α_0 and β_0 are obtained by setting $m = n = 0$ in Eq. (2.17). When the FSS is backed by a ground plane, Eq. (2.95d) is not used because there is no

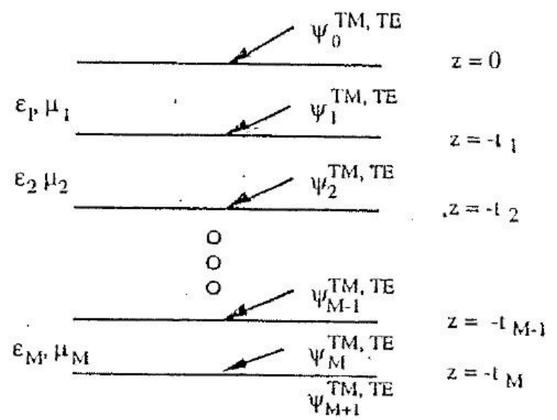

FIGURE 2.11 Incident fields.

transmitted field. Equation (2.95c) is modified such that it satisfies the boundary condition that the tangential electric field vanishes on the conductor. The modified equations are

$$\text{TE case} \qquad \psi_M^{\text{TE}} = e^{j\alpha_0 x} e^{j\beta_0 y}\left[C_{M2} \sinh \gamma_M (z + t_M)\right], \tag{2.96a}$$

$$\text{TM case} \qquad \psi_M^{\text{TM}} = e^{j\alpha_0 x} e^{j\beta_0 y}\left[C_{M2} \cosh \gamma_M (z + t_M)\right]. \tag{2.96b}$$

To enforce the continuity of the tangential electric and magnetic fields at the dielectric interfaces, we use the following equations [48]:

TE case

$$E_x = -\frac{\partial \psi^{\text{TE}}}{\partial y}; \qquad E_y = \frac{\partial \psi^{\text{TE}}}{\partial x}, \tag{2.97}$$

$$H_x = \frac{1}{j\omega\mu}\frac{\partial^2 \psi^{\text{TE}}}{\partial x\, \partial z}; \qquad H_y = \frac{1}{j\omega\mu}\frac{\partial^2 \psi^{\text{TE}}}{\partial y\, \partial z}, \tag{2.98}$$

TM case

$$E_x = \frac{1}{j\omega\epsilon}\frac{\partial^2 \psi^{\text{TM}}}{\partial x\, \partial z}; \qquad E_y = \frac{1}{j\omega\epsilon}\frac{\partial^2 \psi^{\text{TM}}}{\partial y\, \partial z}, \tag{2.99}$$

$$H_x = \frac{\partial \psi^{\text{TM}}}{\partial y}; \qquad H_y = -\frac{\partial \psi^{\text{TM}}}{\partial x}. \tag{2.100}$$

A matrix equation is obtained and solved numerically to determine the values of all the coefficients in Eqs. (2.95a) to (2.95d). The matrix equations corresponding to the TE and TM incidences are

$$[A][x] = [b], \tag{2.101}$$

$$[x] = [R \quad C_{11} \quad C_{12} \quad C_{21} \quad C_{22} \quad \cdots \quad C_{M1} \quad C_{M2} \quad T]^{\text{transpose}}, \tag{2.102}$$

$$[b] = [-1 \quad -\gamma_0 \quad 0 \quad 0 \quad 0 \quad \cdots \quad 0 \quad 0], \tag{2.103}$$

$$A_{11} = 1, \quad A_{12} = -1, \quad A_{21} = -\gamma_0, \quad A_{31} = -\frac{\gamma_1}{\epsilon_{r1}},$$

$$A_{2i+1,2i} = \cosh \gamma_i(-t_i), \quad A_{2i+1,2i+1} = \sinh \gamma_i(-t_i),$$

$$A_{2i+1,2i+2} = -\cosh \gamma_{i+1}(-t_i),$$

$$A_{2i+1,2i+3} = -\sinh \gamma_{i+1}(-t_i),$$

$$A_{2i+2,2i} = \frac{\gamma_i}{\xi_{ri}} \sinh \gamma_i(-t_i), \qquad A_{2i+1,2i+1} = \frac{\gamma_i}{\xi_{ri}} \cosh \gamma_i(-t_i),$$

$$A_{2i+1,2i+2} = -\frac{\gamma_{i+1}}{\xi_{ri+1}} \sinh \gamma_{i+1}(-t_i),$$

$$A_{2i+1,2i+3} = -\frac{\gamma_{i+1}}{\xi_{ri+1}} \cosh \gamma_{i+1}(-t_i), \qquad i = 1, 2, \ldots, M-1,$$

$$A_{2M+1,2M} = \cosh \gamma_M(-t_M), \quad A_{2M+1,2M+1} = \sinh \gamma_M(-t_M),$$

$$A_{2M+1,2M+2} = -e^{-\gamma_0 t_M},$$

$$A_{2M+2,2M} = \frac{\gamma_M}{\xi_{rM}} \sinh \gamma_M(-t_M),$$

$$A_{2M+1,2M+1} = \frac{\gamma_M}{\xi_{rM}} \cosh \gamma_M(-t_M),$$

$$A_{2M+2,2M+2} = -\gamma_0 e^{-\gamma_0 t_M}, \tag{2.104}$$

where $\xi_r = \mu_r$ and $\xi_r = \epsilon_r$ for TE and TM incidences, respectively. All other elements in $[A]$ are zero.

Using the expressions for the incident fields and that of the dyadic Green's function in the operator equation for the induced current density, one obtains the system of equations in Eq. (2.78) to be solved for a multilayered FSS with multilayered dielectrics. Note that the format of this equation is identical to that of the freestanding screen, although modifications are introduced by the expressions for the incident field and the composite Green's function.

2.4 REFLECTION AND TRANSMISSION COEFFICIENTS

Once the surface currents are known, the reflection and transmission coefficients of the FSSs can be calculated from the tangential scattered electric fields at $z = 0$ and $z = -t_M$, expressed in the spectral domain. These scattered fields are calculated on the conducting screen from Eq. (2.89) and then transferred to the top and bottom surfaces of the multilayered FSS by using Eq. (2.93) repeatedly. The total field on the top surface is the sum of the scattered field and the reflected field obtained by solving R in Eq. (2.101) and substituting its value in the second term on the right-hand side of Eq. (2.95a). Similarly, the total field on the bottom surface is the sum of the scattered field and the transmitted field obtained from Eq. (2.95d).

Consider a plane-wave incidence with its magnetic or electric vector potential given by

$$\mathbf{A} = \hat{z}e^{j\alpha_0 x}e^{j\beta_0 y}e^{\gamma_0 z}, \tag{2.105}$$

$$\mathbf{F} = \hat{z}e^{j\alpha_0 x}e^{j\beta_0 y}e^{\gamma_0 z}. \tag{2.106}$$

Here $A_z = \psi^{\mathrm{TM}}$ and $F_z = \psi^{\mathrm{TE}}$ as described in Section 3.

The total scattered field at $z = 0$ can be written as the superposition of Floquet's harmonics, which takes the form

$$\mathbf{E}^s = \mathbf{E}^r_{(0)}e^{j\alpha_0 x}e^{j\beta_0 y}e^{-\gamma_0 z} + \sum_{p=-\infty}^{\infty}\sum_{q=-\infty}^{\infty}\mathbf{E}^s_{pq}e^{j\alpha_p x}e^{j\beta_q y}e^{-\gamma_{pq} z} \tag{2.107}$$

where $\gamma_{pq} = \sqrt{\alpha_p^2 + \beta_q^2 - k_0^2}$.

An alternative form of $\mathbf{E}^s$ is

$$\mathbf{E}^s = -\nabla \times \mathbf{F}^s - j\omega\mu_0\mathbf{A}^s + \frac{1}{j\omega\epsilon_0}\nabla(\nabla \cdot \mathbf{A}^s), \tag{2.108}$$

where the scattered potentials are

$$\mathbf{A}^s = \hat{z}\sum_{p=-\infty}^{\infty}\sum_{q=-\infty}^{\infty}R^{\mathrm{TM}}_{pq}e^{j\alpha_p x}e^{j\beta_q y}e^{\gamma_{pq} z}, \qquad z = 0,$$

$$= \hat{z}\sum_{p=-\infty}^{\infty}\sum_{q=-\infty}^{\infty}R^{\mathrm{TM}}_{pq}\psi_{pq}, \tag{2.109}$$

$$\mathbf{F}^s = \hat{z}\sum_{p=-\infty}^{\infty}\sum_{q=-\infty}^{\infty}R^{\mathrm{TE}}_{pq}\psi_{pq}. \tag{2.110}$$

Hence,

$$E^s_x = \sum_{p=-\infty}^{\infty}\sum_{q=-\infty}^{\infty}\left(-j\beta_q R^{\mathrm{TE}}_{pq} - \frac{\alpha_p\gamma_{pq}}{\omega\epsilon_0}R^{\mathrm{TM}}_{pq}\right)\psi_{pq}, \tag{2.111}$$

$$E^s_y = \sum_{p=-\infty}^{\infty}\sum_{q=-\infty}^{\infty}\left(j\alpha_p R^{\mathrm{TE}}_{pq} - \frac{\beta_q\gamma_{pq}}{\omega\epsilon_0}R^{\mathrm{TM}}_{pq}\right)\psi_{pq}. \tag{2.112}$$

Multiplying Eqs. (2.111) and (2.112) by ψ^*_{mn} and integrating over the unit cell,

one gets

$$\int_{\text{unit cell}} E^s_x\psi^*_{mn}\,ds = \sum_{p=-\infty}^{\infty}\sum_{q=-\infty}^{\infty}\left(-j\beta_q R^{\mathrm{TE}}_{pq} - \frac{\alpha_p\gamma_{pq}}{\omega\epsilon_0}R^{\mathrm{TM}}_{pq}\right)\cdot\int_{\text{unit cell}}\psi_{pq}\psi^*_{mn}\,ds, \tag{2.113}$$

$$\int_{\text{unit cell}} E^s_y\psi^*_{mn}\,ds = \sum_{p=-\infty}^{\infty}\sum_{q=-\infty}^{\infty}\left(j\alpha_p R^{\mathrm{TE}}_{pq} - \frac{\beta_q\gamma_{pq}}{\omega\epsilon_0}R^{\mathrm{TM}}_{pq}\right)\cdot\int_{\text{unit cell}}\psi_{pq}\psi^*_{mn}\,ds. \tag{2.114}$$

Note that the left-hand sides of Eqs. (2.113) and (2.114) are the Fourier transform of E^s_x and E^s_y, respectively, evaluated at α_m and β_n. Due to the orthogonality property of Floquet's harmonics, R^{TE}_{mn} and R^{TM}_{mn} can be written from the previous equations as

$$R^{\mathrm{TE}}_{mn} = \frac{j\left(\beta_n\left(\tilde{E}^s_x(\alpha_m,\beta_n) + \tilde{E}^i_x\delta_{mn}\right) - \alpha_m\left(\tilde{E}^s_y(\alpha_m,\beta_n) + \tilde{E}^i_y\delta_{mn}\right)\right)}{\alpha_m^2 + \beta_n^2}, \tag{2.115}$$

$$R^{\mathrm{TM}}_{mn} = \frac{-\left(\alpha_m\left(\tilde{E}^s_x(\alpha_m,\beta_n) + \tilde{E}^i_x\delta_{mn}\right) + \beta_n\left(\tilde{E}^s_y(\alpha_m,\beta_n) + \tilde{E}^i_y\delta_{mn}\right)\right)}{\left(\alpha_m^2 + \beta_n^2\right)\gamma_{mn}/\omega\epsilon_0}.$$

$$\begin{pmatrix}\tilde{E}^s_x(\,,\,)\\ \tilde{E}^s_y(\,,\,)\end{pmatrix} = \frac{1}{j\omega\epsilon_0}\begin{pmatrix}k_0^2 - \alpha_m^2 & -\alpha_m\beta_n\\ -\alpha_m\beta_n & k_0^2 - \beta_n^2\end{pmatrix}\begin{pmatrix}\tilde{J}_x\\ \tilde{J}_y\end{pmatrix} \tag{2.116}$$

The reflected field terms are included when $m = n = 0$. The tilde in Eqs. (2.115) and (2.116) represents the Fourier transform of the quantity underneath. In a similar manner, the scattered field at the bottom surface can be evaluated. We have

$$T^{\mathrm{TE}}_{mn} = \frac{j\left(\beta_n\left(\tilde{E}^s_x(\alpha_m,\beta_n) + \tilde{E}^t_x\delta_{mn}\right) - \alpha_m\left(\tilde{E}^s_y(\alpha_m,\beta_n) + \tilde{E}^t_y\delta_{mn}\right)\right)}{\alpha_p^2 + \beta_q^2}, \tag{2.117}$$

$$T^{\mathrm{TM}}_{mn} = \frac{-\left(\alpha_m\left(\tilde{E}^s_x(\alpha_m,\beta_n) + \tilde{E}^t_x\delta_{mn}\right) + \beta_n\left(\tilde{E}^s_y(\alpha_m,\beta_n) + \tilde{E}^t_y\delta_{mn}\right)\right)}{\left(\alpha_m^2 + \beta_n^2\right)\gamma_{mn}/\omega\epsilon_0}. \tag{2.118}$$

In Eqs. (2.115) to (2.118), the reflected field and the transmitted field are

TE

$$\tilde{E}_x^r = -j\beta_0 R, \quad \tilde{E}_y^r = j\alpha_0 R, \quad \tilde{E}_x^t = -j\beta_0 T e^{-\gamma_0' t_M}, \quad \tilde{E}_y^t = j\alpha_0 T e^{-\gamma_0' t_M}, \tag{2.119}$$

TM

$$\tilde{E}_x^r = \frac{\alpha_0 \gamma_0}{\omega \epsilon_0} R, \quad \tilde{E}_y^r = \frac{\beta_0 \gamma_0}{\omega \epsilon_0} R, \quad \tilde{E}_x^t = \frac{\alpha_0 \gamma_0}{\omega \epsilon_0} T e^{-\gamma_0' t_M}, \quad \tilde{E}_y^t = \frac{\beta_0 \gamma_0}{\omega \epsilon_0} T e^{-\gamma_0' t_M}. \tag{2.120}$$

The power reflection and transmission coefficients of the propagating modes are obtained by taking the absolute value squared of the reflection and transmission coefficients. As a check, one can note that the sum of these power coefficients is equal to unity when normalized to the incident power if there are no conductor and dielectric losses.

2.5 MAGNETIC FIELD FORMULATION FOR AN APERTURE SCREEN

It was mentioned earlier that an aperture solution based on the use of magnetic surface currents provides an alternative means of FSS analysis [Eq. (2.18)]. This analysis requires that the screen be a perfect conductor, however. More generally, multilayered FSS analysis can be performed with some screens treated as patch FSSs and others treated as aperture FSSs. Here we use a patch-aperture-patch configuration as depicted in Figure 2.12 to illustrate how we can couple electric and magnetic currents in the FSS analysis [70]. To analyze this structure, it is more convenient to construct two auxiliary problems based on the equivalence principle [48], one for the fields above the aperture and one for the fields below. These two problems are coupled through the enforcement of boundary conditions.

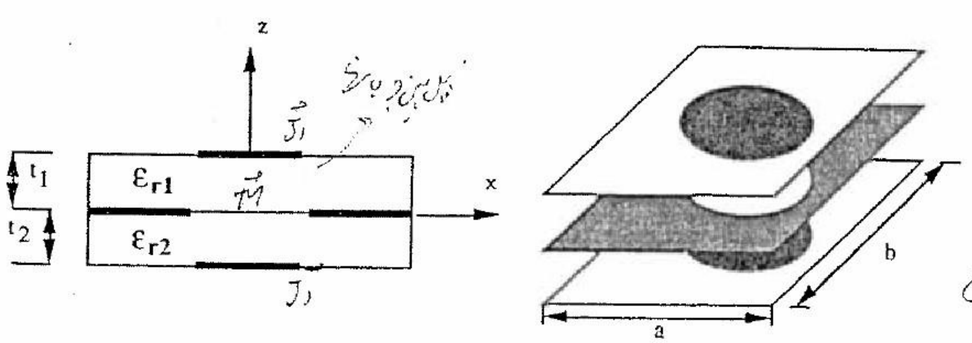

FIGURE 2.12 A patch-aperture-patch FSS.

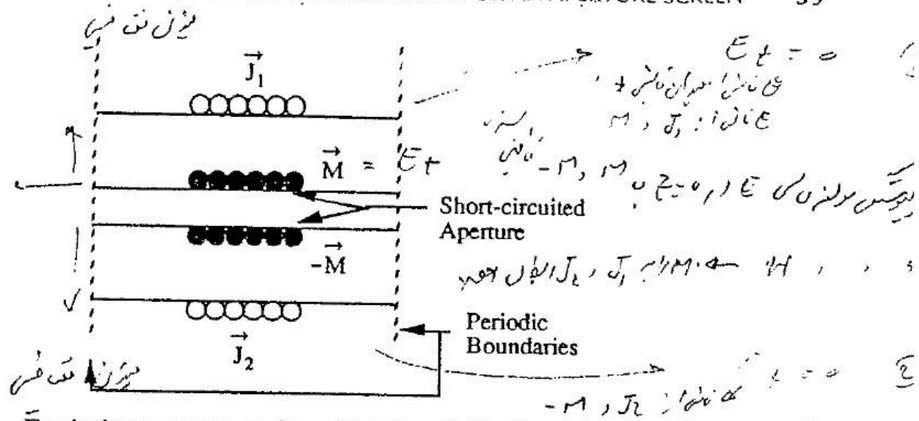

FIGURE 2.13 Equivalent structure for obtaining fields for a patch-aperture-patch FSS.

The aperture at the $z = 0$ plane is replaced by a perfectly conducting plane (shorted aperture), with the original tangential electric field at the aperture restored at $z = 0^+$ and $z = 0^-$ by appropriate magnetic surface currents $\mathbf{M}$ and $-\mathbf{M}$, respectively. The patches at $z = t_1$ and $-t_2$ are replaced by electric surface currents $\mathbf{J}_1$ and $\mathbf{J}_2$ (see Figure 2.13). One can write expressions for the magnetic field above and below the $z = 0$ plane. The total transverse magnetic field at the $z = 0^+$ plane is the sum of the field radiated by $\mathbf{M}$ in the presence of the shorted aperture and the short-circuited field due to $\mathbf{J}_1$ and the incident field. On the other hand, the field at $z = 0^-$ is radiated by $-\mathbf{M}$ in the presence of the conducting plane and the environment for the region $z < 0$ and the short-circuited field due to $\mathbf{J}_2$. The continuity of the tangential electric field at the aperture is satisfied via the choice of equivalent magnetic currents $\mathbf{M}$ and $-\mathbf{M}$. The enforcement of the continuity of the transverse magnetic field across the aperture relates the unknown magnetic surface current $\mathbf{M}$ and the electric surface currents $\mathbf{J}_1$ and $\mathbf{J}_2$.

To complete the formulation, we enforce the boundary condition that the total tangential electric field on the patches is zero. For $z > 0$, the total electric field is the sum of the incident field (with the aperture short-circuited) and the scattered field due to $\mathbf{J}_1$ and $\mathbf{M}$. For $z < 0$, the total electric field is the scattered field due to $\mathbf{J}_2$ and $-\mathbf{M}$ only.

At $z = t_1$, where the total tangential electric field on the patch is zero, we have

$$\begin{bmatrix} E_x^{\text{inc}} \\ E_y^{\text{inc}} \end{bmatrix}_{\text{S.C.}} + \sum_{m=-\infty}^{\infty} \sum_{n=-\infty}^{\infty} \left\{ \begin{bmatrix} \tilde{G}_{xx}^1 & \tilde{G}_{xy}^1 \\ \tilde{G}_{yx}^1 & \tilde{G}_{yy}^1 \end{bmatrix} \begin{bmatrix} \tilde{J}_{1x} \\ \tilde{J}_{1y} \end{bmatrix} + \begin{bmatrix} \tilde{G}_{xx}^2 & \tilde{G}_{xy}^2 \\ \tilde{G}_{yx}^2 & \tilde{G}_{yy}^2 \end{bmatrix} \begin{bmatrix} \tilde{M}_x \\ \tilde{M}_y \end{bmatrix} \right\} e^{j(\alpha_m x + \beta_n y)} = 0, \tag{2.121}$$

where the subscript S.C. corresponds to the fact that the incident field is calculated with the aperture short-circuited; that is, the aperture is removed by covering it with a conducting plane. On the other hand, the conducting patch at $z = t_1$ is removed. At $z = 0$, the continuity of the tangential magnetic field at the aperture requires

$$\begin{bmatrix} H_x^{\text{inc}} \\ H_y^{\text{inc}} \end{bmatrix}_{\text{S.C.}} + \sum_{m=-\infty}^{\infty} \sum_{n=-\infty}^{\infty} \left\{ \begin{bmatrix} \tilde{G}_{xx}^3 & \tilde{G}_{xy}^3 \\ \tilde{G}_{yx}^3 & \tilde{G}_{yy}^3 \end{bmatrix} \begin{bmatrix} \tilde{J}_{1x} \\ \tilde{J}_{1y} \end{bmatrix} + \begin{bmatrix} \tilde{G}_{xx}^4 & \tilde{G}_{xy}^4 \\ \tilde{G}_{yx}^4 & \tilde{G}_{yy}^4 \end{bmatrix} \begin{bmatrix} \tilde{M}_x \\ \tilde{M}_y \end{bmatrix} \right\} e^{j(\alpha_m x + \beta_n y)}$$

$$= \sum_{m=-\infty}^{\infty} \sum_{n=-\infty}^{\infty} \left\{ \begin{bmatrix} \tilde{G}_{xx}^5 & \tilde{G}_{xy}^5 \\ \tilde{G}_{yx}^5 & \tilde{G}_{yy}^5 \end{bmatrix} \begin{bmatrix} \tilde{M}_x \\ \tilde{M}_y \end{bmatrix} + \begin{bmatrix} \tilde{G}_{xx}^6 & \tilde{G}_{xy}^6 \\ \tilde{G}_{yx}^6 & \tilde{G}_{yy}^6 \end{bmatrix} \begin{bmatrix} \tilde{J}_{2x} \\ \tilde{J}_{2y} \end{bmatrix} \right\} e^{j(\alpha_m x + \beta_n y)}. \tag{2.122}$$

Again, zero tangential electric field on the second patch at $z = -t_2$ yields

$$\sum_{m=-\infty}^{\infty} \sum_{n=-\infty}^{\infty} \left\{ \begin{bmatrix} \tilde{G}_{xx}^7 & \tilde{G}_{xy}^7 \\ \tilde{G}_{yx}^7 & \tilde{G}_{yy}^7 \end{bmatrix} \begin{bmatrix} \tilde{J}_{2x} \\ \tilde{J}_{2y} \end{bmatrix} + \begin{bmatrix} \tilde{G}_{xx}^8 & \tilde{G}_{xy}^8 \\ \tilde{G}_{yx}^8 & \tilde{G}_{yy}^8 \end{bmatrix} \begin{bmatrix} \tilde{M}_x \\ \tilde{M}_y \end{bmatrix} \right\} e^{j(\alpha_m x + \beta_n y)} = 0. \tag{2.123}$$

The unknown electric and magnetic currents appearing in Eqs. (2.121) to (2.123) are expanded with the rooftop basis functions weighted with unknown coefficients. To solve for the unknown weighting coefficients, we need the short-circuited incident electric field at the top patch and the short-circuited incident magnetic field at the aperture. In addition, we need to derive all the spectral Green's functions appearing in Eqs. (2.121) to (2.123). We derive them by using the spectral-domain immittance approach discussed earlier.

The most important steps in this approach are to carry out a coordinate transformation that leads to the decomposition of the TE and TM fields to z components in the spectral domain. The transmission line model (TLM) is then used to derive the spectral Green's function for each of the TE and TM components. Decomposition of the TE and TM fields due to the equivalent magnetic surface current $\mathbf{M}$ can also be done in the spectral domain. Similar to Eqs. (2.1) and (2.79), we write [48]

$$\mathbf{E} = -\nabla \times \mathbf{F}, \tag{2.124}$$

$$\mathbf{H} = -j\omega\epsilon\mathbf{F} + \frac{1}{j\omega\mu}\nabla(\nabla \cdot \mathbf{F}), \tag{2.125}$$

where $\mathbf{F}$ is the electric vector potential due to $\mathbf{M}$ at the short-circuited aperture. In the spectral domain, the z components of the electric and magnetic fields are

$$\begin{cases} \tilde{E}_z = j\alpha\tilde{F}_y - j\beta\tilde{F}_x \propto \dfrac{\alpha}{\sqrt{\alpha^2+\beta^2}}\tilde{M}_y - \dfrac{\beta}{\sqrt{\alpha^2+\beta^2}}\tilde{M}_x \\ \quad = \tilde{M}_y \cos\theta - \tilde{M}_x \sin\theta = -\tilde{M}_u, \end{cases} \tag{2.126}$$

$$\begin{cases} \tilde{H}_z = \dfrac{1}{j\omega\mu}\dfrac{\partial}{\partial z}\left(\dfrac{\partial}{\partial x}\tilde{F}_x + \dfrac{\partial}{\partial y}\tilde{F}_y\right) \propto \dfrac{\alpha}{\sqrt{\alpha^2+\beta^2}}\tilde{M}_x + \dfrac{\beta}{\sqrt{\alpha^2+\beta^2}}\tilde{M}_y \\ \quad = \tilde{M}_x \cos\theta + M_y \sin\theta = \tilde{M}_v. \end{cases} \tag{2.127}$$

Note that $\tilde{E}_z$ depends only on $\tilde{M}_u$, which implies that $\tilde{M}_u$ creates only the TE fields. Similarly, $\tilde{H}_z$ depends only on $\tilde{M}_v$, and, hence, the $\tilde{M}_u$ current creates only the TM fields. Again, in (u, v) coordinates, the TE and TM fields due to $\mathbf{M}$ are decomposed in the spectral domain. With the decomposition of the TE and TM fields, the Green's function appearing in Eqs. (2.121) to (2.123) can be constructed easily with the TLM. In particular, we derive the spectral Green's functions associated with the upper-half problem as depicted in Figure 2.14. We obtain the functions associated with the lower-half problem from those for the upper half by replacing ϵ_{r1} and t_1 and ϵ_{r2} and t_2, respectively.

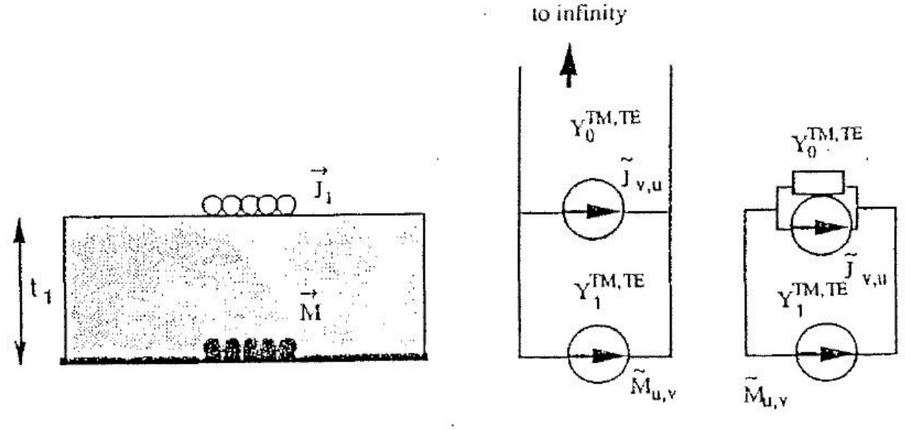

FIGURE 2.14 The upper-half problem and its equivalent transmission line models.

The upper-half problem together with its equivalent TLMs are depicted in Fig. 2.14, where Y_0 and Y_1 are the characteristic admittance of the air and dielectric regions, respectively. Note that the subscript of the electric current is suppressed for simplicity. Since the transmission line in the air region extends to infinity, we can terminate the transmission line at the dielectric/air interface with the characteristic admittance of the air region. The appropriate field quantities due to the electric and magnetic current sources can be obtained by using the superposition principle, as depicted in Figure 2.15. The relationship between the circuit and field quantities is also included in the figure.

With the characteristic admittances Y_0 and Y_1 defined in Eq. (2.91), we can now write the transmission line equations and their appropriate boundary conditions for the TLM depicted in Figures 2.15(a) and (b). In the following equations, the superscripts TE and TM and subscripts u and v are suppressed for convenience. The transmission line equations are

$$v(z) = V_0(e^{-\gamma_1 z} + \Gamma e^{\gamma_1 z}), \tag{2.128}$$

$$i(z) = Y_1 V_0(e^{-\gamma_1 z} - \Gamma e^{\gamma_1 z}). \tag{2.129}$$

For Figure 2.15(a), we have the boundary conditions

$$I + i(t_1) - v(t_1)Y_0 = 0, \tag{2.130}$$

$$v(0) = 0. \tag{2.131}$$

From Eqs. (2.128) and (2.131), we have $\Gamma = -1$. Subsequently, from Eqs. (2.128)–(2.130) we evaluate V_0 as

$$V_0 = \frac{-I}{Y_0(e^{\gamma_1 t_1} - e^{-\gamma_1 t_1}) + Y_1(e^{\gamma_1 t_1} + e^{-\gamma_1 t_1})}, \tag{2.132}$$

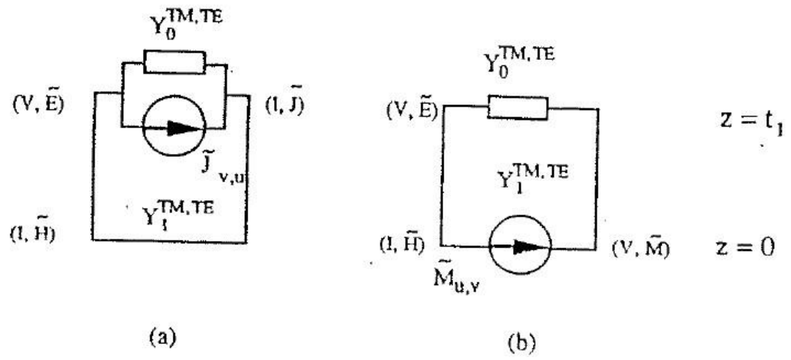

FIGURE 2.15 Equivalent transmission line models using the superposition principle (a) with electric current source, (b) with magnetic current source.

and, hence, the voltage at $z = t_1$ and the current at $z = 0$, after simplification, are

$$v(t_1) = ZI = \frac{1}{Y_0 + Y_1 \coth \gamma_1 t_1} I, \tag{2.133}$$

$$i(0) = P_1 I = \frac{-Y_1/\sinh \gamma_1 t_1}{Y_0 + Y_1 \coth \gamma_1 t_1} I. \tag{2.134}$$

On the other hand, for Figure 2.15(b), the boundary conditions are

$$v(0) = V, \tag{2.135}$$

$$i(t_1) = v(t_1)Y_0. \tag{2.136}$$

Enforcing these boundary conditions in Eqs. (2.128) and (2.129), we obtain

$$v(t_1) = P_2 V = \frac{Y_1/\sinh \gamma_1 t_1}{Y_0 + Y_1 \coth \gamma_1 t_1} V, \tag{2.137}$$

$$i(0) = YV = \frac{Y_1 + Y_0 \coth \gamma_1 t_1}{Y_0 + Y_1 \coth \gamma_1 t_1} V. \tag{2.138}$$

The functions Z, P_1, P_2, and Y are defined by Eqs. (2.133) to (2.138). From the relationships between the circuit and field quantities, the appropriate field quantities due to the electric and magnetic current sources are obtained. Recalling the fact that $\tilde{J}_u$ and $\tilde{M}_v$ generate TE fields and $\tilde{J}_v$ and $\tilde{M}_u$ generate TM fields in (u, v) coordinates, we have

$$\begin{bmatrix} \tilde{E}_u \\ \tilde{E}_v \end{bmatrix}_{\text{at } z=t_1} = \begin{bmatrix} Z^{TE} & 0 \\ 0 & Z^{TM} \end{bmatrix} \begin{bmatrix} \tilde{J}_u \\ \tilde{J}_v \end{bmatrix}, \tag{2.139}$$

$$\begin{bmatrix} \tilde{H}_u \\ \tilde{H}_v \end{bmatrix}_{\text{at } z=0} = \begin{bmatrix} 0 & P_1^{TM} \\ -P_1^{TE} & 0 \end{bmatrix} \begin{bmatrix} \tilde{J}_u \\ \tilde{J}_v \end{bmatrix}, \tag{2.140}$$

and

$$\begin{bmatrix} \tilde{E}_u \\ \tilde{E}_v \end{bmatrix}_{\text{at } z=t_1} = \begin{bmatrix} 0 & P_2^{TE} \\ -P_2^{TM} & 0 \end{bmatrix} \begin{bmatrix} \tilde{M}_u \\ \tilde{M}_v \end{bmatrix}, \tag{2.141}$$

$$\begin{bmatrix} \tilde{H}_u \\ \tilde{H}_v \end{bmatrix}_{\text{at } z=0} = \begin{bmatrix} Y^{TM} & 0 \\ 0 & Y^{TE} \end{bmatrix} \begin{bmatrix} \tilde{M}_u \\ \tilde{M}_v \end{bmatrix}. \tag{2.142}$$

However, the field quantities appearing in Eqs. (2.121) to (2.123) are in (x, y) coordinates. Therefore, Eqs. (2.139) to (2.142) have to be transformed back

to (x, y) coordinates. This can be done by the use of the transformation matrix in Eq. (2.84). As an illustration, we will derive the spectral Green's function that relates the scattered electric field $\mathbf{E}^s$ at $z = t_1$ due to the electric surface current $\tilde{J}_1$. The rest of the Green's functions follow very easily. From Eq. (2.84) we have

$$\begin{bmatrix} \tilde{E}_x^s \\ \tilde{E}_y^s \end{bmatrix} = \begin{bmatrix} \sin\theta & \cos\theta \\ -\cos\theta & \sin\theta \end{bmatrix} \begin{bmatrix} \tilde{E}_u \\ \tilde{E}_v \end{bmatrix} = \begin{bmatrix} \sin\theta & \cos\theta \\ -\cos\theta & \sin\theta \end{bmatrix} \begin{bmatrix} Z^{\mathrm{TE}} & 0 \\ 0 & Z^{\mathrm{TM}} \end{bmatrix} \begin{bmatrix} \tilde{J}_{1u} \\ \tilde{J}_{1v} \end{bmatrix}$$

$$= \begin{bmatrix} \sin\theta & \cos\theta \\ -\cos\theta & \sin\theta \end{bmatrix} \begin{bmatrix} Z^{\mathrm{TE}} & 0 \\ 0 & Z^{\mathrm{TM}} \end{bmatrix} \begin{bmatrix} \sin\theta & -\cos\theta \\ \cos\theta & \sin\theta \end{bmatrix} \begin{bmatrix} \tilde{J}_{1x} \\ \tilde{J}_{1y} \end{bmatrix}$$

$$= \begin{bmatrix} Z^{\mathrm{TE}}\sin^2\theta + Z^{\mathrm{TM}}\cos^2\theta & (Z^{\mathrm{TM}} - Z^{\mathrm{TE}})\cos\theta\sin\theta \\ (Z^{\mathrm{TM}} - Z^{\mathrm{TE}})\cos\theta\sin\theta & Z^{\mathrm{TM}}\sin^2\theta + Z^{\mathrm{TE}}\cos^2\theta \end{bmatrix} \begin{bmatrix} \tilde{J}_{1x} \\ \tilde{J}_{1y} \end{bmatrix}$$

$$= \begin{bmatrix} \tilde{G}_{xx}^1 & \tilde{G}_{xy}^1 \\ \tilde{G}_{yx}^1 & \tilde{G}_{yy}^1 \end{bmatrix} \begin{bmatrix} \tilde{J}_{1x} \\ \tilde{J}_{1y} \end{bmatrix}. \tag{2.143}$$

Following the same coordinate transformations, the rest of the spectral Green's functions are

$$\begin{bmatrix} \tilde{G}_{xx}^2 & \tilde{G}_{xy}^2 \\ \tilde{G}_{yx}^2 & \tilde{G}_{yy}^2 \end{bmatrix} = \begin{bmatrix} (P_2^{\mathrm{TE}} - P_2^{\mathrm{TM}})\sin\theta\cos\theta & P_2^{\mathrm{TE}}\sin^2\theta + P_2^{\mathrm{TM}}\cos^2\theta \\ -(P_2^{\mathrm{TE}}\cos^2\theta + P_2^{\mathrm{TM}}\sin^2\theta) & (P_2^{\mathrm{TM}} - P_2^{\mathrm{TE}})\sin\theta\cos\theta \end{bmatrix}, \tag{2.144}$$

$$\begin{bmatrix} \tilde{G}_{xx}^3 & \tilde{G}_{xy}^3 \\ \tilde{G}_{yx}^3 & \tilde{G}_{yy}^3 \end{bmatrix} = \begin{bmatrix} (P_1^{\mathrm{TM}} - P_1^{\mathrm{TE}})\sin\theta\cos\theta & P_1^{\mathrm{TM}}\sin^2\theta + P_1^{\mathrm{TE}}\cos^2\theta \\ -(P_1^{\mathrm{TM}}\cos^2\theta + P_1^{\mathrm{TE}}\sin^2\theta) & (P_1^{\mathrm{TE}} - P_1^{\mathrm{TM}})\sin\theta\cos\theta \end{bmatrix}, \tag{2.145}$$

$$\begin{bmatrix} \tilde{G}_{xx}^4 & \tilde{G}_{xy}^4 \\ \tilde{G}_{yx}^4 & \tilde{G}_{yy}^4 \end{bmatrix} = \begin{bmatrix} Y^{\mathrm{TM}}\sin^2\theta + Y^{\mathrm{TE}}\cos^2\theta & (Y^{\mathrm{TE}} - Y^{\mathrm{TM}})\cos\theta\sin\theta \\ (Y^{\mathrm{TE}} - Y^{\mathrm{TM}})\cos\theta\sin\theta & Y^{\mathrm{TE}}\sin^2\theta + Y^{\mathrm{TM}}\cos^2\theta \end{bmatrix}. \tag{2.146}$$

Note that the subscript 1 in $\tilde{J}_x$ and $\tilde{J}_y$ has been omitted for convenience. The spectral Green's functions for the lower-half problem can be obtained by replacing ϵ_{r1} and t_1 by ϵ_{r2} and t_2, respectively, in Eqs. (2.143) to (2.146). In addition, for the spectral Green's functions that are associated with the magnetic surface current, a negative sign is required since we have $-\tilde{M}$ in the lower-half problem. Hence,

$$\begin{aligned} \left[\tilde{G}^5\right] &= -\left[\tilde{G}^4\right], \\ \left[\tilde{G}^6\right] &= \left[\tilde{G}^3\right], \\ \left[\tilde{G}^7\right] &= \left[\tilde{G}^1\right], \qquad \left[\tilde{G}^8\right] = -\left[\tilde{G}^2\right], \\ \epsilon_{r1} &\to \epsilon_{r2}, \\ t_1 &\to t_2. \end{aligned} \tag{2.147}$$

Although we have derived all the necessary spectral Green's functions to solve for the unknown electric and magnetic surface currents in Eqs. (2.121) to (2.123), we need to calculate the short-circuited incident electric field on the upper patch and the incident magnetic field at the short-circuited aperture. These incident fields are derived as follows.

The short-circuited incident fields for both TE and TM polarization can be derived by using the z-directed potential Ψ. Consider the grounded dielectric slab depicted in Figure 2.16, where the incident potential Ψ^{inc} is defined as

$$\Psi^{\mathrm{inc}} = e^{j\alpha_0 x} e^{j\beta_0 y} e^{\gamma_0 z}.$$

The total potential in each of the regions is defined as

TE

$$\Psi^{\mathrm{I}} = e^{j\alpha_0 x} e^{j\beta_0 y} e^{\gamma_0 z} + Re^{j\alpha_0 x} e^{j\beta_0 y} e^{-\gamma_0 z}, \tag{2.148}$$

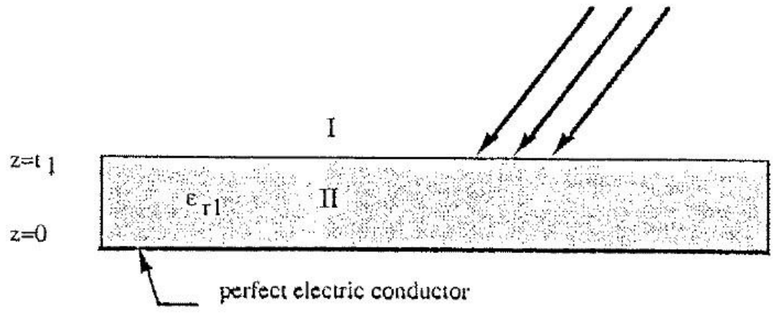

FIGURE 2.16 Short-circuited incident fields on a grounded slab.

$$\Psi^{II} = Ae^{j\alpha_0 x}e^{j\beta_0 y}\cosh\gamma_1 z, \tag{2.149}$$

TM

$$\Psi^{I} = e^{j\alpha_0 x}e^{j\beta_0 y}e^{\gamma_0 z} + Re^{j\alpha_0 x}e^{j\beta_0 y}e^{-\gamma_0 z}, \tag{2.150}$$

$$\Psi^{II} = Ae^{j\alpha_0 x}e^{j\beta_0 y}\sinh\gamma_1 z. \tag{2.151}$$

The potentials are chosen such that they satisfy the boundary condition on the perfect electric conductor. To calculate the electric and magnetic fields for the TE case from Eqs. (2.1) and (2.20), we set $\mathbf{A} = \hat{z}\Psi^{TE}$. On the other hand, for the TM case, we set $\mathbf{F} = \hat{z}\Psi^{TM}$ in Eqs. (2.124) and (2.125). By enforcing the continuity of the tangential electric and magnetic fields at $z = t_1$, we obtain the unknown coefficients R and A. Subsequently, we obtain the short-circuited electric field at $z = t_1$ and magnetic field at $z = 0$ as

TE

$$E_x^{inc}(z = t_1) = \frac{-j\beta_0 2e^{\gamma_0 t_1}\gamma_0}{\gamma_0 + \gamma_1\coth\gamma_1 t_1}e^{j\alpha_0 x}e^{j\beta_0 y}, \tag{2.152}$$

$$E_y^{inc}(z = t_1) = \frac{j\alpha_0 2e^{\gamma_0 t_1}\gamma_0}{\gamma_0 + \gamma_1\coth\gamma_1 t_1}e^{j\alpha_0 x}e^{j\beta_0 y}, \tag{2.153}$$

$$H_x^{inc}(z = 0) = \frac{2\alpha_0 e^{\gamma_0 t_1}\gamma_0\gamma_1/\sinh\gamma_1 t_1}{\omega\mu_0(\gamma_0 + \gamma_1\coth\gamma_1 t_1)}e^{j\alpha_0 x}e^{j\beta_0 y}, \tag{2.154}$$

$$H_y^{inc}(z = 0) = \frac{2\beta_0 e^{\gamma_0 t_1}\gamma_0\gamma_1/\sinh\gamma_1 t_1}{\omega\mu_0(\gamma_0 + \gamma_1\coth\gamma_1 t_1)}e^{j\alpha_0 x}e^{j\beta_0 y}, \tag{2.155}$$

TM

$$E_x^{inc}(z = t_1) = \frac{2\alpha_0\gamma_0\gamma_1 e^{\gamma_0 t_1}}{\omega\epsilon_r\epsilon_0(\gamma_0\coth\gamma_1 t_1 + \gamma_1/\gamma_0)}e^{j\alpha_0 x}e^{j\beta_0 y}, \tag{2.156}$$

$$E_y^{inc}(z = t_1) = \frac{2\beta_0\gamma_0\gamma_1 e^{\gamma_0 t_1}}{\omega\epsilon_r\epsilon_0(\gamma_0\coth\gamma_1 t_1 + \gamma_1/\gamma_0)}e^{j\alpha_0 x}e^{j\beta_0 y}, \tag{2.157}$$

$$H_x^{inc}(z = 0) = \frac{2j\beta_0 e^{\gamma_0 t_1}\gamma_0/\sinh\gamma_1 t_1}{\gamma_0 + \gamma_1\coth\gamma_1 t_1}e^{j\alpha_0 x}e^{j\beta_0 y}, \tag{2.158}$$

$$H_y^{inc}(z = 0) = -\frac{2j\alpha_0 e^{\gamma_0 t_1}\gamma_0/\sinh\gamma_1 t_1}{\gamma_0 + \gamma_1\coth\gamma_1 t_1}e^{j\alpha_0 x}e^{j\beta_0 y}. \tag{2.159}$$

With all the spectral Green's functions and short-circuited incident fields being defined, we can solve the set of simultaneous equations (2.121) to (2.123) for the unknown electric and magnetic currents. The reflection and transmission coefficients can be calculated from the tangential scattered electric fields at $z = t_1$ and $z = -t_2$ expressed in the spectral domain. The scattered field on the top surface is given by

$$\begin{bmatrix}\tilde{E}_x\\ \tilde{E}_y\end{bmatrix}_{\alpha_p\beta_q} = \begin{bmatrix}\tilde{G}_{xx}^1 & \tilde{G}_{xy}^1\\ \tilde{G}_{yx}^1 & \tilde{G}_{yy}^1\end{bmatrix}\begin{bmatrix}\tilde{J}_{1x}\\ \tilde{J}_{1y}\end{bmatrix}_{\alpha_p\beta_q} + \begin{bmatrix}\tilde{G}_{xx}^2 & \tilde{G}_{xy}^2\\ \tilde{G}_{yx}^2 & \tilde{G}_{yy}^2\end{bmatrix}\begin{bmatrix}\tilde{M}_x\\ \tilde{M}_y\end{bmatrix}_{\alpha_p\beta_q}. \tag{2.160}$$

The scattered and reflected fields are substituted into Eqs. (2.115) and (2.116) to obtain the reflection coefficients. The reflected field terms are included only when $p = q = 0$. From the solution of Eq. (2.101), the reflected field terms for the present case are

TE

$$\tilde{E}_x^r = -j\beta_0 R, \quad \tilde{E}_y^r = j\alpha_0 R, \qquad \text{where } R = \frac{e^{\gamma_0 t_1}(\gamma_0 - \gamma_1\coth\gamma_1 t_1)}{\gamma_0 + \gamma_1\coth\gamma_1 t_1}, \tag{2.161}$$

TM

$$\tilde{E}_x^r = -\frac{\alpha_0\gamma_0}{\omega\epsilon_0}R, \quad \tilde{E}_y^r = -\frac{\beta_0\gamma_0}{\omega\epsilon_0}R, \qquad \text{where}$$

$$R = \frac{e^{\gamma_0 t_1}(\gamma_0\coth\gamma_1 t_1 - \gamma_1/\epsilon_{r1})}{\gamma_0\coth\gamma_1 t_1 + \gamma_1/\epsilon_{r1}}. \tag{2.162}$$

By the same token, the transmission coefficients can be obtained very easily by replacing the appropriate spectral Green's functions. Furthermore, in the lower-half problem, the incident field has been shielded by the ground plane, and, as a result, the transmitted field terms in Eqs. (2.117) and (2.118) are deleted. The transmission coefficients are then

$$T_{pq}^{TE} = \frac{j\left[\beta_q\tilde{E}_x(\alpha_p, \beta_q) - \alpha_p\tilde{E}_y(\alpha_p, \beta_q)\right]}{\alpha_p^2 + \beta_q^2}, \tag{2.163}$$

$$T_{pq}^{TM} = \frac{j\left[\alpha_p\tilde{E}_x(\alpha_p, \beta_q) + \beta_q\tilde{E}_y(\alpha_p, \beta_q)\right]}{\left(\alpha_p^2 + \beta_q^2\right)\gamma_{pq}/j\omega\epsilon_0}, \tag{2.164}$$

where the scattered field on the bottom surface is

$$\begin{bmatrix} \tilde{E}_x \\ \tilde{E}_y \end{bmatrix}_{\alpha_p\beta_q} = \begin{bmatrix} \tilde{G}^T_{xx} & \tilde{G}^T_{xy} \\ \tilde{G}^T_{yx} & \tilde{G}^T_{yy} \end{bmatrix} \begin{bmatrix} \tilde{J}_{2x} \\ \tilde{J}_{2y} \end{bmatrix}_{\alpha_p\beta_q} + \begin{bmatrix} \tilde{G}^S_{xx} & \tilde{G}^S_{xy} \\ \tilde{G}^S_{yx} & \tilde{G}^S_{yy} \end{bmatrix} \begin{bmatrix} \tilde{M}_x \\ \tilde{M}_y \end{bmatrix}_{\alpha_p\beta_q} . \quad (2.165)$$

The power reflection and transmission coefficients of the propagating modes are obtained by taking the absolute value square of these reflection and transmission coefficients. The sum of these power reflection and transmission coefficients of the propagating modes is equal to unity when normalized to the incidence power for lossless dielectrics.

2.6 THICK-STRIP GRATINGS, CORRUGATED SURFACES, AND SLOTTED SCREENS

In addition to the dielectric loading effect, the frequency response of an FSS is also affected by the finite-thickness metallization of the conducting surface. Periodic structures with finite-thickness metallization include thick-strip gratings, corrugated surfaces, and slotted screens. Diffraction from a grating with a rectangular cross section or a corrugated surface has been analyzed with analytical techniques such as the Wiener-Hopf [71] and the dual-series approach derived from the equivalent Riemann-Hilbert problem [72]. Although these methods are mathematically rigorous, the solutions are unnecessarily complicated. A considerable number of modifications are required when the periodic structures are loaded with dielectric layers. Another class of periodic structures of interest is a thick screen, which is desirable in many applications, such as solar power filters [73], because it has a sharper stopband cutoff than does a thin screen. A moment method analysis of a thick screen has been reported [74]; however, no dielectric loading is included.

By extending the spectral domain developed for the patch-aperture-patch FSS, we derive a mixed spectral-domain approach for analyzing periodic structures with thick metallization and dielectric loading. This approach has been successfully applied to analyze microwave transmission lines and ridge waveguides [53, 54]. Structures that can be analyzed by this method are depicted in Figure 2.17.

To illustrate how the mixed spectral-domain method works, let us consider a thick-strip grating as depicted in Figure 2.18.

The essence of this approach is to short-circuit the apertures with perfectly conducting planes. The original tangential electric fields at the apertures are restored by unknown magnetic surface currents, which are found by enforcing the continuity of tangential magnetic field across the apertures.

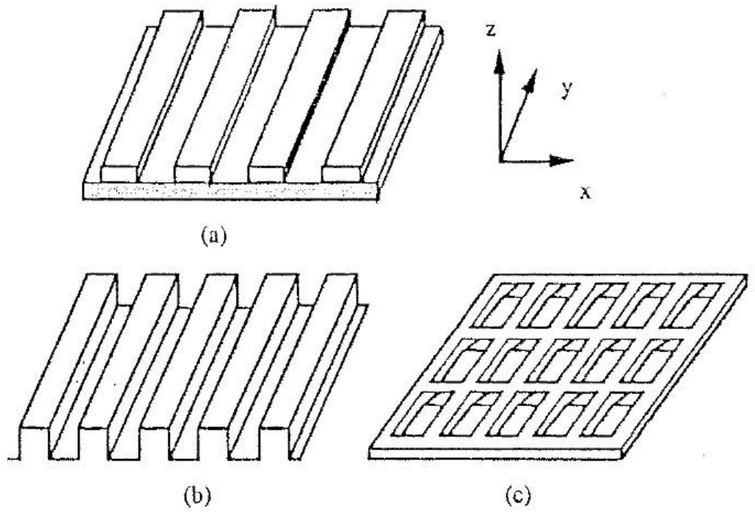

FIGURE 2.17 Periodic structures with finite-thickness metallization: (a) a thick-strip grating; (b) a corrugated surface; (c) thick slotted screen.

Mathematically, we have

$$H_x(d^+) = H_x^i(d^+) + H_x^{M_1}(d^+), \quad (2.166)$$

$$H_x(d^-) = H_x^{-M_1}(d^-) + H_x^{M_2}(d^-), \quad (2.167)$$

$$H_x(0^+) = H_x^{-M_1}(0^+) + H_x^{M_2}(0^+), \quad (2.168)$$

$$H_x(0^-) = H_x^{-M_2}(0^-), \quad (2.169)$$

$$H_x(d^+) = H_x(d^-), \quad (2.170)$$

$$H_x(0^+) = H_x(0^-). \quad (2.171)$$

The superscripts correspond to the sources that generated the magnetic fields. The incident field is calculated with the ground plane short-circuited as in the patch-aperture-patch FSS case. The key difference between the present problem and the patch-aperture-patch case is that, although the magnetic field above or below the thick aperture satisfies Floquet's condition as in the case of the patch-aperture-patch, the magnetic field inside the thick aperture satisfies the waveguide modal condition. Therefore, the spectral-domain magnetic fields above and below the apertures have a different transform variable, and the solution method involves the mixing of Floquet's

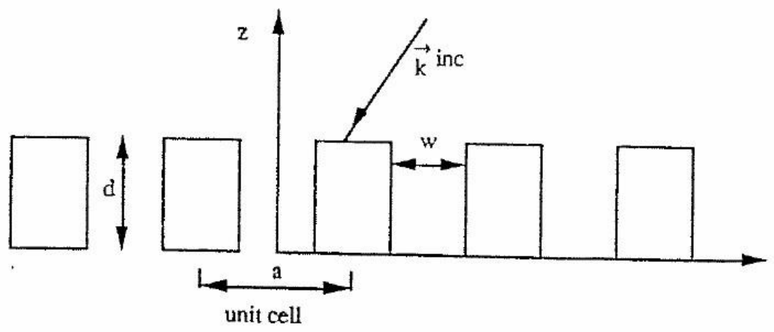

(a)

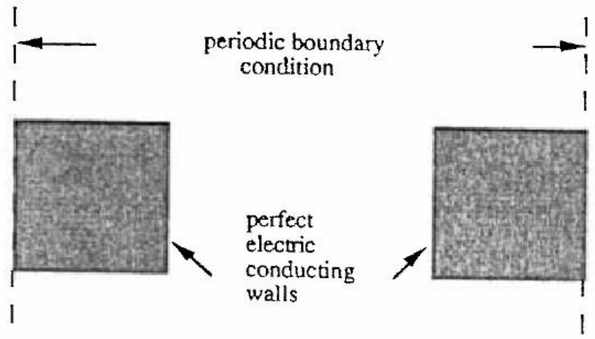

(b)

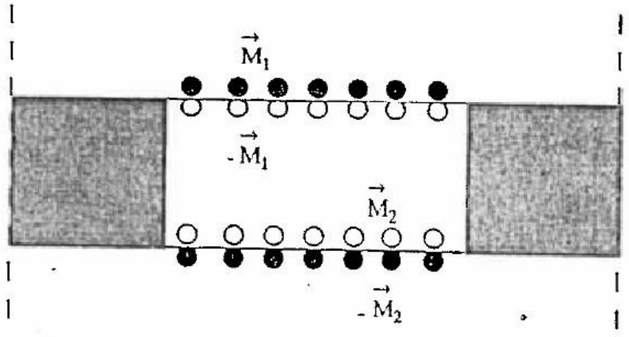

(c)

FIGURE 2.18 A thick-strip grating and its equivalent structure: (a) a thick-strip grating; (b) unit cell of the original structure; (c) unit cell of an equivalent structure.

and waveguide modes, which give the method its name of mixed spectral domain. Equations (2.170) and (2.171) can be rewritten as

$$H_x^{\text{inc}}(d^+) = -H_x^{M_1}(d^+) + H_x^{-M_1}(d^-) + H_x^{M_2}(d^-), \tag{2.172}$$

$$0 = H_x^{-M_1}(0^+) + H_x^{M_2}(0^+) - H_x^{-M_2}(0^-). \tag{2.173}$$

Expanding the scattered fields on the right-hand side as a product of the spectral Green's function and spectral magnetic currents, we have

$$H_x^{\text{inc}} = \sum_{n=-\infty}^{\infty} \tilde{G}_1 \tilde{M}_1 e^{j\alpha_n x} + \sum_{n=-\infty}^{\infty} \tilde{G}_2 \tilde{M}_1 e^{j\alpha'_n x} + \sum_{n=-\infty}^{\infty} \tilde{G}_3 \tilde{M}_2 e^{j\alpha'_n x}, \tag{2.174}$$

$$0 = \sum_{n=-\infty}^{\infty} \tilde{G}_4 \tilde{M}_1 e^{j\alpha'_n x} + \sum_{n=-\infty}^{\infty} \tilde{G}_5 \tilde{M}_2 e^{j\alpha'_n x} + \sum_{n=-\infty}^{\infty} \tilde{G}_6 \tilde{M}_2 e^{j\alpha_n x}, \tag{2.175}$$

where

$$\alpha_n = \frac{2n\pi}{a} + k_x^{\text{inc}}, \tag{2.176}$$

$$\alpha'_n = \frac{n\pi}{w}. \tag{2.177}$$

The required spectral Green's functions are derived by the spectral-domain immittance approach. The spectral Green's functions outside the slot are different from inside and are sampled according to Eqs. (2.176) and (2.177), respectively. The extension of this mixed spectral-domain approach to treat the slotted screen is straightforward. The basis functions chosen are

$$M_x = \sin\left[\frac{r\pi x}{w}\left(x + \frac{w}{2}\right)\right] e^{jk_x^{\text{inc}} x}, \tag{2.178}$$

$$M_y = \frac{T_p(2x/w)}{\sqrt{1 - (2x/w)^2}} e^{jk_x^{\text{inc}} x}, \tag{2.179}$$

where $r = 1, 2, \ldots$ and $p = 0, 1, 2, \ldots$. For the slotted screens, the basis functions in Eqs. (2.24) and (2.25) with phase factor $e^{j(k_x^{\text{inc}} x + k_y^{\text{inc}} y)}$ can be used to speed up convergence. The edge singularity varies as $\delta^{-1/3}$, and the normal component should vanish at a rate of $\delta^{1/3}$, where δ is a small distance away from the edge. One could incorporate a cubic root in the denominator of Eq. (2.179) so that these edge conditions can be satisfied exactly. The Fourier transforms of the new functions, however, require one to evaluate Bessel functions of fractional order. We will show in the numerical section that the edge conditions need not be strictly enforced. Applying

the spectral Galerkin method, we have

$$\int M_1 H^{\text{inc}}\, dx = \sum_{n=-\infty}^{\infty} \tilde{M}_1^* \tilde{G}_1 \tilde{M}_1\Big|_{\alpha_n} + \sum_{n=-\infty}^{\infty} \tilde{M}_1^* \tilde{G}_2 \tilde{M}_1\Big|_{\alpha_n'} + \sum_{n=-\infty}^{\infty} \tilde{M}_1^* \tilde{G}_3 \tilde{M}_2\Big|_{\alpha_n'}, \tag{2.180}$$

$$0 = \sum_{n=-\infty}^{\infty} \tilde{M}_2^* \tilde{G}_4 \tilde{M}_1\Big|_{\alpha_n'} + \sum_{n=-\infty}^{\infty} \tilde{M}_2^* \tilde{G}_5 \tilde{M}_2\Big|_{\alpha_n'} + \sum_{n=-\infty}^{\infty} \tilde{M}_2^* \tilde{G}_6 \tilde{M}_2\Big|_{\alpha_n}. \tag{2.181}$$

Note that matrix elements are now mixed with the two spectral domains defined in Eqs. (2.176) and (2.177). Direct matrix inversion using Gaussian elimination is employed to solve for the unknown weighting coefficients of the magnetic currents.

2.7 NUMERICAL RESULTS

The spectral Galerkin methods using the entire-domain basis functions with Gaussian elimination and the subdomain basis functions with the conjugate gradient method, respectively, have been validated against experimental measurements. For example, the former agrees well with the measurement by Ott et al. [5] for an array of narrow freestanding plates [37] between 8.5 and 12 GHz. The latter method has been validated in both the millimeter-wave [56] and infrared [75] regions. In these cases, the subdomain basis functions are required to model nonuniform resistive loading on the conducting surfaces as well as undesirable irregular unit-cell geometry caused by the fabrication process. Readers are referred to these papers for experimental verification details.

In this section we present some numerical results that illustrate the application of the techniques discussed for computing the scattering characteristics of FSSs. Let us first consider the entire-domain basis functions.

Figure 2.19 shows the convergence curves for a freestanding square-patch FSS computed using basis functions given by Eqs. (2.24) and (2.25) with and without the edge singularity term in the denominator. That is, we want to investigate the effects of the edge singularity. Contrary to the example shown in Tsao and Mittra [37], basis functions with or without edge singularity yield similar convergent solutions for this patch case. In Tsao and Mittra [37], the convergence curve is for a square aperture with $a = 1.0$ cm, $b = 0.8$ cm, and $a/\lambda_0 = 1.5$. Here our square patch is $a = 1.0$ cm, $b = 0.5$, and $a/\lambda_0 = 0.5$. Normal incidence is assumed.

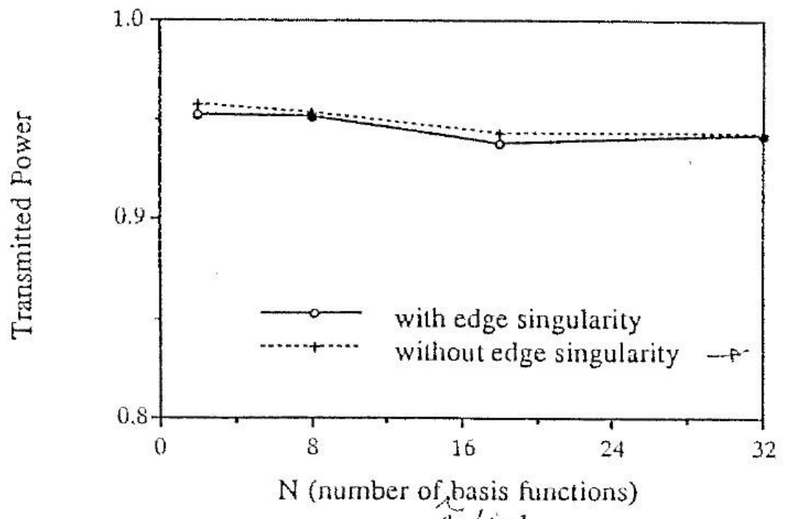

FIGURE 2.19 Convergence curves for a square-patch FSS.

Next, we compare the spectral response of the same FSS, using the entire-domain basis functions of Eqs. (2.24) and (2.25) and the rooftop subdomain basis functions. We use 8 entire-basis functions and the 112 subdomain basis functions for a 16×16 grid. Figure 2.20 shows very good agreement between the two. Here λ_0 is the free-space wavelength. The number of subdomain basis functions is small enough that we can solve the resulting matrix equation by Gaussian elimination.

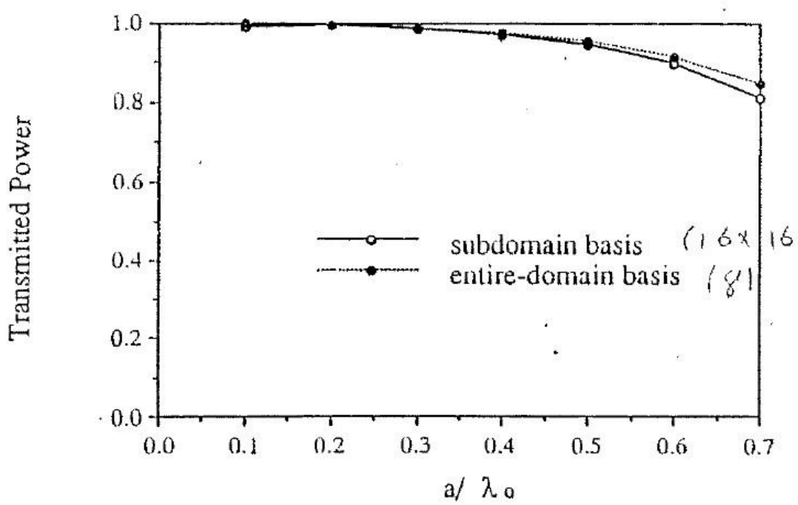

FIGURE 2.20 Comparison of transmitted power calculated by entire-domain and subdomain basis functions.

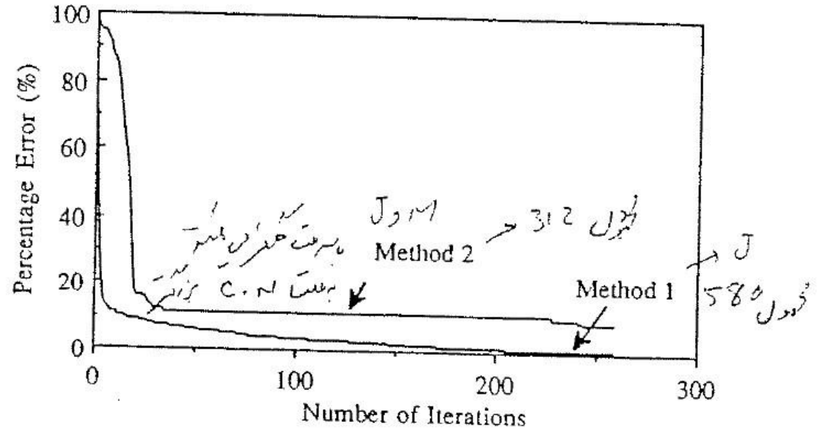

FIGURE 2.21 Comparison of rate of convergence between methods 1 and 2.

Let us consider the patch-aperture-patch structure in Figure 2.12. We have presented two approaches to analyze this structure, namely, (1) model the structure with electric currents only, as discussed in Section 2.3, or (2) model the structure with both electric and magnetic currents, as discussed in Section 2.5. Figure 2.21 shows the rate of convergence of the percentage error defined in Table 2.1 for solving the matrix equation formulated by the two methods by using the conjugate gradient iterative solution. Due to the mixing of the electric and magnetic surface currents, although proper scaling between them has been used [67], the rate of convergence of method 2 is much slower than that of method 1, which involves only electric surface currents. Note that the number of unknowns in method 2 is 312 as opposed to 580 in method 1. The slow convergence of method 2 can be attributed to the condition number of the resulting impedance matrix and the zero term in the excitation vector [70]. Although not shown here, similar convergence behavior was observed for other unit-cell geometries.

In the numerical results that follow, direct matrix inversion will be used for methods 1 and 2 when enough computer memory is available to store the impedance matrix in the core. When the matrix size becomes prohibitively large, only the conjugate gradient method is used for method 1. The conjugate gradient is not applied to method 2 because of the slow convergence behavior. Once the unknown currents are found, the reflection and transmission coefficients can be evaluated with the equations in Section 2.4.

The transmitted power of two patch-aperture-patch structures will be presented. The first one has a circular geometry (Figure 2.12), and the second one has a Jerusalem-cross unit cell. Each dielectric layer in Figure 2.12 is a 0.0254-cm Teflon-Fiberglass with a dielectric constant of 2.5. In addition, the aperture in the middle screen has the same geometry and dimensions as the top and bottom patches.

Figure 2.22 shows the numerical results for both formulations of a circular patch-aperture-patch surface with 0.7112-cm diameter in a 1.27-cm × 1.27-cm square lattice. The incident angle is $\theta^{inc} = 20°$ and $\phi^{inc} = 1°$. The circular boundary is approximated by the rooftop basis functions. Although one can use the triangular discretization for better approximation to the circular boundary using the method in Kipp and Chan [76], the nonuniform dis-

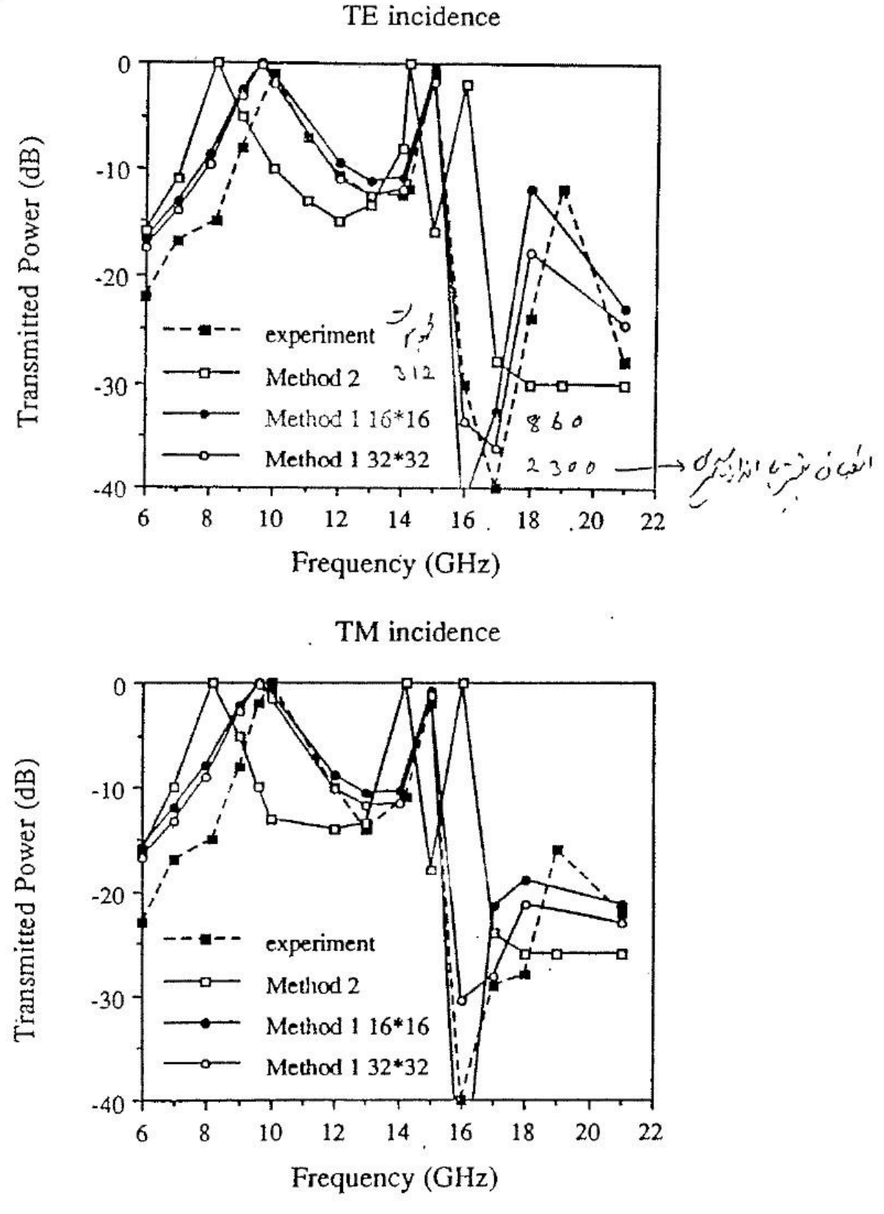

FIGURE 2.22 Comparison of spectral response between methods 1 and 2. $\theta^{inc} = 20°$.

cretization prohibits the use of FFT and therefore results in a slower solution time.

The plain solid curve is obtained by solving method 2 with matrix inversion. The number of unknowns is 312 for a 16 × 16 discretization of the unit cell. The solid curves with dots are obtained from method 1 by using both 16 × 16 and 32 × 32 discretizations having 860 and over 2300 unknowns, respectively. The results obtained from the 32 × 32 discretization of the unit cell in using method 1 best agree with experimental results, since the circular geometry is better approximated by staircasing with finer discretizations. Similar results are obtained for $\theta^{inc} = 40°$, as depicted in Figure 2.23.

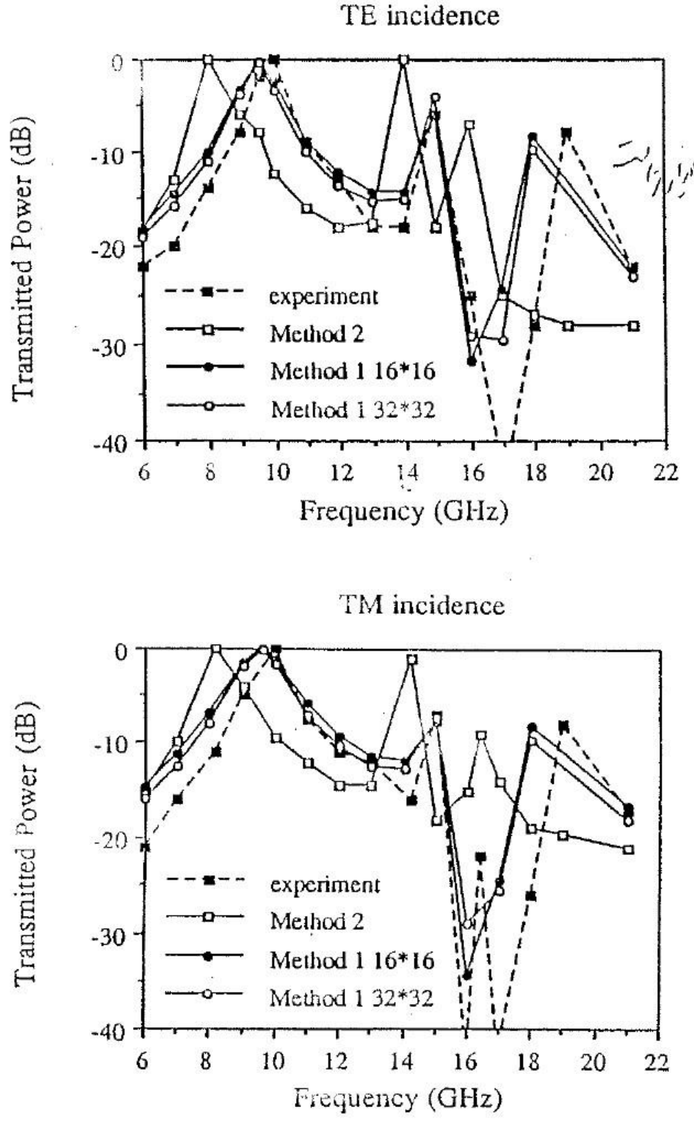

FIGURE 2.23 Comparison of spectral response between methods 1 and 2. $\theta^{inc} = 40°$.

The resonance remains stable for theta as large as 70°. Although not shown here, when ϕ^{inc} is varied, the resonance remains unchanged up to a certain value of ϕ^{inc}, say $\phi^{inc} = 45°$. Another resonance may show up between the first and second resonances, and this can be attributed to the grating-lobe phenomenon [2]. More studies are required to eliminate this unwanted resonance—for example arrange the elements in a skewed lattice. Extensive computer simulations reveal that the first resonance is due to the aperture, and the second is due to the patches. The two resonances can be shifted by adjusting the radii of the patches and the aperture. That the first resonance is controlled by the aperture explains why the second resonance calculated from method 1 tends to agree with experimental results better than the first resonance. This is because more basis functions are used in representing the electric surface currents in the perforated ground plane than are used in modeling the magnetic surface currents at the aperture. On the other hand, if the aperture is large enough that more basis functions are used to model the magnetic currents, better results from method 2 are expected.

Next, we focus our attention on the calculation of the first resonance of this tightly coupled structure. In Figure 2.24 we replace the circular geometry with a Jerusalem cross. The dimensions of the Jerusalem cross are $L = \frac{3}{4}a$, $W = \frac{1}{8}a$, $D = \frac{3}{8}a$, and $a = b = 1.27$ cm, as defined in Figure 2.5. A 16 × 16 grid is employed to discretize the unit cell. It is clearly shown that the resonance is invariant to the incident angle θ^{inc}, at least up to 70° when ϕ^{inc} is fixed at 1°.

So far we have presented numerical results for structures of zero thickness. We now consider structures with finite-thickness metallization. The analysis techniques were presented in Section 2.6. Figure 2.25 shows the comparison of the mixed spectral-domain method and the Wiener-Hopf technique [71] for a thick-strip grating with $w = d = a/3$. Excellent agreement is achieved.

Next we compare the mixed spectral-domain method with the dual-series approach [72] for the corrugated surface depicted in Figure 2.17. Figure 2.26 shows the phase difference between the fast polarization case (TM) and the slow polarization case (TE) for $\lambda_0 = 1$ cm, $a = 2.5$ cm, $a/w = 2.5$, and $0 < d < 0.3$ cm. Figure 2.26 agrees very well with Figure 6b of Lok et al. [72] and does not show the numerical difficulty such as the results presented in Figure 6a of Kok et al. [72] with the mode-matching method. Our good results may be attributed to the fact that the basis functions satisfy the edge singularity condition and that we have a phase factor in the basis function for this aperture case.

As a final example, we compare our mixed spectral-domain result with the approximate technique [74] for a thick-rectangular-aperture screen. Our method compares very well with those in Compton and Rutledge [74], which also compares well with the mode-matching method for the same structure at normal incidence. Note that the accuracy of the approximate technique deteriorates when the thickness is reduced.

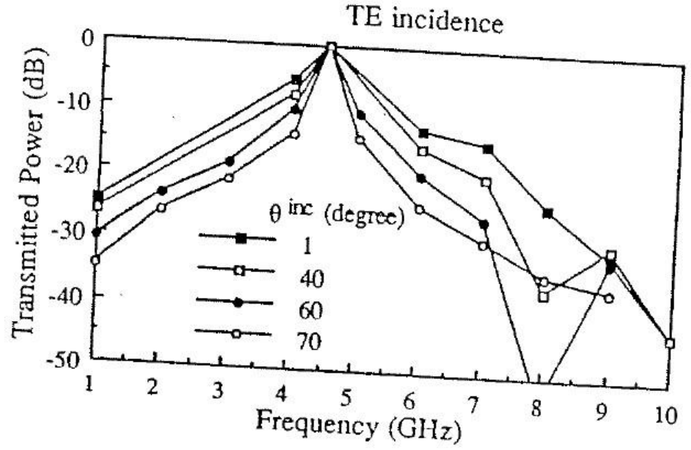

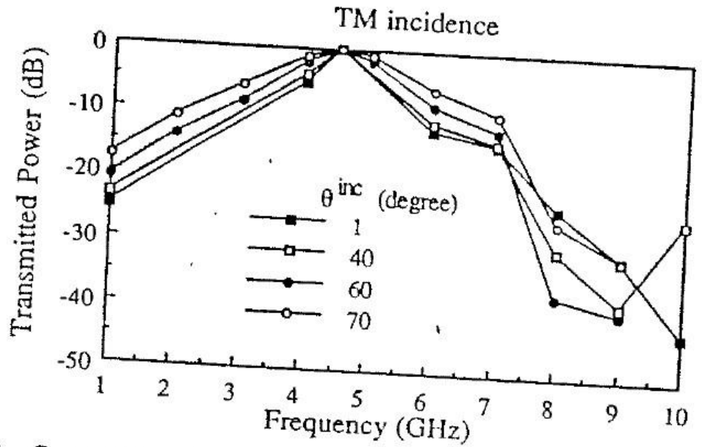

FIGURE 2.24 Comparison of spectral response at various θ^{inc}. $\phi^{inc} = 1°$. Jerusalem cross.

Note that in the analysis leading to Figure 2.27 the phase factor is included in the basis functions. To illustrate the importance of this phase factor, let us consider the same thick screen in Figure 2.27 but with the incidence field at $\theta = 20°$ and $\phi = 20°$. Figures 2.28(a) and (b) show the convergence of the spectral response with the number of basis functions with and without the phase factor, respectively. It is clear that without the phase factor, the solution does not converge rapidly, especially close to resonance.

In this chapter we presented several techniques for analysis of frequency selective surfaces. These techniques are based on Galerkin's method in the spectral domain. Both entire-domain basis functions and subdomain basis functions are considered. These functions are judiciously chosen so that they satisfy, or approximately satisfy, the edge conditions and are analytically Fourier transformable. The solution technique of the matrix equation de-

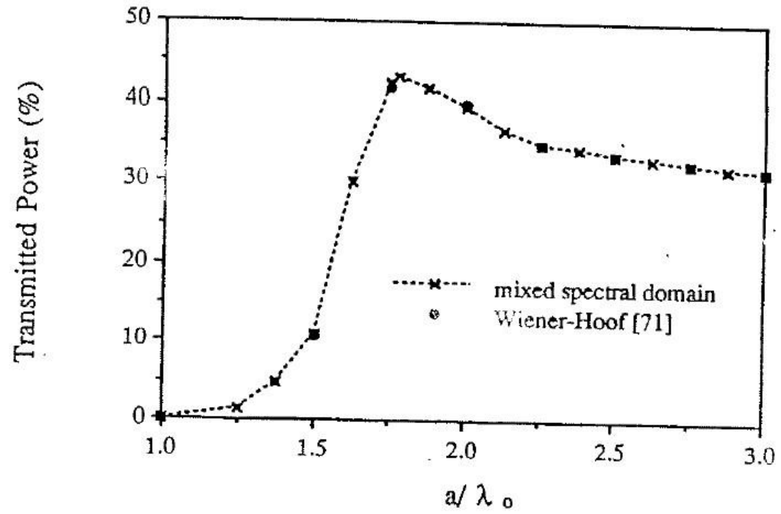

FIGURE 2.25 Comparison of the mixed spectral-domain method and Wiener-Hopf technique for a thick-strip grating.

pends on the number of unknowns. When the number of unknowns is small, which is usually the case when entire-domain basis functions are available, the matrix is solved by Gaussian elimination. In contrast, when the number of unknowns is large, due to the use of subdomain basis functions, we solve the matrix solution iteratively, using the conjugate gradient method, which is numerically efficient when coupled with the fast Fourier transform algorithm.

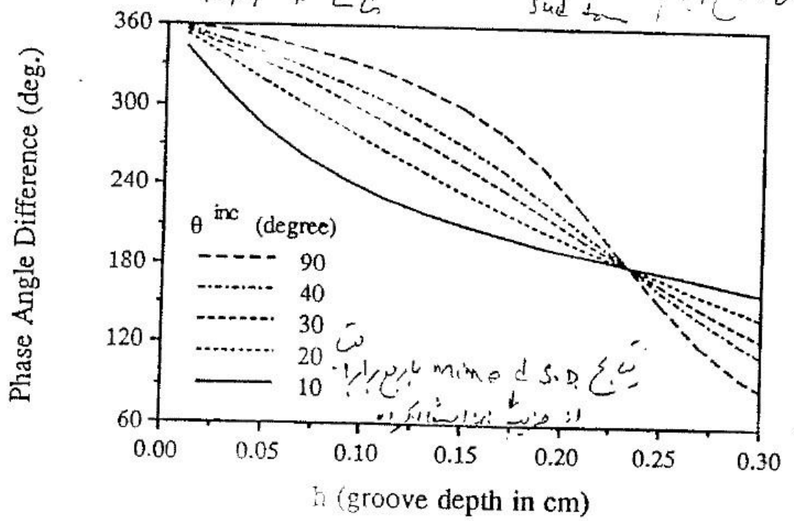

FIGURE 2.26 The phase difference between fast and slow polarization cases for a corrugated surface described in Kok et al. [72].

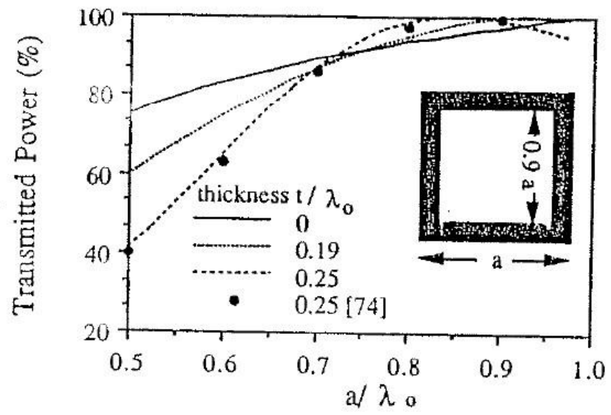

FIGURE 2.27 Comparison between the mixed-spectral-domain method and the approximate technique described in Compton and Rutledge [74].

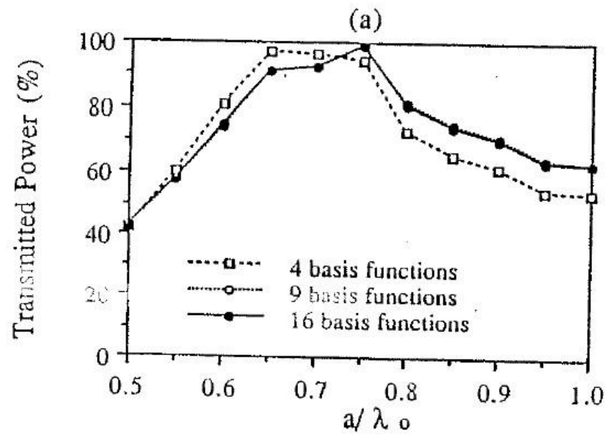

FIGURE 2.28 Convergence of spectral response with the number of basis functions (a) with phase factor, (b) without phase factor.

Depending on the problems, we formulate the integral equation by using electric surface currents, magnetic surface currents, or a combination of both. Different formulations yield different numerical efficiencies, even if the same matrix solution technique is employed. The efficiency and accuracy of all solution methods presented here have been proven based on agreement between experimental, analytical, and numerical results.

In this chapter the analysis is based on the assumptions that (i) the FSS is infinite in extent, (ii) the incident radiation is a monochromatic plane wave, and (iii) the conducting patch is infinitesimally thin. The frequency range of primary interest is that $a/\lambda_0 < 1$. For $a/\lambda_0 \gg 1$, the analysis methods are no longer practical, and other solution methods, such as the spectral iterative [77] and optical methods [4], should be adopted. When the FSS is truncated, one can no longer solve for the surface currents on a unit cell. However, one can still assume the current distributions in the cells that are not too close to the periphery of the surface to be the same as the infinite FSS. The currents on and near the peripheral cells are then modified. Detailed descriptions can be found in Ko and Mittra [78]. The effects of curvature of the surface frequency response have been discussed in Cwik and Mittra [79]. Another important point is that the material properties change with frequency and should be properly accounted for, especially at optical frequency [75]. When the incident field is not a monochromatic plane wave, one may expand the source into its plane-wave spectrum and construct the frequency response of the FSS for each of the sampled frequencies. Such treatment has been employed to calculate the interaction between a dipole antenna and an FSS [80].

REFERENCES

1. D. Rittenhouse, An optical problem, proposed by Mr. Hopkinson, and solved by Mr. Rittenhouse. *Trans. Am. Philos. Soc.* 2, 201–206 (1786).
2. R. Mittra, C. H. Chan, and T. Cwik, Techniques for analyzing frequency selective surfaces—a review. *IEEE Proc.* 76 (12), 1593–1615 (1988).
3. R. B. Kieburtz and A. Ishimaru, Scattering by a periodically apertured conducting screen. *IRE Trans. Antennas Propag.* **AP-9** (6), 506–514 (1961).
4. R. Ulrich, Far-infrared properties of metallic mesh and its complementary structure. *Infrared Phys.* 7, 37–55 (1967).
5. R. H. Ott, R. G. Kouyoumjian, and L. Peters, Jr., Scattering by a two-dimensional periodic array of narrow plates. *Radio Sci.* 2 (11), 1347–1359 (1967).
6. W. H. Miller, G. D. Bernard, and J. L. Allen, The optics of insect compound eyes. *Science* **162**, 760–767 (1968).
7. C. C. Chen, Scattering by a two-dimensional periodic array of conducting plates. *IEEE Trans. Antennas Propag.* AP-18 (5), 660–665, (1970).

8. C. C. Chen, Transmission through a conducting screen perforated periodically with apertures. *IEEE Trans. Microwave Theory Tech.* **MTT-18** (9), 627–632 (1970).

9. C. C. Chen, Diffraction of electromagnetic waves by a conducting screen perforated periodically with circular holes. *IEEE Trans. Microwave Theory Tech.* **MTT-19** (5), 475–481 (1971).

10. B. A. Munk, R. G. Kouyoumjian, and L. Peters, Jr., Reflection properties of periodic surfaces of loaded dipoles. *IEEE Trans. Antennas Propag.* **AP-19**, 612–617 (1971).

11. S. W. Lee, Scattering by dielectric-loaded screen. *IEEE Trans. Antennas Propag.* **AP-19** (5), 656–665 (1971).

12. C. C. Chen, Transmission of microwave through perforated flat plates. *IEEE Trans. Microwave Theory Tech.* **MTT-21** (1), 1–6 (1973).

13. G. H. Schennum, Frequency-selective surfaces for multiple-frequency antennas. *Microwave J.* **16**(5), 55–57 (1973).

14. L. Young, L. A. Robinson, and C. A. Hacking, Meander-line polarizer. *IEEE Trans. Antennas Propag.* **AP-21**, 376–378 (1973).

15. C. M. Horwitz, A new solar selective surface. *Opt. Commun.* **11** (2), 210–212 (1974).

16. B. A. Munk and R. J. Luebbers, Reflection properties of two-layer dipole arrays. *IEEE Trans. Antennas Propag.* **AP-22**, 766–773 (1974).

17. B. A. Munk, R. J. Luebbers, and R. D. Fulton, Transmission through a two-layer array of loaded slots. *IEEE Trans. Antennas Propag.* **AP-22**, 804–809 (1974).

18. J. A. Arnaud and F. A. Pelow, Resonant-grid quasi-optical diplexers. *Bell Syst. Tech. J.* **54** (2), 263–283 (1975).

19. J. P. Montgomery, Scattering by an infinite periodic array of thin conductors on a dielectric sheet. *IEEE Trans. Antennas Propag.* **AP-23** (1), 70–75, (1975).

20. R. J. Luebbers and B. A. Munk, Cross polarization losses in periodic arrays of loaded slots. *IEEE Trans. Antennas Propag.* **AP-23**, 159–164 (1975).

21. L. L. Tsai, T. K. Wu, and J. T. Mayhan, Scattering by multilayered lossy periodic strips with application to artificial dielectrics. *IEEE Trans. Antennas Propag.* **AP-26** (2), 257–260 (1978).

22. R. J. Luebbers and B. A. Munk, Some effects of dielectric loading on periodic slot arrays. *IEEE Trans. Antennas Propag.* **AP-26** (4), 536–542 (1978).

23. R. J. Luebbers and B. A. Munk, Mode matching analysis of biplanar slot arrays. *IEEE Trans. Antennas Propag.* **AP-27** (3), 441–443 (1979).

24. T. K. Wu, Analysis and application of multilayered periodic strips. *AEU* **33** (4), 144–148 (1979).

25. E. L. Pelton and B. A. Munk, Scattering from periodic arrays of crossed dipoles. *IEEE Trans. Antennas Propag.* **AP-27**, 323–330 (1979).

26. V. D. Agrawal and W. A. Imbriale, Design of a dichroic Casegrain subreflector. *IEEE Trans. Antennas Propag.* **AP-27** (4), 466–473 (1979).

27. M. S. Kurschlag and T. A. DeTemple, Far-IR optical properties of freestanding and dielectrically backed metal meshes. *Appl. Opt.* **20** (7), 1245–1253 (1981).

28. E. A. Parker and S. M. A. Hamdy, Rings as elements for frequency selective surfaces. *Electron. Lett.* **17** (17), 612–614 (1981).

29. C. H. Tsao, Spectral-domain approach for analyzing scattering from frequency selective surface. Ph.D. Dissertation, University of Illinois, Urbana (1981).

30. R. Cahill and E. A. Parker, Concentric ring and Jerusalem cross arrays as frequency selective surfaces for a 45° incidence diplexer. *Electron. Lett.* **18** (8), 313–314 (1982).

31. S. M. A. Hamdy and E. A. Parker, Current distribution on the elements of a square loop frequency selective surface. *Electron. Lett.* **18** (14), 624–626 (1982).

32. R. Cahill and E. A. Parker, Crosspolar levels of ring arrays in reflection at 45° incidence: Influence of lattice spacing. *Electron. Lett.* **18** (24), 1060–1061 (1982).

33. L. Henderson, The scattering of planar arrays of arbitrarily shaped slot and/or wire elements in a stratified dielectric medium. Ph.D. Dissertation, Ohio State University, Columbus (1983).

34. M. A. A. El-Morsy, E. A. Parker, and R. J. Langley, 4 layer inductive grid FSS at 45° incidence. *Electron. Lett.* **19** (16), 602–603 (1983).

35. R. J. Langley and E. A. Parker, Double-square frequency-selective surfaces and their equivalent circuit. *Electron. Lett.* **19** (17), 675–677 (1983).

36. B. J. Rubin and H. L. Bertoni, Reflection from a periodically perforated plane using a subsectional current approximation. *IEEE Trans. Antennas Propag.* **AP-31** (6), 829–836 (1983).

37. C-H. Tsao and R. Mittra, Spectral-domain analysis of frequency selective surfaces comprised of periodic arrays of cross dipoles and Jerusalem crosses. *IEEE Trans. Antennas Propag.*, **AP-32** (5), 478–486 (1984).

38. R. Mittra, R. C. Hall, and C.-H. Tsao, Spectral-domain analysis of circular patch frequency selective surfaces. *IEEE Trans. Antennas Propag.* **AP-32** (5), 533–536 (1984).

39. N. Shuley, Analysis of dichroic surfaces. Ph.D. Dissertation, Chalmers University of Technology, Gothenburgh, Sweden, (1985).

40. R. C. Hall and R. Mittra, Scattering from a periodic array of resistive strips. *IEEE Trans. Antennas Propag.* **AP-33** (9), 1009–1011 (1985).

41. J. P. Montgomery and K. R. Davey, The solution of planar periodic structures using iterative methods. *Electromagnetics* **5** (2–3), 209–235 (1985).

42. C. G. Christodoulou and J. F. Kauffman, On the electromagnetic scattering from infinite rectangular grids with finite conductivity. *IEEE Trans. Antennas Propag.* **AP-34**, 144–154 (1986).

43. R. Hall, Electromagnetic scattering from periodic structures comprised of resistive sheet material. Ph.D. Dissertation, University of Illinois, Urbana (1986).

44. T. Cwik, Scattering from general periodic screens. Ph.D. Dissertation, University of Illinois, Urbana (1986).

45. C. H. Chan, Investigation of iterative and spectral Galerkin techniques for solving electromagnetic boundary value problems. Ph.D. Dissertation, University of Illinois, Urbana (1987).

46. T. A. Cwik and R. Mittra, Scattering from a periodic array of free-standing arbitrarily shaped perfectly conducting or resistive patches. *IEEE Trans. Antennas Propag.* **AP-35** (11), 1226–1234 (1987).

47. T. Cwik and R. Mittra. The cascade connection of planar periodic surfaces and lossy dielectric layers to form an arbitrary periodic screen. *IEEE Trans. Antennas Propag.* **AP-35**, 1397–1405 (1987).

48. R. F. Harrington, *Time-Harmonic Electromagnetic Fields*. McGraw-Hill, New York, 1961.

49. R. F. Harrington, *Field Computation by Moment Methods*. Macmillan, New York, 1968.

50. A. Ishimaru, *Electromagnetic Wave Propagation, Radiation, and Scattering*. Prentice-Hall, Englewood Cliffs, NJ, 1991.

51. R. E. Jorgenson, Electromagnetic scattering from a structured slab comprised of periodically placed resistive cards. Ph.D. Dissertation, University of Illinois, Urbana, (1989).

52. R. Mittra and S. W. Lee, *Analytical Techniques in the Theory of Guided Waves*. Macmillan, New York, 1971.

53. C. H. Chan, K. T. Ng, and A. B. Kouki, A mixed spectral-domain approach for dispersion analysis of suspended planar transmission lines with pedestals. *IEEE Trans. Microwave Theory Tech.* **MTT-37** (11), 1716–1723, (1989).

54. K. T. Ng and C. H. Chan, Unified solution of various dielectric-loaded ridge waveguides with a mixed spectral-domain method. *IEEE Trans. Microwave Theory Tech.* **MTT-37**, (12) 2080–2085 (1989).

55. T. R. Schimert, A. J. Brouns, C. H. Chan, and R. Mittra, Investigation of millimeter-wave scattering from frequency selective surface. *IEEE Trans. Microwave Theory Tech.* **MTT-39** (2), 315–322 (1991).

56. C. H. Chan and R. Mittra, On the analysis of frequency selective surfaces using subdomain basis functions. *IEEE Trans. Antennas Propag.* **AP-38** (1), 40–50 (1990).

57. R. Mittra, Relative convergence of the solution of a doubly infinite set of equations. *J. Res. Nat. Bur. Stand., Sect. D* **67** (2), 245–253 (1963).

58. S. W. Lee, W. R. Jones, and J. J. Campbell, Convergence of numerical solutions of iris-type discontinuity problems. *IEEE Trans. Microwave Theory Tech.* **MTT-19** (6), 528–536 (1971).

59. R. Mittra, T. Itoh, and T. S. Li, Analytical and numerical studies of the relative convergence phenomenon arising in the solution of an integral equation by moment method. *IEEE Trans. Microwave Theory Tech.* **MTT-20** (2), 96–104 (1972).

60. N. Shuley, A note on relative convergence for moment-method solutions of integral equations of the first kind as applied to dichroic problems. *Electron. Lett.* **21** (3), 95–97 (1985).

61. K. J. Webb, P. W. Grounds, and R. Mittra, Convergence in the spectral domain formulation of waveguide and scattering problems. *IEEE Trans. Antennas Propag.* **AP-38** (6), 869–877 (1990).

62. K. M. Mitzner, Effective boundary conditions for reflection and transmission by an absorbing shell of arbitrary shape. *IEEE Trans. Antennas Propag.* **AP-16** (8), 706–712 (1968).

63. A. W. Glisson and D. R. Wilton, Simple and efficient numerical methods for problems of electromagnetic radiation and scattering from surfaces. *IEEE Trans. Antennas Propag.* AP-28 (5), 593–603 (1980).

64. L. W. Pearson, A technique for organizing large moment calculations for use with iterative solution methods. *IEEE Trans. Antennas Propag.* **AP-33**, 1031–1033 (1985).

65. M. R. Hestenes and E. Stiefel, Methods of conjugate gradient for solving linear systems. *J. Res. Nat. Bur. Stand.* **49** (6), 409–436 (1952).

66. P. M. van den Berg, Iterative computational techniques in scattering based upon the integrated square error criterion. *IEEE Trans. Antennas Propag.* **AP-32** (10), 1063–1070 (1984).

67. A. Kas and E. L. Yip, Preconditioned conjugate gradient methods for solving electromagnetic problems. *IEEE Trans. Antennas Propag.* **AP-35**, 147–152 (1987).

68. F. B. Hildebrand, *Introduction to Numerical Analysis*, 2nd ed. Dover, New York, 1974. QA 297 H54 1987

69. T. Itoh, Spectral domain immitance approach for dispersion characteristics of generalized printed transmission lines. *IEEE Trans. Microwave Theory Tech.* **MTT-28**, 733–736 (1980).

70. C. H. Chan, I. Tardy, and J. S. Yee, Analysis of three closely coupled frequency selective surface. *Arch. Elektr. Ubert.* **46**, 321–327 (1992).

71. K. Kobayashi and K. Miura, Diffraction of a plane wave by a thick strip grating. *IEEE Trans. Antennas Propag.* **AP-37** (4), 459–470 (1980).

72. Y. L. Kok, N. C. Gallagher, and R. W. Ziolkowski, Dual series solution to the scattering of plane waves from a binary conducting grating. *IEEE Trans. Antennas Propag.* **AP-37** (7), 901–917 (1989).

73. R. C. McPhedran and D. Maystre, On the theory and solar application of inductive grids. *Appl. Phys.* **14**, 1–20 (1977).

74. R. C. Compton and D. B. Rutledge, Approximation techniques for planar periodic structures. *IEEE Trans. Microwave Theory Tech.* **MTT-33** (10), 1083–1088 (1985).

75. T. R. Schimert, M. E. Koch, and C. H. Chan, Analysis of scattering from frequency-selective surfaces in the infrared. *J. Opt. Soc. Am. A* **7** (8), 1545–1553 (1990).

76. R. A. Kipp and C. H. Chan, A numerically efficient technique for the method of moments solution to planar periodic structures in layered media. *IEEE Trans. Microwave Theory Tech.* **MTT-42** (4), 635–643 (1994).

77. C-H. Tsao and R. Mittra, A spectral-iteration approach for analyzing scattering from frequency selective surfaces. *IEEE Trans. Antennas Propag.* **AP-30**, 303–308 (1982).

78. W. L. Ko and R. Mittra, Scattering characteristics of frequency-selective surface comprising truncated doubly periodic array of metallic patches. *IEEE Trans. Antennas Propag.* **AP-36**, 496–503 (1988).

79. T. Cwik and R. Mittra, The effects of the truncation and curvature of periodic surfaces: A strip grating. *IEEE Trans. Antennas Propag.* **AP-36**, 612–622 (1988).

80. C. H. Chan and R. Mittra, Investigation of antenna interaction with an FSS radome. *Int. IEEE Antennas Propag. Symp. Dig.*, 1989, Vol. 2, pp. 1076–1079 (1989).